Mon. Not. R. Astron. Soc. **000**, 1–29 (2002) Printed 11 February 2010 (MN LATEX style file v2.2)

s-Process in Low Metallicity Stars. I. Theoretical Predictions

S. Bisterzo[1⋆] and R. Gallino[1] and O. Straniero[2] and S. Cristallo[2,3] and F. Käppeler[4]
[1] *Dipartimento di Fisica Generale, Università di Torino, Via P. Giuria 1, 10125 Torino, Italy*
[2] *INAF Osservatorio Astronomico di Collurania, via M. Maggini, 64100 Teramo, Italy*
[3] *Departamento de Fisica Teorica y del Cosmos, Universidad de Granada, Campus de Fuentenueva, 18071 Granada, Spain*
[4] *Karlsruhe Institute of Technology, Campus Nord, Forschungszentrum Karlsruhe, Institut für Kernphysik, D-76021 Karlsruhe, Germany*

Accepted 1988 December 15. Received 1988 December 14; in original form 1988 October 11

ABSTRACT

A large sample of carbon enhanced metal-poor stars enriched in *s*-process elements (CEMP-*s*) have been observed in the Galactic halo. These stars of low mass ($M \sim 0.9\ M_{\odot}$) are located on the main-sequence or the red giant phase, and do not undergo third dredge-up (TDU) episodes. The *s*-process enhancement is most plausibly due to accretion in a binary system from a more massive companion when on the asymptotic giant branch (AGB) phase (now a white dwarf). In order to interpret the spectroscopic observations, updated AGB models are needed to follow in detail the *s*-process nucleosynthesis. We present nucleosynthesis calculations based on AGB stellar models obtained with FRANEC (Frascati Raphson-Newton Evolutionary Code) for low initial stellar masses and low metallicities. For a given metallicity, a wide spread in the abundances of the *s*-process elements is obtained by varying the amount of ^{13}C and its profile in the pocket, where the ^{13}C(α, n)^{16}O reaction is the major neutron source, releasing neutrons in radiative conditions during the interpulse phase. We account also for the second neutron source ^{22}Ne(α, n)^{25}Mg, partially activated during convective thermal pulses. We discuss the surface abundance of elements from carbon to bismuth, for AGB models of initial masses $M = 1.3$ – $2\ M_{\odot}$, low metallicities ([Fe/H] from -1 down to -3.6) and for different ^{13}C-pockets efficiencies. In particular we analyse the relative behaviour of the three *s*-process peaks: light-*s* (ls at magic neutron number N = 50), heavy-*s* (hs at N = 82) and lead (N = 126). Two *s*-process indicators, [hs/ls] and [Pb/hs], are needed in order to characterise the *s*-process distribution. In the online material, we provide a set of data tables with surface predictions. Our final goal is to provide a full set of theoretical models of low mass low metallicity *s*-process enhanced stars. In a forthcoming paper, we will test our results through a comparison with observations of CEMP-*s* stars.

Key words: Stars: AGB – Stars: carbon – Stars: Population II – nucleosynthesis

1 INTRODUCTION

In the last years, high-resolution spectroscopic surveys of very metal-poor stars have acquired particular interest, especially for those stars with an appreciable carbon enhancement, i.e. [C/Fe] > 1[1], the so-called Carbon Enhanced Metal-Poor stars (CEMP, Beers & Christlieb 2005). A large number of CEMP stars has been recently discovered by several survey projects, as the HK-survey (Beers et al. 1992, 2007), the ESO Large Programme First Stars with the ESO VLT and UVES spectrograph (e.g. Cayrel et al. 2004), the Hamburg/ESO Survey (Christlieb 2003), the SEGUE survey (Sloan Extension for Galactic Exploration and Understanding), the SEGUE Stellar Parameter Pipeline (SSPP; Lee et al. 2008a,b), the Sloan Digital Sky Survey (SDSS, York et al. 2000), the Chemical Abundances of Stars in the Halo (CASH) Project (Roederer et al. 2008). These surveys provide essential means to the understanding of the early universe and the Galactic chemical evolution.

⋆ E-mail: bisterzo@ph.unito.it (AVR); sarabisterzo@gmail.com (ANO)

[1] The standard spectroscopic notation is adopted: for two generic elements A and B, [A/B] = $\log_{10}(N_A/N_B)_{\star}$ - $\log_{10}(N_A/N_B)_{\odot}$ (Helfer, Wallerstein & Greenstein 1959).

To interpret the surface abundances of these objects, theoretical stellar evolutionary models are needed. We concentrate here on CEMP stars with enhancement in elements produced via *slow*-neutron capture process (*s*-process; Burbidge et al. 1957; Clayton 1961, 1968; Käppeler et al. 1982), the so-called CEMP-*s* stars. It is commonly assumed that CEMP-*s* stars belong to binary systems where a more massive asymptotic giant branch (AGB) companion, now a white dwarf, had synthesised the *s*-elements and polluted the observed star by mass transfer. Different studies about AGB nucleosynthesis are available in the literature, either with post-process method or with full stellar evolutionary models (Straniero et al. 1995, 1997, 2003; Goriely & Mowlavi 2000; Herwig 2004; Campbell & Lattanzio 2008; Cristallo et al. 2009a,b). Our calculations are based on FRANEC (Frascati Raphson-Newton Evolutionary Code) (Chieffi & Straniero 1989), coupled with a post-process method which includes a full network up to bismuth (Gallino et al. 1998).

Late on the AGB, two alternate energy sources are activated, the H-burning shell and the He-burning shell. These two shells are separated by a thin zone in radiative equilibrium, the so-called He-intershell. The H-burning shell progressively erodes the bottom layers of the envelope and produces helium. Consequently, the He-intershell grows in mass and is progressively compressed and heated until the temperature and density become high enough to trigger a thermonuclear runaway in the He shell (*thermal pulse*, TP). The sudden energy release causes the above layers to be unstable against convection, thus mixing material over the whole He-intershell (Schwarzschild & Härm 1965, 1967). The consequent expansion of the region above the He-burning shell temporarily extinguishes the H-shell. In these conditions, the convective envelope can penetrate under the H-shell, bringing to the surface newly synthesised material (*third dredge-up*, TDU). During TDU, a chemical discontinuity is established at the interface between the H-rich envelope and the He-intershell, with a sudden change of the opacity, and then, of the temperature gradient. Thus, at the radiative border, the convective velocity becomes abruptly zero, whereas it should exist a transition region, where the convective velocity smoothly decreases to 0. Therefore, a partial mixing may take place. Under this hypothesis, a small amount of hydrogen from the envelope penetrates into the top layers of the He-intershell (Iben & Renzini 1983). Then, at H-shell reignition, a thin ^{13}C-pocket forms in the top layers of the He-intershell, by proton capture on the abundant ^{12}C. There is an upper limit in the ^{13}C production in the pocket. Indeed, a higher proton abundance ingestion would produce ^{14}N by proton capture on ^{13}C. This ^{13}C is *primary*, because the diffused protons are captured by ^{12}C directly produced by helium burning during previous TPs, regardless of the metallicity. During the interpulse phase, when the temperature in the ^{13}C-pocket increases up to 1×10^8 K, neutrons are released in radiative conditions via the ^{13}C(α, n)^{16}O reaction, before the occurrence of the next thermal instability. This reaction constitutes the major neutron source in low mass AGB stars ($1.2 \lesssim M/M_{\odot} \lesssim 3$, hereafter LMS), (Straniero et al. 1995; Gallino et al. 1998).

During the convective episode originated by a TP, the *s*-process material synthesised in the pocket is diluted over the whole He-intershell, while the abundant ^{14}N nuclei in the H ashes are converted to ^{22}Ne via the ^{14}N(α, γ)^{18}F($\beta^+\nu$)^{18}O(α, γ)^{22}Ne chain. In LMS, the maximum temperature at the bottom of the TP slightly increases with pulse number, depending on the initial mass and metallicity, reaching $T \sim 3 \times 10^8$ K toward the end of the AGB phase. At this temperature the ^{22}Ne(α, n)^{25}Mg reaction is partially activated, producing a neutron burst of small neutron exposure[2] but with a high neutron density peak $n_n^{peak} < 10^{11}$ cm^{-3}, followed by a rapid decline (neutron freezout). The time dependence of this neutron burst is particularly important for defining the freezeout conditions for most of the branchings, that are sensitive to temperature and neutron density. In intermediate mass AGB stars ($4 \lesssim M/M_{\odot} \lesssim 8$, hereafter IMS), the maximum temperature during a TP reaches about 3.5×10^8 K, thus leading to a substantial activation of the ^{22}Ne(α, n)^{25}Mg.

The aim of this paper is to present in detail theoretical predictions of LMS AGB stars (M = 1.3, 1.4, 1.5 and 2.0 $M_{\odot}$) as a function of metallicity, starting from solar down to [Fe/H] = -3.6[3], focusing on stars with [Fe/H] $\leqslant -1$. Additional models of IMS in the range of $-1.6 \leqslant$ [Fe/H] $\leqslant 0$ are discussed to highlight the effects that the mass has on the stellar structure and evolution. Comparison with spectroscopic observations of CEMP-*s* stars will be presented in a forthcoming paper (Bisterzo et al., in preparation, hereafter Paper II). The models on which we base our calculations are described in Section 2. We study the behaviour of all the elements from carbon to bismuth, the three *s*-process peaks (light *s*-process elements *ls*, heavy *s*-process elements *hs*, and [Pb/Fe][4], and the *s*-process indicators [hs/ls] and [Pb/hs] by varying the metallicity and the ^{13}C-pocket efficiency, which is a parameterisation of the amount of ^{13}C and its profile in the pocket (Section 3). We also discuss the important effect of ^{22}Ne at low metallicities (Section 4), and the relevance of Na (and Mg) abundances as indicators of the initial AGB mass (Section 5). In Section 6 we give our conclusions.

2 DESCRIPTION OF THE MODELS

We perform the *s*-process nucleosynthesis with a post-process method (Gallino et al. 1998) based on full evolutionary models obtained with FRANEC code (Straniero et al. 1997, 2000, 2003). Our post-processing calculations follow

[2] The neutron exposure is the time integrated neutron flux $\tau = \int n_n v_{th} dt$, where n_n is the neutron density and v_{th} is the thermal velocity.

[3] The metallicity is defined as

$$[\mathrm{Fe/H}] = \log_{10}(\mathrm{Fe/H}) - \log_{10}(\mathrm{Fe/H})_{\odot}. \quad (1)$$

[4] We define *ls* and *hs* as

$$[\mathrm{ls/Fe}] = 1/2([\mathrm{Y/Fe}] + [\mathrm{Zr/Fe}]), \quad (2)$$

$$[\mathrm{hs/Fe}] = 1/3([\mathrm{La/Fe}] + [\mathrm{Nd/Fe}] + [\mathrm{Sm/Fe}]). \quad (3)$$

We exclude Sr from the ls elements and Ba from the hs elements because they are affected by spectroscopic uncertainties, as discussed by Busso et al. (1995) (see also Paper II). Moreover, non-local thermodinamical equilibrium (NLTE) corrections, can be significant for Sr and Ba in particular at low metallicities (Andrievsky et al. 2009; Mashonkina et al. 2008; Short & Hauschildt 2006).

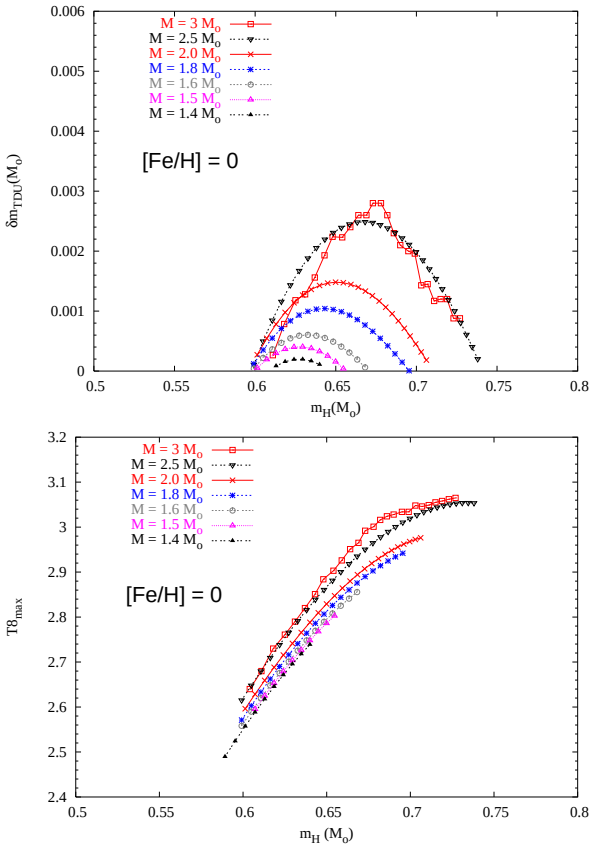

Figure 1. *Top panel:* the mass of the ^{12}C-rich and *s*-process-rich layer, $\delta m_{\rm TDU}$, that is mixed into the envelope after each TDU episode, as a function of the position in mass of the H shell, $m_{\rm H}$, for AGB models of [Fe/H] = 0 and different initial masses. Each symbol on the curves indicates the appearance of the various TDU episodes. The location of $m_{\rm H}$ grows in time due to the activation of the H-burning shell in the interpulse phase. *Bottom panel:* evolution of the maximum temperature at the base of the convective shell generated by the TPs as a function of $m_{\rm H}$ for AGB models at [Fe/H] = 0 and different masses. T_8 stand for 1×10^8 K. (*See the electronic paper for a colour version of this and the following figures.*)

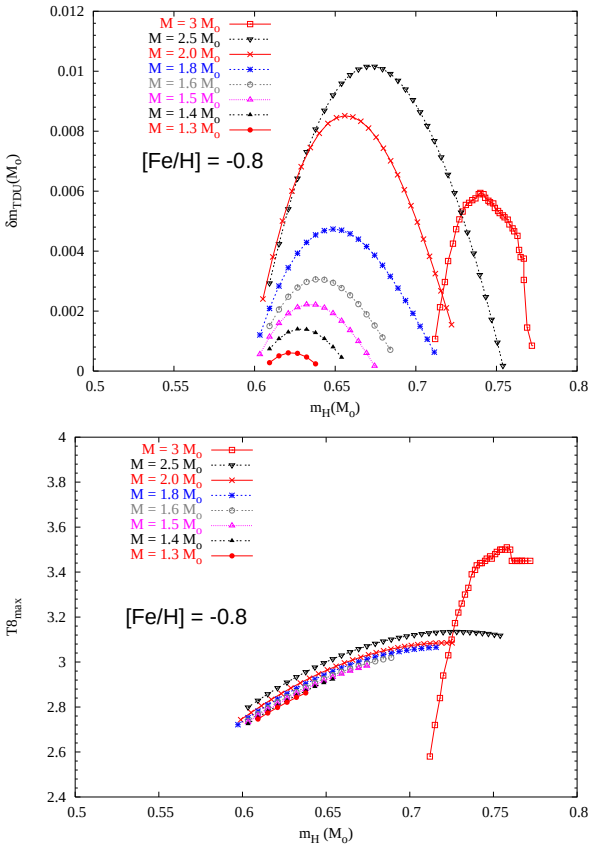

Figure 2. The same as Fig. 1, but at [Fe/H] = −0.8. Note the different scale adopted with respect to Fig. 1, top panel. By decreasing the metallicity, the mass involved in the TDU significantly increases.

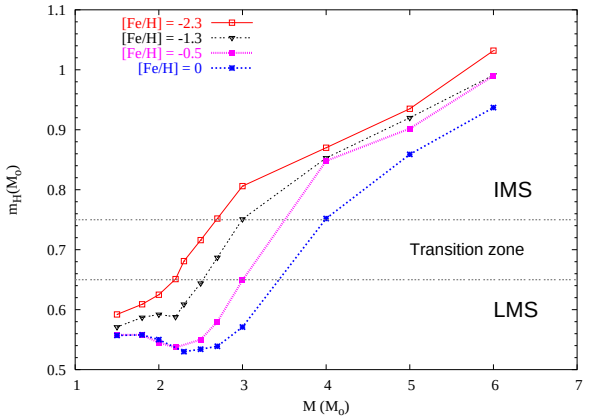

Figure 3. The mass of the core at the first TP versus the initial mass of the star, at different metallicities. The two horizontal lines correspond to a transition limit between LMS and IMS. Values are provided by Tables 1 – 4 of Domínguez et al. (1999).

the convective instabilities generated by TPs, the ^{13}C-pocket burning and the TDU episodes. The nuclear reaction rates are updated to 2009 (see KADoNiS[5] and further references given in Appendix A). The main differences with respect to previous publications is the discovery and the correction of an old bug in the models, which affected the treatment of ^{16}O produced in the pocket via ^{13}C(α, n)^{16}O. In addition, protons captures are now included to improve the prediction of the light elements. In particular ^{19}F: reaction rates of isotopes involving charged particles are taken from the NACRE compilation (Angulo et al. 1999) (web address http://pntpm3.ulb.ac.be/Nacre/barre_database.htm). We follow the prescriptions given by Straniero et al. (2003) for input data such as:

- the mass of the material dredged-up at each TDU episode,
- the temporal history of the temperature and density during the TP and their distribution in the various mass zones of the convective TP,
- the mass of the H-shell,
- the mass of the He-intershell,
- the *overlapping factor* r between successive TDUs,
- the mass of the envelope, which decreases with the TP

[5] Karlsruhe Astrophysical Database of Nucleosynthesis in Stars, web address http://nuclear-astrophysics.fzk.de/kadonis/.

number because of mass loss and by the activation of the H-burning shell, which progressively erodes the bottom of the envelope.

The interpolation formulae by Straniero et al. (2003) were available in a grid of masses up to $M = 2\ M_{\odot}$ and in the metallicity range of $-1 \lesssim$ [Fe/H] $\lesssim 0$. We have further extrapolated the stellar parameters down to [Fe/H] $= -3.6$.

For a given metallicity, a spread in the *s*-process elements is observed in MS, S, C(N) and Ba stars of the Galactic disk (see Busso et al. 1995, 2001; Abia et al. 2001, 2002; Gallino et al. 2005; Husti & Gallino 2008). At low metallicities, recent high-resolution spectroscopic measurements of CEMP-*s* stars showed an even larger spread (Ivans et al. 2005; Aoki et al. 2006; Thompson et al. 2008; Roederer et al. 2008; Bisterzo & Gallino 2008; Bisterzo et al. 2008; Sneden, Cowan & Gallino 2008). A range of *s*-process efficiencies is therefore needed in order to interpret the observations. In our calculations, we artificially introduce the ^{13}C-pocket, which is treated as a free parameter and kept constant pulse by pulse. Starting from the ST case adopted by Gallino et al. (1998) and Arlandini et al. (1999), which was shown to reproduce the solar *s*-process main component as the average of the 1.5 and 3.0 $M_{\odot}$ models at half solar metallicity (as described in Appendix A), we multiply or divide the ^{13}C (and ^{14}N) abundances in the pocket by different factors. The pocket extends in mass for $9.4 \times 10^{-4}\ M_{\odot}$ (for LMS about 1/20 of the typical mass involved in a TP), and contains $4.7 \times 10^{-6}\ M_{\odot}$ of ^{13}C and $1.6 \times 10^{-7}\ M_{\odot}$ of ^{14}N. These masses are the integrated masses in the pocket accounting for the ^{13}C and ^{14}N profiles, respectively. ^{14}N has a resonant neutron capture reaction rate ($\sigma[^{14}\mathrm{N(n,\,p)}^{14}\mathrm{C}]_{(30\mathrm{keV})} = 1.85$ mbarn, Koehler & O'Brien 1989): ^{14}N(n, p)^{14}C preventing the captured neutrons to be available for the *s*-process nucleosynthesis (while ^{14}C has a very low neutron capture cross section). We exclude the possible upper zone close to the border of the TDU where higher proton injection would produce ^{14}N > ^{13}C. The case ST×2 corresponds to an upper limit, because further proton ingestion leads to the formation of ^{14}N at expenses of ^{13}C. The *s*-process efficiency of the ^{13}C-pocket increases by decreasing the metallicity because of the lower number of iron seeds. We may define a minimum ^{13}C-pocket as the one which significantly affect the final *s* distribution, below which the *s*-process path mostly depends on the ^{22}Ne neutron exposure only. As first approximation, for solar metallicity the lowest ^{13}C-pocket is ST/6, and ST/150 for [Fe/H] $= -2.6$ (see Section 3, Fig. 5 for further details). In IMS the He-intershell mass involved is smaller than LMS by one order of magnitude and the TDU efficiency is reduced. For this reason, a different choice of ^{13}C-pocket is used for these stars: we defined the case ST-IMS, with $M(^{13}\mathrm{C}_{\mathrm{ST-IMS}}) = 10^{-7}\ M_{\odot}$.

The crude approximation in the treatment of the ^{13}C-pocket reflects a significant uncertainty which affects AGB models: in particular, the mixing processes at radiative/convective interfaces during TDU episode. In fact, the penetration of protons in the He-intershell during TDUs is currently matter of study and one of the most debated issues. Models including rotation (Langer et al. 1999), or gravity waves (Denissenkov & Tout 2003) have obtained a partial mixing zone at the base of the convective envelope during TDU episode, which leads to the formation of a ^{13}C-rich layer of limited mass extension. Similar results have been obtained by Herwig et al. (1997) and Herwig (2000), who introduced an exponential diffusive overshoot at the borders of all convective zones. A formally similar algorithm, but based on a different mixing scheme (i.e. not diffusive) has been proposed by Straniero et al. (2006), (see also Cristallo et al. 2009a). Finally, we remind that the efficiency of the TDU itself is significantly affected by the different treatment of the mixing algorithm, and it is currently a main problem with AGB computations. Different evolutionary codes do not reproduce the same results, since they are based on different treatment of the mixing algorithm (see, for instance Straniero et al. 2003; Herwig 2004; Karakas & Lattanzio 2007; Stancliffe & Jeffery 2007; Cristallo et al. 2009a, and references therein).

In AGB stars, photospheric *s*-process enrichment is observed only when the TDU takes place. According to FRANEC model, for LMS it occurs after a limited number of pulses, when the mass of the H-exhausted core reaches $\sim 0.6\ M_{\odot}$ (Straniero et al. 2003), bringing freshly synthesised material from the He-intershell into the envelope. The TDU efficiency depends on the envelope mass and on the H-burning rate (see Straniero et al. 2000). The amount of the mass dredged-up by each TDU episode, δm_{TDU}, first increases as the core mass m_{H} increases, and then decreases until vanishing when the envelope mass is reduced by mass loss to a fraction of it (about 0.5 $M_{\odot}$ at solar metallicity).

The minimum envelope mass for the occurrence of the TDU depends upon the metallicity, the core mass and the mass loss adopted. The minimum initial mass for a star that undergoes recursive TDU episodes depends on the metallicity. For a solar composition model, $M^{\mathrm{min}}_{\mathrm{TDU}} \sim 1.4\ M_{\odot}$, and it decreases with metallicity (Straniero et al. 2003). In Fig. 1, we show the mass involved in TDUs (top panel) and the maximum temperature at the base of the convective shell generated by the TPs (bottom panel) as a function of the position in mass of the H-shell, m_{H}, for AGB models of solar metallicity and different initial masses. Calculations of $M \leqslant 2.5\ M_{\odot}$ have been computed with interpolation formulae published by Straniero et al. (2003). Note that the mass involved in the TDU increases with the initial AGB mass at [Fe/H] $= 0$. At solar metallicity $M = 3\ M_{\odot}$ shows a peculiar behaviour of the TDU mass. Indeed, its maximum TDU mass is of the same order of $M = 2.5\ M_{\odot}$, and does not further increase. The same of Fig. 1 is shown in Fig. 2, but for [Fe/H] $= -0.8$, where the mass involved in the TDU increases. Significant differences are shown for $M = 3\ M_{\odot}$ at [Fe/H] $= -0.8$, with respect to LMS models: the first TP with TDU occurs when the mass of the H shell is $m_{\mathrm{H}} \sim 0.7\ M_{\odot}$ (instead of $0.6\ M_{\odot}$ as for $M \leqslant 2.5\ M_{\odot}$) and the TDU is less efficient. It was shown by Domínguez et al. (1999) (see also Boothroyd & Sackmann 1988) that for a given initial mass, the core mass increases by decreasing [Fe/H] (Fig. 3). Then, for [Fe/H] < -1.3 an initial mass $M = 3\ M_{\odot}$ approaches the behaviour of IMS stars, characterised by a thinner He-intershell and a weaker TDU. Therefore, $M = 3\ M_{\odot}$ behaves as a LMS for disk metallicities and as a IMS for halo metallicities. For $-1.3 \leqslant$ [Fe/H] $\leqslant -0.8$, we adopt the TDU mass δm_{TDU} shown in Fig. 2 for each initial mass. Then, we assume an increase

by a factor of two in the metallicity range $-2 <$ [Fe/H] < -1.3, and a further factor of two for [Fe/H] $\leqslant -2$ for AGBs with $M = 1.3$, 1.4 and 1.5 $M_{\odot}$. For $M = 2$ $M_{\odot}$, we adopt an increase of a factor of two in all the metallicity range $-3.6 \leqslant$ [Fe/H] < -1.3, following detailed results of AGB models (Cristallo et al. 2009a). Indeed, as shown in Fig. 3, $M = 2$ $M_{\odot}$ at [Fe/H] $= -2.3$ is not far from the transition zone between LMS and IMS stars. For initial masses in the range $1.3 \leqslant M \leqslant 2.0$ $M_{\odot}$ and $-3.6 \leqslant$ [Fe/H] $\leqslant -1.3$, we assumed the values of models with [Fe/H] $= -0.8$ for the other input data (like the temperature and density during the TP, the mass of the H-shell and the He-intershell, the overlapping factor and the residual mass of the envelope).
Another debated problem is the evaluation of the mass loss, which plays a key role during the AGB phase. Many stellar properties of the AGB phase depend on the mass loss: for instance, the efficiency of the TDU, the number of pulses and, therefore, the duration of this evolutionary phase. Different methods were developed to estimate the mass loss rate based on:

- observations of circumstellar envelope in giants and supergiants (Reimers 1977),
- dynamical calculations for atmospheric Mira-like stars (Bloecker 1995),
- the observed mass loss-period and the period-luminosity relations of AGB stars (Vassiliadis & Wood 1993; recently revised by Straniero et al. 2006 who account for most recent infrared data).

In the models adopted here, the mass loss is estimated with the Reimers formula:

$$\frac{dM}{dt} = -\eta \times (1.34 \cdot 10^5) \frac{L^{\frac{3}{2}}}{MT_{\rm eff}^2} (M_{\odot} \cdot yr^{-1}), \quad (4)$$

where η is the Reimers parameter; M, R and L are in solar units. We set $\eta = 0.3$ for $M = 1.3$ – 1.5 $M_{\odot}$, $\eta = 0.5$ for $M = 2.0$ $M_{\odot}$, and $\eta = 1$ for $M = 3.0$ $M_{\odot}$.
With this mass loss, at [Fe/H] $= -2.6$, $M = 1.3$ $M_{\odot}$ shows 5 TPs followed by TDU, $M = 1.5$ $M_{\odot}$ experiences 20 TPs with TDU, while $M = 2.0$ $M_{\odot}$ shows 26 TDUs. The poor knowledge of the actual mass loss rate remains one of the major uncertainties of AGB stellar models. In particular, observational constraints for the calibration of the mass loss rate at very low metallicities are lacking (see Straniero et al. 2006). Using the prescription of Reimers as compared with the one by Vassiliadis & Wood (1993), few differences in the model results are obtained during the AGB phase, with the exception of the lasts TPs where superwinds take place (Iben & Renzini 1983). On the other hand, in our models the TDU episodes cease when the envelope mass is still substantial, and all the superwind phase will take place afterward without further variations in the chemical composition.
IMS AGB models are strongly affected by the mass loss evaluation (see Straniero et al. 2000; Van Loon 2006). For IMS stars, we based our calculations on FRANEC AGB models of $M = 5.0$ $M_{\odot}$ at [Fe/H] $= 0$ and -1.3 (Straniero et al. 2000). These two models show very similar characteristics during TP phase, as the maximum temperature at the bottom of the TP (3.6 and 3.7 $\times 10^8$ K, respectively), the mass of the TDU almost constant pulse by pulse ($1.2 - 1.3 \times 10^{-3}$ $M_{\odot}$), and the mass of the He-intershell ($\sim 3 \times 10^{-3}$ $M_{\odot}$). Extrapolating, this might imply that for halo metallicities, the structure of $M = 5.0$ $M_{\odot}$ is barely distinguishable from solar. Similar characteristics are obtained for a $M = 7$ $M_{\odot}$ model (Straniero et al. 2000), with the exception of the TDU mass which is reduced by a factor of six with respect to $M = 5.0$ $M_{\odot}$ at [Fe/H] $= 0$. With our mass loss choice, the $M = 5$ $M_{\odot}$ model experience 24 TPs followed by TDU, leaving a residual total mass of 1.67 $M_{\odot}$ and a core mass of 0.9 $M_{\odot}$. Since in IMS the temperature at the bottom of the convective pulse and the peak neutron density are higher than in LMS ($T_8 \sim 3.5$; $n_n \sim 10^{11}$ cm^{-3}), the neutron source ^{22}Ne(α, n)^{25}Mg is more efficiently activated. Here, neutron-rich isotopes involved in important branchings along the *s*-process, like ^{86}Kr, ^{87}Rb and ^{96}Zr, are strongly enhanced. As already demonstrated by Travaglio et al. (2004), a remarkable *s*-process contribution to the isotopes up to zirconium is provided by IMSs during thermally pulsing phases via ^{22}Ne(α, n)^{25}Mg, the main neutron source in these stars.
Other mixing and nuclear burning phenomena not treated here are find to occur in IMS, as hot bottom burning (Sugimoto 1971; Iben 1973; Karakas & Lattanzio 2003; Ventura & D'Antona 2005), or, for [Fe/H] $\lesssim -2.3$, hot third dredge-up (Herwig 2004; Goriely & Siess 2004; Campbell & Lattanzio 2008; Lau et al. 2009). When hot bottom burning occurs (during the interpulse phase) the bottom of the convective envelope reaches the top of the H−burning and the temperature at the base is large enough ($T > 5 \times 10^7$ K) to activate the CNO, NeNa, and MgAl cycles of H burning. The hot third dredge-up, instead, is an extremely efficient dredge-up occurring at low metallicities, in which the envelope reaches almost the bottom of the intershell (or perhaps beyond it, if overshooting is included at low metallicities Herwig 2004; Lau et al. 2009). This last phenomenon modifies the efficiency of the TDU and, then, may influence the structure of the star and its evolution. Nucleosynthesis models which include hot third dredge-up are still matter of study. For this reason only IMS AGB models of disk metallicities are discussed here ($M = 5.0$ and 7.0 $M_{\odot}$; $-1.6 \leqslant$ [Fe/H] $\leqslant 0$).
At [Fe/H] $\lesssim -2.3$, also LMS may experience a single and anomalous TDU episode. It occurs when the convective zone generated by the first fully-developed TP extends till the H-rich zone, bringing protons at high temperature and causing the development of a violent thermonuclear runaway (Hollowell et al. 1990; Fujimoto et al. 2000; Iwamoto et al. 2004; Campbell & Lattanzio 2008; Lau et al. 2009; Cristallo et al. 2009b). In the present calculations we do not consider such an extreme case.

2.1 Initial chemical composition

The initial compositions (in mass fractions) used for He are: $Y = 0.28$ for $-0.3 \leqslant$ [Fe/H] $\leqslant 0.0$; $Y = 0.27$ for $-0.8 \leqslant$ [Fe/H] < -0.3; $Y = 0.26$ for $-1.3 \leqslant$ [Fe/H] < -0.8; $Y = 0.25$ for [Fe/H] < -1.3. The initial isotopic composition of the other isotopes is based on the solar meteoritic values of Anders & Grevesse (1989), except for C, N, and O isotopes, which are upgraded to Lodders (2003). For metallicity lower than solar we use solar scaled abundances, with the exception of the α elements. For oxygen, we assumed a linear increase [O/Fe] with decreasing [Fe/H] (Abia et al. 2001), ([O/Fe] $= -0.4$ [Fe/H]). For the other α elements (^{20}Ne, ^{24}Mg, ^{28}Si, ^{32}S, ^{36}Ar, ^{40}Ca, ^{48}Ti) we adopt a linear

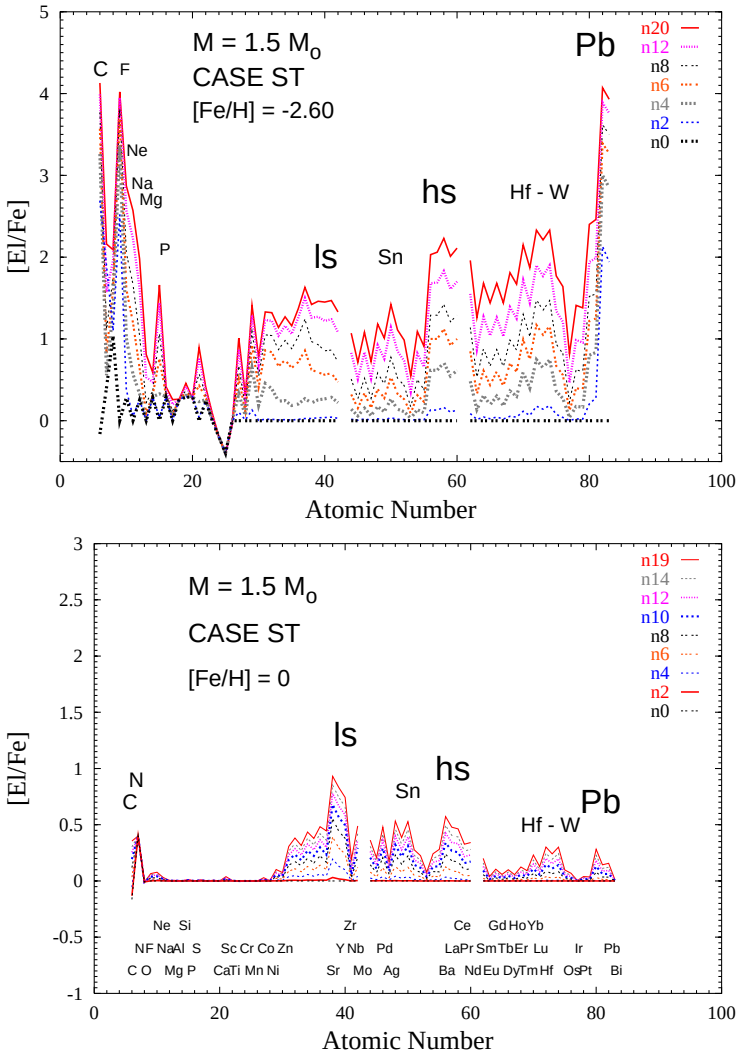

Figure 4. *Top panel*: elemental composition in the envelope after different TDU episodes (labeled as $n(i)$), for an AGB model of initial mass $M = 1.5\ M_{\odot}$, initial metallicity [Fe/H] $= -2.6$, and standard choice of the ^{13}C-pocket (case ST, Gallino et al. 1998). The labels 'n0' stands for the initial composition. Note that after 15 TPs, the abundances [El/Fe] reach an asymptotic value (the label 'El' stands for a generic element). The initial Cr and Mn abundances are chosen in agreement with the observations of unevolved halo stars (Cayrel et al. 2004; François et al. 2004). The assumed value [Mn/Fe] $= -0.4$ may increase up to [Mn/Fe] ~ -0.1 due to NLTE corrections (Bergemann & Gehren 2008). *Bottom panel*: for comparison, we report the similar case for a model with the same initial mass, but at [Fe/H] $= 0$. These models are for intrinsic AGBs ([Zr/Nb] ~ 1, see Sect. 3.2). Note the difference of scale between the two plots.

relation [α/Fe] $= -0.3$ [Fe/H] at disk metallicities ($-1 \leqslant$ [Fe/H] $\leqslant 0$), and an average constant [α/Fe] $= 0.3$ dex for [Fe/H] $\leqslant -1$, following the trend observed in unevolved stars (Cayrel et al. 2004; François et al. 2004).

We took into account the effect of the first dredge-up (Busso, Gallino & Wasserburg 1999) and second dredge-up (SDU occurring in IMS, Lattanzio et al. 1996; Busso et al. 1999) in the initial C, N, O composition of our AGB models. Concerning nitrogen, we assumed an initial value after the first dredge up [N/Fe] $= 0.3 - 0.4$, depending on the mass of the AGB, as predicted by full evolutionary models by Cristallo et al. (2009a,b). The higher surface predicted value for [N/Fe] in the AGB phase derives from dredging to the surface also the ashes of the temporary inactivated H-burning shell, where all CNO isotopes are almost converted to ^{14}N, including the primary ^{12}C that is present in the envelope due to previous TDU episodes. As a consequence, [N/Fe] increases with the number of TDU episodes.

3 RESULTS AND DISCUSSION

3.1 The three *s*-process peaks

Nuclei with a magic neutron number ($N = 50$, 82, and 126) are essentially produced by the *s*-process, since their low neutron capture cross sections act as a bottleneck for the *s*-path.

In Fig. 4, we shown the envelope abundances after each TDU for an AGB model of initial mass $M = 1.5\ M_{\odot}$, a case ST and [Fe/H] $= -2.6$ (top panel). As a comparison, we plot the envelope abundances for the same case, but at

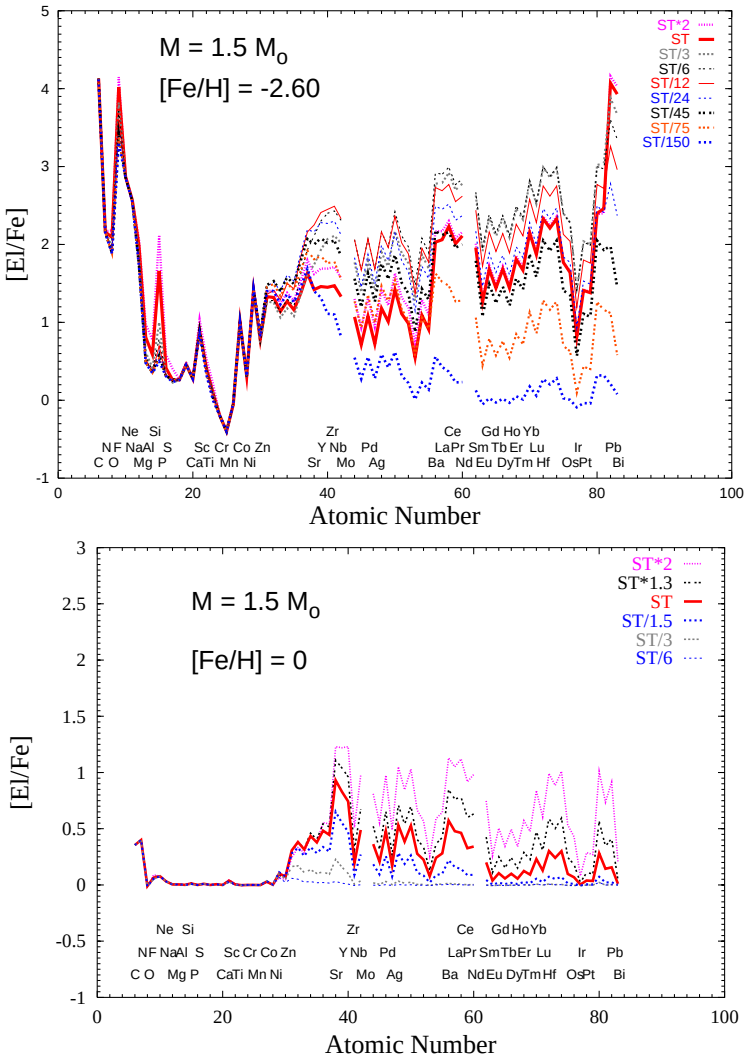

Figure 5. *Top panel*: elemental composition in the envelope at the last TDU, for AGB models of initial mass $M = 1.5\ M_{\odot}$, initial metallicity [Fe/H] $= -2.6$, and different choices of the ^{13}C-pocket efficiency. Similar results are predicted for $M = 2.0\ M_{\odot}$. In the on line material, Fig. C1, the same plot is shown for an AGB model of initial mass $M = 1.3\ M_{\odot}$. *Bottom panel*: the same as top panel, but at [Fe/H] $= 0$. These models are for intrinsic AGBs ([Zr/Nb] ~ 1, see Sect. 3.2).

[Fe/H] $= 0$ (bottom panel). We underline the completely different shapes of the two distributions. At low metallicities a distribution weighted toward heavier elements emerges: in particular, already after the first TDU, lead receives an extraordinary contribution ([Pb/Fe] ~ 4.1), producing also a huge amount of ^{209}Bi by neutron captures on ^{208}Pb ([Bi/Fe] ~ 3.9). This occurs because ^{56}Fe (the seed of the *s*-process) decreases with metallicity, thus the number of neutrons available per iron seed increases, due to the fact that the ^{13}C neutron source is primary (Clayton 1988). Hence, the neutron fluence overcomes the first two peaks, directly feeding ^{208}Pb (Gallino et al. 1998; Goriely & Mowlavi 2000; Travaglio et al. 2001). Note that the increase of heavy elements is more pronounced during the first TPs, achieving an asymptotic trend beyond the 10$^{\rm th}$ TDU.

During the TDU, also the material of the H-shell is carried to the surface: this zone is rich of primary ^{14}N produced from primary ^{12}C during the CNO cycle. The nitrogen surface prediction takes into account for this primary ^{14}N, and, therefore, [N/Fe] increases with the number of TDU episodes and by decreasing the metallicity. Carbon is efficiently enhanced in the envelope at [Fe/H] $= -2.6$ already at the first TDUs (for the case ST we predict [C/Fe] ~ 2.7, Fig. 4, top panel). The overproduction of carbon, in fact, increases by decreasing the metallicity due to the primary amount of ^{12}C and to the deeper TDUs as well (Section 2). Two further peaks are predicted: at Sn (before hs) and at Hf/W (before Pb/Bi). These elements receive an *s*-process contribution to the solar abundances of Sn$_{\rm s}$ = 66%, Hf$_{\rm s}$ = 59%, Ta$_{\rm s}$ = 45%, W$_{\rm s}$ = 64% (see Appendix A).

Fig. 5, top panel, shows AGB models of $M = 1.5\ M_{\odot}$ at [Fe/H] $= -2.6$, by varying the efficiency of the ^{13}C-pocket. Similarly, we show in Fig. 5, bottom panel, the same result at solar metallicity. The solid heavy line represents the case ST. Decreasing the ^{13}C-pocket efficiency to ST/24, lead is reduced of more than 1 dex with respect to the ST case. At [Fe/H] $= -2.6$, for ^{13}C-pockets $\leqslant$ ST/75, the ^{13}C is negligible and the *s*-process production is principally due to the

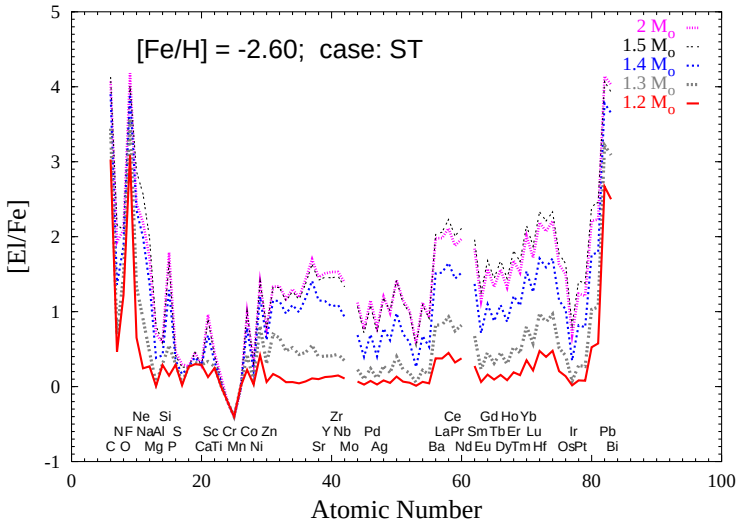

Figure 6. Elemental composition in the envelope at the last TDU, for AGB models of initial metallicity [Fe/H] = −2.6, but different initial masses: $1.2 \leqslant M/M_{\odot} \leqslant 2.0$ (cases ST).

^{22}Ne(α, n)^{25}Mg reaction activated during the TPs. Some production of the ls elements is still observed with a case ST/150.

In Table 1, we list the theoretical predictions for elements from Sr to Bi at the last TDU for an initial mass $M = 1.5$ $M_{\odot}$ at [Fe/H] = −2.6 and different ^{13}C-pocket efficiencies (ST, ST/12, ST/45, ST/75). In Col.s 3 to 6 we shown the [El/Fe] predictions, which, in Col.s 7 to 10, are normalised to europium in logarithmic scale [El/Eu] (the label 'El' stands for a generic element). The case ST predicts [hs/ls] = 0.6 (Col. 3), while [hs/ls] reaches −0.25 by decreasing the *s*-process efficiency down to ∼ ST/70 (similarly to the case ST at [Fe/H] = −0.3, see Appendix A). Since europium is an element with dominating *r*-process abundances, the lanthanum/europium ratio provides a measure of the *s*- and *r*-process components in halo stars. A pure *s*-process contribution predicts $0.8 \leqslant [\mathrm{La/Eu}]_s \leqslant 1.1$ at [Fe/H] = −2.6 (Cols. 7 to 10). Values $[\mathrm{La/Eu}]_s \lesssim 0.4$ indicate stars that have experienced an important *r*-process contribution in addition to the *s*-process enhancements (see Paper II).

Another parameter affecting the overabundances is the initial AGB mass, which determines not only the *s*-process element abundances, but also some of the light element abundances (like Na and Mg), which are not affected by the ^{13}C-pocket efficiency (see Section 5 for a detailed description). In Fig. 6, we show a comparison of the theoretical results obtained for $1.2 \leqslant M/M_{\odot} \leqslant 2.0$. The limited number of TDUs for the lowest mass models explains the smaller abundances. Changing the initial mass, we predict variations up to 2.5 dex for the light elements (as Na and Mg, as discussed in Section 5), 1.5 dex for the ls peak, about 2 dex for the hs peak and 1.5 dex for Pb. In Appendix B (Section B1), we list surface elemental predictions at [Fe/H] = −2.6 for different initial AGB masses: $M^{\mathrm{AGB}}_{\mathrm{ini}} = 1.3$, 1.4, 1.5 and 2.0 $M_{\odot}$.

In order to extend our theoretical analysis to different stellar populations, we discuss the AGB results by varying the metallicity. In Figs. 7 to 9, we present theoretical predictions of [ls/Fe], [hs/Fe] and [Pb/Fe] versus [Fe/H] for AGB models with initial masses $M = 1.3$, 1.5 and 2.0 $M_{\odot}$ and different ^{13}C-pocket efficiencies (from ST×2 down to ST/150). In Appendix B (Section B2), we give tabulated surface predictions, for AGB initial masses $M = 1.3$ and 1.5 $M_{\odot}$, $-3.6 \leqslant$ [Fe/H] $\leqslant -1.0$, and two choices of the ^{13}C-pocket, (ST and ST/12). Obviously, models with more TDU (Fig. 1 and 2) show larger surface s-process enhancements. In Table 2 we list the number of pulses with TDU experienced by each model. Results from 1.5 and 2 $M_{\odot}$ models are in general quite similar (Fig. 7, middle and bottom panels). Depending on the metal content and on the efficiency of the ^{13}C-pocket, the behaviour of the [ls/Fe] peak is highly non linear as a function of the metallicity and on the ^{13}C amount. For example in the ST case of the $M = 1.5$ $M_{\odot}$ model, the [ls/Fe] ratio increases starting from solar down to [Fe/H] ∼ −0.8, where there is a local maximum. Then, [ls/Fe] decreases down [Fe/H] ∼ −1.5, because the *s*-path overcomes the ls (and hs) elements feeding lead. Further decreasing the metallicity ([Fe/H] $\lesssim -1.5$), [ls/Fe] increases again. This is the consequence of the primary ^{22}Ne contribution, which provides an additional neutron exposure. In fact, by decreasing the metallicity, a progressively high amount of primary ^{22}Ne is produced in the advanced pulses, by the conversion of primary ^{12}C to primary ^{14}N in the H-burning ashes followed by double α capture on the ^{14}N in the early phases of the next TP (see Section 4 for further explanations). For less efficient ^{13}C-pockets, e.g. the case ST/12, the highest [ls/Fe] value is shifted toward lower metallicities ([Fe/H] ∼ −2), because of the lower number of neutrons produced. For [Fe/H] $\leqslant -2$, a flat behaviour is achieved.

The [hs/Fe] trend is similar to the behaviour previously discussed for [ls/Fe], but with slightly different slopes (Fig. 8). As for [ls/Fe], a primary ^{22}Ne contribution to [hs/Fe] is observed for [Fe/H] $\lesssim -2$. When the hs-peak reaches a local maximum, the hs nuclei are used for the production of lead. [Pb/Fe] increases by decreasing the metallicity, covering a range of 4 orders of magnitude (Fig. 9). The results for [Pb/Fe] varying the initial stellar mass is very similar, with higher overabundances according to the rising number of TPs.

Table 1. Theoretical predictions of [El/Fe] and [El/Eu] for elements from Sr to Bi (the label 'El' stands for a generic element), at [Fe/H] = −2.6, for $M = 1.5\ M_{\odot}$ models and various choices of the ^{13}C-pocket (ST, ST/12, ST/45, ST/75).

		$M = 1.5\ M_{\odot}$ [Fe/H] = −2.6							
El	Z	[El/Fe]				[El/Eu]			
		ST	ST/12	ST/45	ST/75	ST	ST/12	ST/45	ST/75
(1)	(2)	(3)	(4)	(5)	(6)	(7)	(8)	(9)	(10)
Sr	38	1.42	2.25	2.00	1.81	0.16	0.53	0.92	1.36
Y	39	1.46	2.41	2.08	1.85	0.20	0.69	1.00	1.40
Zr	40	1.45	2.45	2.02	1.76	0.19	0.73	0.94	1.31
Nb	41	1.47	2.49	2.05	1.78	0.21	0.77	0.97	1.33
Mo	42	1.33	2.33	1.85	1.55	0.07	0.61	0.77	1.10
Ru	44	1.07	2.06	1.56	1.27	-0.19	0.34	0.48	0.82
Rh	45	0.71	1.67	1.19	0.92	-0.55	-0.05	0.11	0.48
Pd	46	1.08	2.07	1.63	1.35	-0.18	0.35	0.55	0.90
Ag	47	0.72	1.68	1.26	1.00	-0.54	-0.04	0.18	0.55
Cd	48	1.18	2.16	1.76	1.47	-0.08	0.44	0.68	1.02
In	49	1.01	1.96	1.56	1.27	-0.25	0.24	0.48	0.82
Sn	50	1.42	2.36	1.87	1.54	0.16	0.64	0.79	1.09
Sb	51	1.11	2.02	1.51	1.17	-0.15	0.30	0.43	0.72
Te	52	0.99	1.88	1.37	1.03	-0.27	0.16	0.29	0.58
I	53	0.55	1.37	0.88	0.57	-0.71	-0.35	-0.20	0.13
Xe	54	1.09	1.95	1.43	1.06	-0.17	0.23	0.35	0.61
Cs	55	0.91	1.77	1.29	0.92	-0.35	0.05	0.21	0.48
Ba	56	2.03	2.73	2.17	1.63	0.77	1.01	1.09	1.18
La	57	2.06	2.69	2.12	1.52	0.80	0.97	1.04	1.07
Ce	58	2.23	2.77	2.16	1.47	0.97	1.05	1.08	1.02
Pr	59	2.01	2.55	1.96	1.27	0.75	0.83	0.88	0.82
Nd	60	2.11	2.62	2.00	1.28	0.85	0.90	0.92	0.83
Sm	62	1.96	2.44	1.79	1.06	0.70	0.72	0.71	0.61
Eu	63	1.26	1.72	1.08	0.45	0.00	0.00	0.00	0.00
Gd	64	1.68	2.16	1.49	0.79	0.42	0.44	0.41	0.34
Tb	65	1.44	1.91	1.25	0.57	0.18	0.19	0.17	0.13
Dy	66	1.68	2.14	1.46	0.76	0.42	0.42	0.38	0.31
Ho	67	1.44	1.89	1.21	0.55	0.18	0.17	0.13	0.10
Er	68	1.81	2.26	1.57	0.85	0.55	0.54	0.49	0.41
Tm	69	1.67	2.11	1.42	0.72	0.41	0.39	0.34	0.27
Yb	70	2.15	2.58	1.87	1.13	0.89	0.86	0.79	0.68
Lu	71	1.87	2.28	1.58	0.85	0.61	0.56	0.50	0.41
Hf	72	2.33	2.75	2.05	1.28	1.07	1.03	0.97	0.83
Ta	73	2.21	2.62	1.92	1.16	0.95	0.90	0.84	0.71
W	74	2.33	2.75	2.05	1.27	1.07	1.03	0.97	0.82
Re	75	1.77	2.13	1.41	0.70	0.51	0.41	0.33	0.25
Os	76	1.64	2.04	1.35	0.63	0.38	0.32	0.27	0.18
Ir	77	0.82	1.19	0.56	0.09	-0.44	-0.53	-0.52	-0.35
Pt	78	1.41	1.80	1.11	0.43	0.15	0.08	0.03	-0.02
Au	79	1.38	1.76	1.07	0.40	0.12	0.04	-0.01	-0.05
Hg	80	2.40	2.77	2.05	1.26	1.14	1.05	0.97	0.81
Tl	81	2.46	2.72	1.93	1.16	1.20	1.00	0.85	0.71
Pb	82	4.07	3.26	1.98	1.12	2.81	1.54	0.90	0.67
Bi	83	3.93	2.96	1.45	0.58	2.67	1.24	0.37	0.13
[hs/ls]		0.59	0.15	-0.08	-0.52				
[Pb/hs]		2.03	0.68	0.01	-0.17				

Table 2. We listed the number of pulses with TDU experienced by each model.

Stellar Mass ($M_{\odot}$)	[Fe/H]	Number of TDUs	[Fe/H]	Number of TDUs
1.3	0; −0.3	0	from −0.5 down to −3.6	5
1.4	0; −0.3	10	from −0.5 down to −3.6	10
1.5	0; −0.3	19	from −0.8 down to −3.6	20
2.0	0; −0.3	22; 25	from −0.5 down to −3.6	26
3.0	0; −0.3	25	−0.5; from −0.8 down to −1.6	26; 35
5.0	0; −0.3	24	from −0.5 down to −1.6	24
7.0	0; −0.3	24	from −0.5 down to −1.6	24

The differences between models presented here and previous publications (Bisterzo et al. 2009; Sneden et al. 2008) are principally due to the correction of a past bug in the code, where we did not account for the poisoning effect of ^{16}O in the pocket produced by the ^{13}C(α, n)^{16}O reaction. While no variations in the *s*-process abundances are found from solar metallicity down to [Fe/H] = −1.6, at halo metallicities, the *s*-process abundances may be strongly reduced for high ^{13}C-pocket efficiencies. For cases ST×2 down to ST variations up to 0.5 dex are obtained for $M = 1.5$ and 2 $M_{\odot}$. Even higher variations (up to 0.8 dex) are obtained for AGB models of $M = 1.3$ and 1.4 $M_{\odot}$. Changes lower than 0.1 dex are observed for cases < ST/1.5.

The addition of proton captures in the network does not involve variations in the *s*-process elements production,

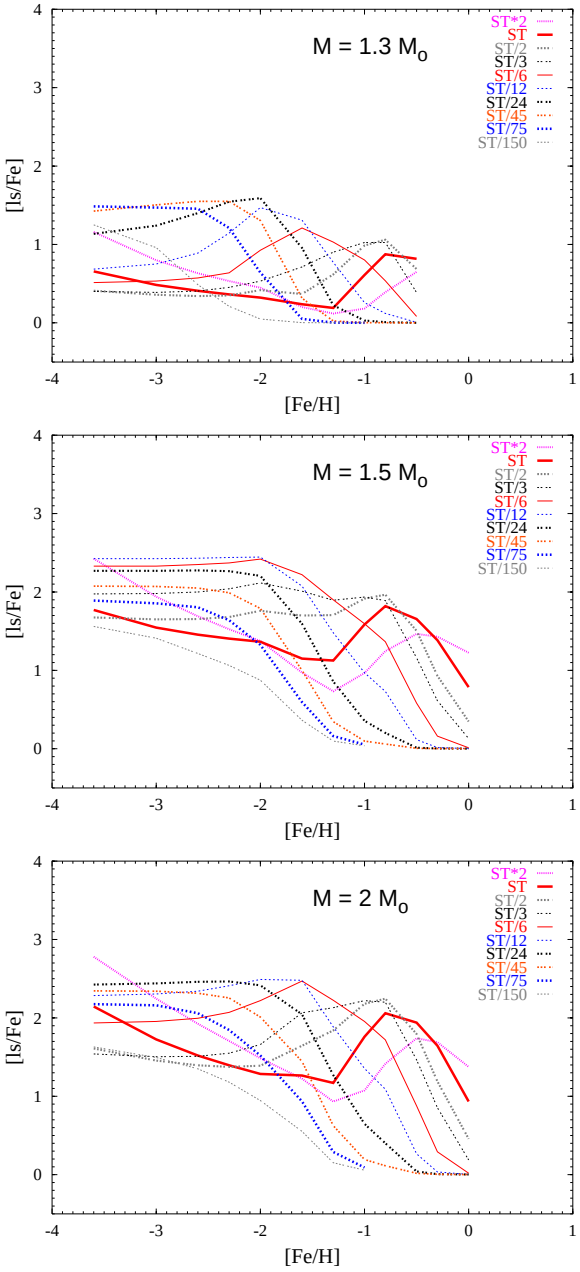

Figure 7. Theoretical results of [ls/Fe] versus metallicity, for AGB models of initial mass $M = 1.3\ M_{\odot}$ (*top panel*), $M = 1.5\ M_{\odot}$ (*middle panel*) and $M = 2.0\ M_{\odot}$ (*bottom panel*). A wide range of ^{13}C-pocket efficiencies is presented. A 1.3 $M_{\odot}$ model undergoes TDU episodes starting from [Fe/H] $\leqslant -0.6$ (see Figs. 2 and 3 of Straniero et al. 2003).

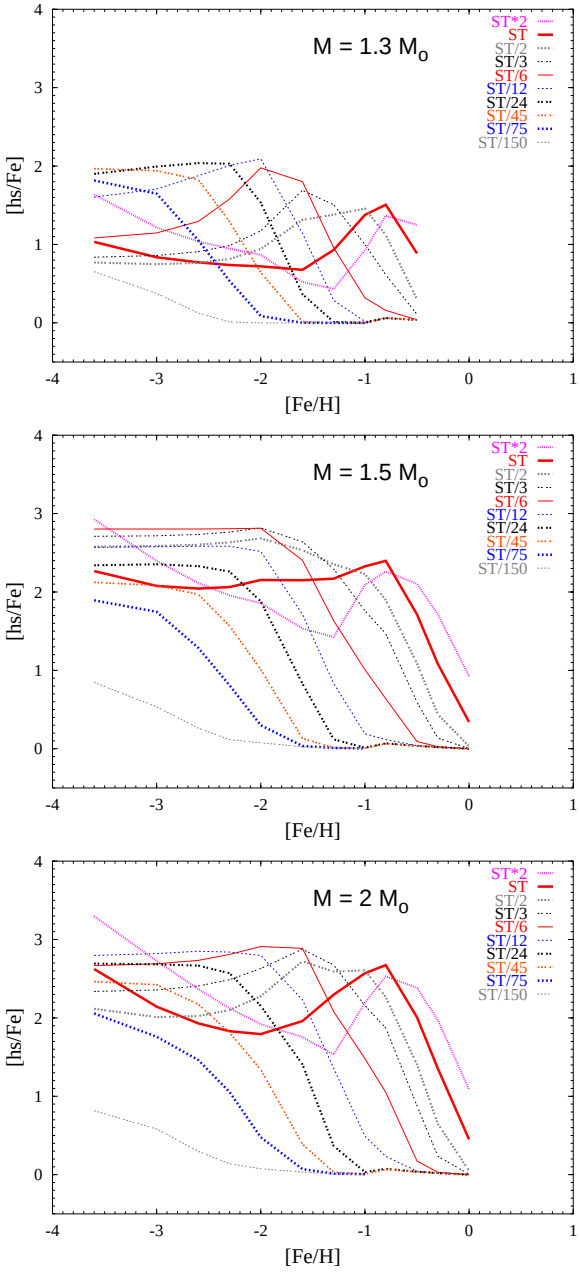

Figure 8. The same as Fig. 7, but for [hs/Fe].

however have a key role in improving the prediction of fluorine (Sect. 5).

3.2 Nb and Zr predictions and their significance.

An intrinsic AGB is a star with high luminosity and low log g that lies on the TP-AGB or Post-AGB phase. An extrinsic AGB is located on the main-sequence or on the red giant branch. In this case, which is the case for CEMP-s stars, the s-process abundances are due to mass transfer from a more massive AGB companion, which now is cooling along the white dwarf sequence (Wallerstein & Dominy 1988). These two classes can be discerned by studying the abundances of two elements: Tc and Nb. Long-lived isotopes fed by the s-process, like ^{99}Tc ($t_{1/2} = 2\times\ 10^5$ yr), can be observed in intrinsic AGB stars, as first discovered by Merrill (1952). As the interpulse phase in LMS has a typical period of the order of 10^4 yr, ^{99}Tc, brought into the surface after the TDU, does not have time to completely decay. Spectroscopic observations of disk metallicity stars were done in the past for MS, S, C(N) stars, in order to search for intrinsic AGBs by detecting Tc lines (Smith & Lambert 1988, 1990; Brown et al. 1990; Busso et al. 2001; Abia et al. 2002).

Another key element to discriminate between intrinsic and extrinsic AGB stars is niobium. According to

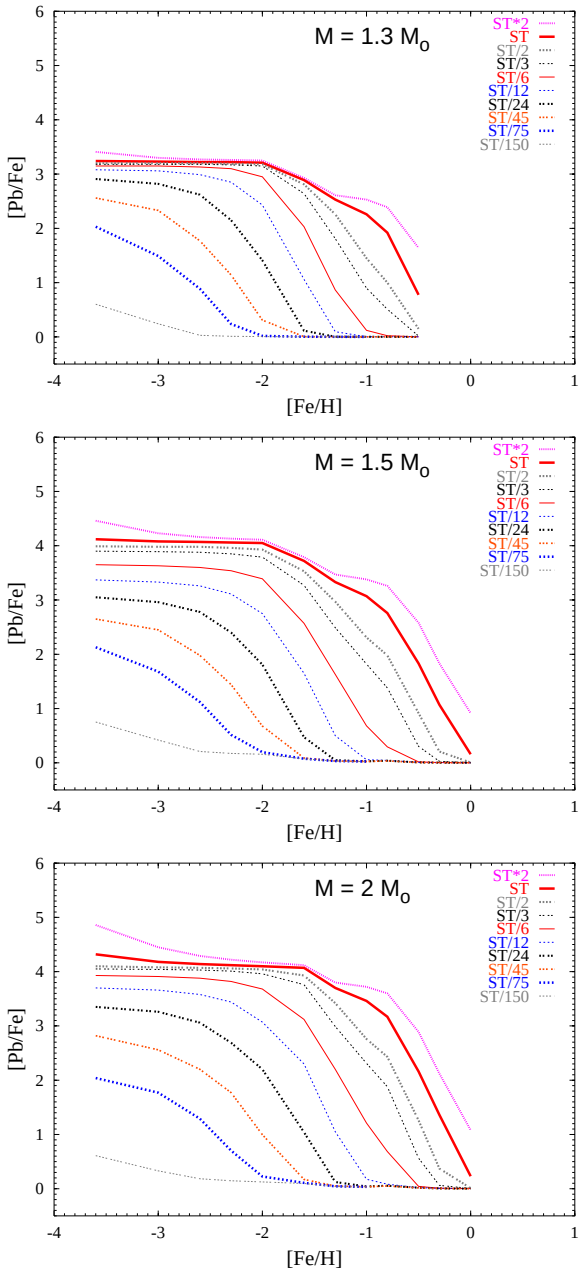

Figure 9. The same as Fig. 7, but for [Pb/Fe].

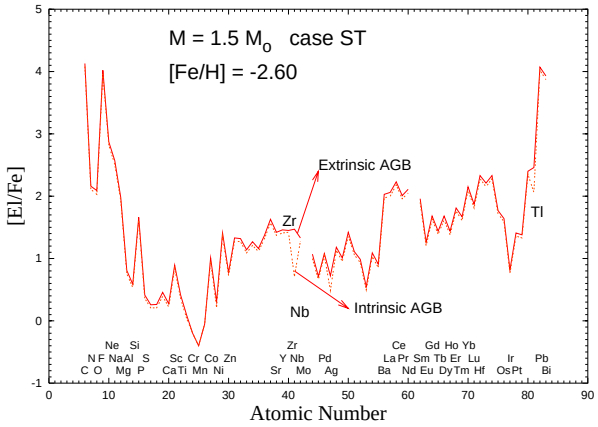

Figure 10. Theoretical predictions for [Zr/Fe] and [Nb/Fe] in an extrinsic (solid line) and an intrinsic (dashed line) AGB, with initial mass $M = 1.5\ M_{\odot}$, and [Fe/H] $= -2.6$. The efficiency of the ^{13}C-pocket has been set to the ST case.

Arlandini et al. (1999), solar Nb (^{93}Nb), which is bypassed by the *s*-process fluence, receives a contribution of 85% from the *s*-process (see also Appendix A) by radiogenic decay of ^{93}Zr ($t_{1/2} = 1.5$ Myr). This latter isotope is strongly fed by the *s*-process because of its low neutron caption cross section (Bao et al. 2000). The long lived isotope ^{93}Zr partially decays into ^{93}Nb during the interpulse phase and, at each TDU, newly synthesised ^{93}Zr is mixed within the envelope. In intrinsic AGB stars, a fraction of Nb is produced in the envelope by the decay of ^{93}Zr. Instead, for extrinsic AGBs, all the ^{93}Zr produced by the *s*-process already decayed into ^{93}Nb. Then, for an intrinsic AGB, such as CEMP-s stars, we expect [Zr/Nb] ~ 1 (dashed line of Fig. 10), while for an extrinsic AGB [Zr/Nb] ~ 0 (solid line of Fig. 10).

3.3 Intrinsic *s*-process indexes

As demonstrated in Sect. 3.1, in AGB stars s-rich material coming from the He-intershell is mixed with the AGB envelope during each TDU and thus [ls/Fe], [hs/Fe] and [Pb/Fe] increase with the number of TDUs. The elemental distribution after each TDU represents therefore the surface composition of the star.

Instead, in extrinsic AGBs, we do not observe the pristine amount of material synthesised since this material may undergo further mixing with the envelope of the extrinsic AGB star. Low mass main-sequence stars have a very thin convective envelope. In this case thermohaline mixing or gravitational settling could dilute the original AGB material (Denissenkov & Pinsonneault 2008; Denissenkov et al. 2009; Stancliffe et al. 2008; Charbonnel & Zahn 2007; Eggleton et al. 2006; Vauclair 2004). Red giants instead have extended convective envelopes in which the original AGB material is diluted. The dilution factor of the AGB material can be calculated using the formula[6]:

$$[\mathrm{El}^{\mathrm{obs}}/\mathrm{Fe}] = \log(10^{[\mathrm{El}_{\mathrm{AGB}}/\mathrm{Fe}]-dil} + 10^{[\mathrm{El}_{\star}/\mathrm{Fe}]}(1-10^{-dil})), \quad (5)$$

where $[\mathrm{El/Fe}]^{\mathrm{obs}}$ is the overabundance measured in the extrinsic star, $[\mathrm{El/Fe}]^{\mathrm{AGB}}$ is the amount of the element 'El' in the AGB envelope. The dilution *dil*, chosen for each star in order to obtain a best fit of the experimental data, is defined as the mass of the convective envelope of the observed star ($M_{\star}^{\mathrm{obs}}$) over the material transferred from the AGB to the companion ($M_{\mathrm{AGB}}^{\mathrm{trans}}$):

[6] This equation is obtained starting from the simple hypothesis that

$$\mathrm{El}_{\star}^{\mathrm{obs}} \cdot M_{\star}^{\mathrm{obs}} = \mathrm{El}_{\mathrm{AGB}}^{\mathrm{env}} \cdot \Delta M_{\mathrm{AGB}}^{\mathrm{trans}} + \mathrm{El}_{\star}^{\mathrm{env}} \cdot M_{\star}^{\mathrm{env}},$$

where $\mathrm{El}_{\star}^{\mathrm{obs}}$ is the mass fraction of the element 'El' observed in the extrinsic star, $\mathrm{El}_{\mathrm{AGB}}^{\mathrm{env}}$ is the mass fraction of the element 'El' in the material transferred from the AGB to the companion, $\mathrm{El}_{\star}^{\mathrm{env}}$ is the mass fraction of the element 'El' in the envelope of the observed star before the mass transfer, $M_{\star}^{\mathrm{obs}}$ is the envelope mass of the observed star, $\Delta M_{AGB}^{\mathrm{trans}}$ is the material transferred from the AGB to the companion, and $M_{\star}^{\mathrm{env}}$ is the envelope mass of the observed star before the mass transfer.

Table 3. The [ls/Fe], [hs/Fe], [Pb/Fe], [hs/ls] and [Pb/hs] predicted ratios by varying the ^{13}C-pocket efficiency, for AGB stellar models of M = 1.3, 1.4, 1.5 and 2 $M_{\odot}$, at [Fe/H] = −2.6.

Mass	^{13}C-pocket	ST×2	ST×1.3	ST	ST/1.5	ST/2	ST/3	ST/4.5	ST/6
M = 1.3 $M_{\odot}$	[ls/Fe]	0.63	0.49	0.41	0.35	0.34	0.41	0.51	0.58
	[hs/Fe]	1.04	0.86	0.77	0.72	0.76	0.91	1.08	1.29
	[Pb/Fe]	3.27	3.24	3.22	3.21	3.20	3.18	3.16	3.13
	[hs/ls]	0.41	0.37	0.36	0.38	0.42	0.51	0.58	0.72
	[Pb/hs]	2.23	2.38	2.45	2.49	2.44	2.27	2.08	1.84
M = 1.4 $M_{\odot}$	[ls/Fe]	1.42	1.22	1.11	1.04	1.05	1.16	1.43	1.65
	[hs/Fe]	1.77	1.54	1.47	1.52	1.69	2.09	2.30	2.41
	[Pb/Fe]	3.86	3.80	3.78	3.75	3.74	3.69	3.62	3.54
	[hs/ls]	0.35	0.33	0.37	0.48	0.64	0.93	0.88	0.76
	[Pb/hs]	2.09	2.26	2.31	2.23	2.05	1.60	1.32	1.13
M = 1.5 $M_{\odot}$	[ls/Fe]	1.69	1.51	1.46	1.51	1.66	2.00	2.25	2.35
	[hs/Fe]	2.11	1.96	2.04	2.42	2.60	2.73	2.83	2.80
	[Pb/Fe]	4.16	4.10	4.07	4.02	3.98	3.88	3.72	3.60
	[hs/ls]	0.42	0.45	0.59	0.91	0.95	0.73	0.59	0.45
	[Pb/hs]	2.05	2.14	2.03	1.60	1.38	1.15	0.89	0.80
M = 2.0 $M_{\odot}$	[ls/Fe]	1.93	1.68	1.52	1.41	1.40	1.51	1.78	2.00
	[hs/Fe]	2.37	2.08	1.93	1.88	2.02	2.41	2.62	2.73
	[Pb/Fe]	4.29	4.18	4.14	4.10	4.07	4.03	3.96	3.88
	[hs/ls]	0.44	0.41	0.41	0.48	0.63	0.90	0.84	0.74
	[Pb/hs]	1.92	2.10	2.21	2.22	2.05	1.62	1.34	1.15

Mass	^{13}C-pocket	ST/9	ST/12	ST/18	ST/24	ST/30	ST/45	ST/75	ST/150
M = 1.3 $M_{\odot}$	[ls/Fe]	0.71	0.89	1.22	1.40	1.49	1.55	1.46	0.49
	[hs/Fe]	1.68	1.88	2.01	2.04	2.02	1.83	1.05	0.13
	[Pb/Fe]	3.07	2.99	2.81	2.62	2.40	1.77	0.89	0.03
	[hs/ls]	0.97	0.99	0.79	0.64	0.53	0.28	-0.40	-0.36
	[Pb/hs]	1.39	1.11	0.80	0.58	0.38	-0.06	-0.16	-0.10
M = 1.4 $M_{\odot}$	[ls/Fe]	1.88	1.99	2.08	2.09	2.06	1.95	1.70	0.82
	[hs/Fe]	2.51	2.49	2.42	2.33	2.25	1.99	1.29	0.21
	[Pb/Fe]	3.40	3.26	3.02	2.81	2.58	2.01	1.12	0.12
	[hs/ls]	0.63	0.50	0.34	0.24	0.19	0.05	-0.41	-0.61
	[Pb/hs]	0.89	0.77	0.60	0.48	0.33	0.02	-0.17	-0.09
M = 1.5 $M_{\odot}$	[ls/Fe]	2.44	2.43	2.35	2.28	2.20	2.05	1.81	1.22
	[hs/Fe]	2.68	2.58	2.45	2.33	2.23	1.97	1.29	0.26
	[Pb/Fe]	3.41	3.26	3.00	2.78	2.56	1.98	1.12	0.21
	[hs/ls]	0.25	0.15	0.10	0.06	0.03	-0.08	-0.52	-0.95
	[Pb/hs]	0.73	0.68	0.55	0.45	0.33	0.01	-0.17	-0.05
M = 2.0 $M_{\odot}$	[ls/Fe]	2.22	2.34	2.45	2.46	2.44	2.32	2.06	1.35
	[hs/Fe]	2.85	2.85	2.75	2.67	2.58	2.17	1.46	0.30
	[Pb/Fe]	3.73	3.58	3.32	3.06	2.79	2.20	1.29	0.18
	[hs/ls]	0.63	0.51	0.30	0.21	0.14	-0.14	-0.60	-1.05
	[Pb/hs]	0.88	0.73	0.57	0.39	0.21	0.03	-0.17	-0.12

$$dil = \log\left(\frac{M_{\star}^{\rm obs}}{\Delta M_{\rm AGB}^{\rm trans}}\right). \quad (6)$$

In this context, the [hs/ls] and [Pb/hs] ratios are extremely valuable indexes for the *s*-process as they are independent both on the TDU efficiency in the AGB star as well as the dilution of the AGB material onto the companion. Moreover, the [hs/ls] ratio may give a constrain on the initial AGB mass because, with increasing the mass (and decreasing the metallicity), the elements of the first *s*-peak receive a significant contribution from the ^{22}Ne(α, n)^{25}Mg neutron source during the convective TP. In Table 3, we list the values of the intrinsic index [hs/ls] at [Fe/H] = −2.6 by changing the ^{13}C-pocket, for various AGB initial masses. The [hs/ls] ratio may give a constraint on the initial mass, and it can be an indicator of the *s*-process efficiency as well. For example, by comparing M = 1.3 and 1.5 $M_{\odot}$, the case ST/12 predicts [hs/ls] $\sim$ 1.0 dex and $\sim$ 0.2 dex, respectively. In Fig. 11, we show the [hs/ls] theoretical predictions versus metallicity for AGB models of M = 1.3, 1.5 and 2.0 $M_{\odot}$. While in disk metallicity stars ([Fe/H] > −1.5), the ratio [hs/ls] provides strong constraints on the mass and on the ^{13}C-pocket efficiency, at low metallicities ([Fe/H] $\leqslant$ −1.5) models characterised by the same [hs/ls] value could show different [Pb/Fe] values. For example, for a M = 1.3 $M_{\odot}$ model at [Fe/H] = −2.5, the ST/3 and ST/30 cases predict the same [hs/ls] $\sim$ 0.5, while they have [Pb/Fe] $\sim$ 3.2 and 2.4, respectively (see Figs. 9 and 11, top panels). Another *s*-process indicator is therefore required to discern between different theoretical models: [Pb/hs] (or [Pb/ls]), (Delaude et al. 2004; Van Eck et al. 2003). In Fig. 12, theoretical predictions of [Pb/hs] versus metallicity are shown for different ^{13}C-pockets and different masses (M = 1.3, 1.5 and 2.0 $M_{\odot}$). These values are also listed in Table 3 at [Fe/H] = −2.6. [Pb/hs] ratio covers a large spread ($0 \lesssim$ [Pb/hs] $\lesssim 2$, Fig. 12). The maximum amount of ^{13}C and ^{14}N in the pocket and different hydrogen profiles (then the amount of ^{13}C and ^{14}N in the tails of the pocket) modify the final *s*-process distribution. This explains possible differences between the range of [hs/ls] and [Pb/hs] predicted by our models and other results presented in the literature (see Bisterzo et al.,

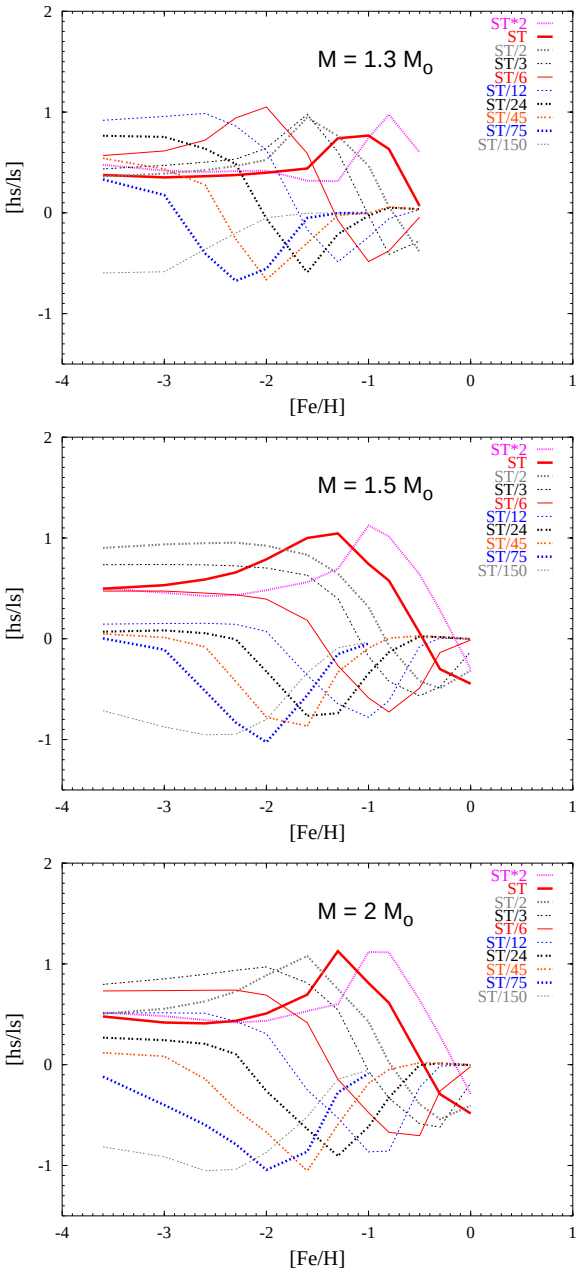

Figure 11. The same as Fig. 7, but for [hs/ls].

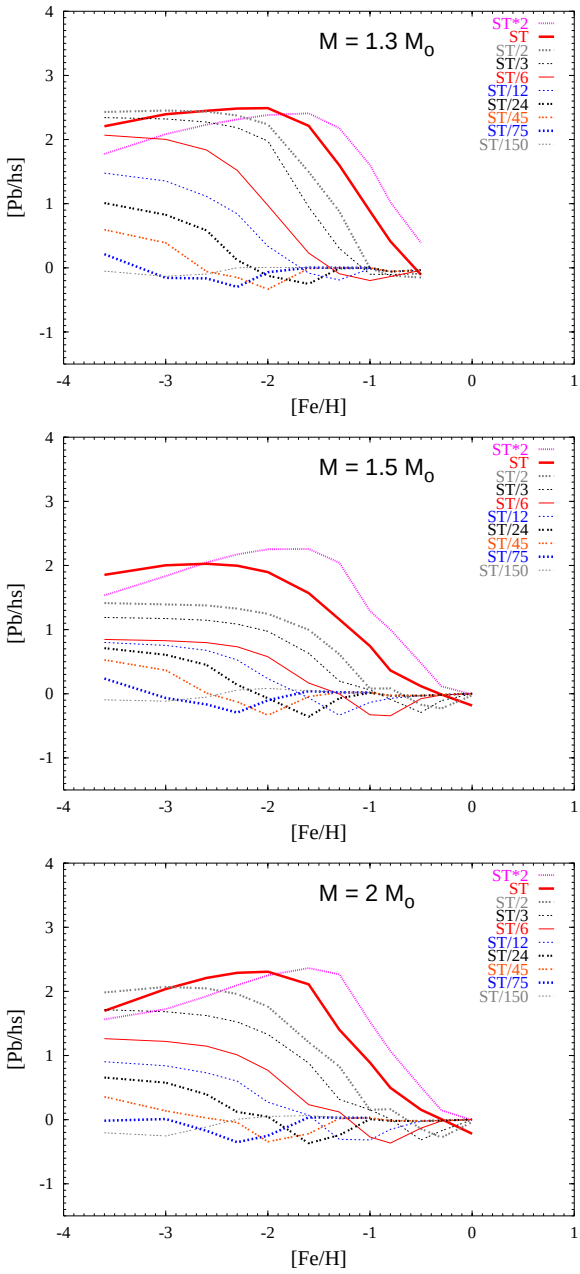

Figure 12. The same as Fig. 7, but for [Pb/hs].

in preparation).

In Figs. C2 and C3 (Appendix C, online material), we show [ls/Fe], [hs/Fe], [Pb/Fe] and [hs/ls] and [Pb/hs] for $M = 5$ $M_\odot$ in the metallicity range $-1.6 \leqslant$ [Fe/H] $\leqslant 0$. Note as the range of ^{13}C-pockets adopted has a negligible influence on the [ls/Fe] ratio (~ 0.3 dex). As expected, lead is more sensible to the ^{13}C-pocket efficiency, showing however a reduced spread with respect to lower stellar masses (Fig. C2, bottom panel, Appendix C, online material). For $M = 3$ $M_\odot$ a behaviour similar to IMS stars is expected for halo metallicities (see Section 2, Fig.3). We show in Figs. C4 and C5 (Appendix C, online material), the three *s*-peak predictions in the metallicity range $-1.6 \leqslant$ [Fe/H] $\leqslant 0$.

4 THE IMPORTANCE OF THE PRIMARY ^{22}NE AT LOW METALLICITIES

At very low metallicities, a primary production of ^{22}Ne, which increases with the initial mass, results in the advanced pulses by the conversion of primary ^{12}C to primary ^{14}N in the H-burning ashes, via ^{14}N(α, γ)^{18}F($\beta^+\nu$)^{18}O and ^{18}O(α, γ)^{22}Ne reaction during TPs (Mowlavi et al. 1999; Gallino et al. 2006; Husti et al. 2007). The production of primary ^{22}Ne is more efficient at lower metallicities because a larger abundance of primary ^{12}C is mixed with the envelope at each TDU episode. The subsequent activation of the H-shell converts almost all CNO nuclei into ^{14}N. This amount of primary ^{14}N is left in the H-burning ashes and during the subsequent TP is converted into primary ^{22}Ne.

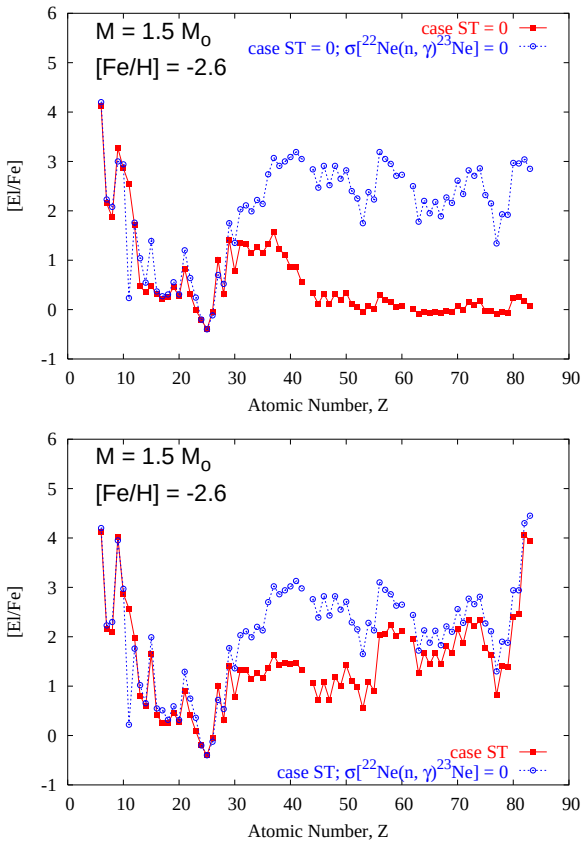

Figure 13. *Top panel:* theoretical predictions of AGB models of $M = 1.5\ M_{\odot}$ for a test case with no ^{13}C-pocket (case ST = 0). The line with squares stands for the ordinary case, while the line with circles corresponds to a case with the cross section of ^{22}Ne(n, γ)^{23}Ne put to zero. *Bottom panel:* The same as top panel but with a ST ^{13}C-pocket.

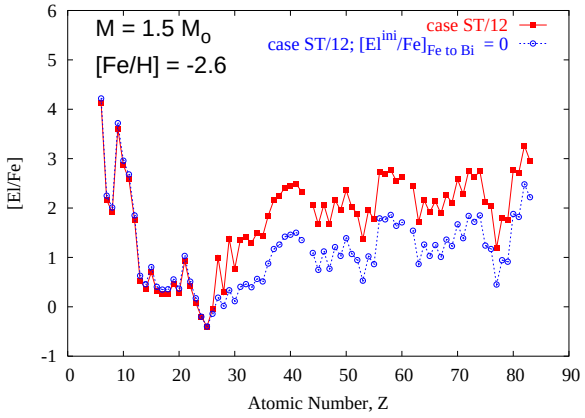

Figure 14. Theoretical predictions of AGB models of $M = 1.5\ M_{\odot}$ and case ST/12. The line with full squares stands for the ordinary case, while the line with empty circles corresponds to a case with the initial abundances of elements from ^{56}Fe to ^{209}Bi put to zero.

To test the effect of neutron captures on ^{22}Ne, we show in Fig. 13, the theoretical prediction for AGB models of $M = 1.5\ M_{\odot}$ and [Fe/H] $= -2.6$, without ^{13}C-pocket (case ST = 0, top panel) and with a case ST (bottom panel). Solid lines represent the ordinary cases, while the dashed lines correspond to cases with the cross section of ^{22}Ne(n, γ)^{23}Ne set to zero. Concerning light elements, this test mainly affect ^{23}Na, which decreases more than 2 dex, thus highlighting the primary production of ^{23}Na via ^{22}Ne(n, γ). For Z $\gtrsim$ 30, the larger amount of available neutrons feeds the production of the elements up to lead (blue dotted lines). This makes ^{22}Ne, as well as ^{23}Na, the main neutron poison at low metallicity during the ^{22}Ne neutron burst. As illustrated in Fig. 13, bottom panel, for a ST case of *s*-process efficiency, ^{22}Ne remains the most efficient neutron poison even inside the ^{13}C-pocket during the interpulse phase. Decreasing the initial AGB mass, the poison effect is visible only for efficient ^{13}C-pocket. For higher metallicities this effect decreases, becoming negligible at [Fe/H] $= -1$ (Gallino et al. 2006).
Primary ^{22}Ne plays a second role at low metallicities, becoming an iron seed producer for a primary *s*-process chain, depending on the adopted ^{13}C-pocket. Even if the neutron capture cross section of ^{22}Ne is very small, not only the light elements as ^{23}Na and the Mg isotopes are produced, but the neutron capture chain extends up to ^{56}Fe, replenishing the starting seed for the production of *s*-elements. This is shown in Fig. 14, for a low ^{13}C-pocket (ST/12) and [Fe/H] $= -2.6$. Even if we set the initial abundances from ^{56}Fe to ^{209}Bi to zero, some primary iron and a consistent amount of primary *s*-elements are produced. When neutrons are largely produced by the ^{13}C(α, n)^{16}O reaction as tests with higher ^{13}C-pockets demonstrate (e.g. a case ST $\times$ 2), a high percentage of *s* elements is primary (produced directly by neutron capture on ^{22}Ne), and the *s*-element abundances are about 0.2 dex lower than the standard case. The primary ^{16}O and ^{12}C produced at low metallicities act also as neutron poison during the pocket (see online material, Fig. C6). We tested also the poison effect of other light elements that show minor or negligible differences.

5 NA AND MG AS INITIAL MASS INDICATORS

As discussed in Section 4, a progressive amount of primary ^{22}Ne is produced in the He-intershell from the CNO cycle during the H-burning shell. The effect is a primary production of ^{23}Na via ^{22}Ne(n,γ)^{23}Na, followed by the nucleosynthesis of Mg via ^{23}Na(n,γ)^{24}Mg, ^{22}Ne(α,n)^{25}Mg and ^{22}Ne(α,γ)^{26}Mg (Mowlavi et al. 1999; Gallino et al. 2006). This chain involves light elements up to P, including Al and Si. In Fig. 15, top panel, we show the [El/Fe] predictions in the region of the light elements, in a stellar mass range $1.2 \leqslant M/M_{\odot} \leqslant 2$, for a case ST and [Fe/H] $= -2.6$. The production of the light elements as Ne, Na, Mg, and P is strongly dependent on the initial AGB mass. In particular, differences higher than 2.5 dex are observed between $M = 1.2$ and $1.5\ M_{\odot}$. The production of primary ^{22}Ne increases at lower metallicity (Fig. 15, bottom panel, for a $M = 1.5\ M_{\odot}$ and a case ST), due to the higher production of ^{22}Ne in the H-burning ashes, thus explaining the slope predicted for [Na/Fe], [Mg/Fe], and other light elements. In particular, Na

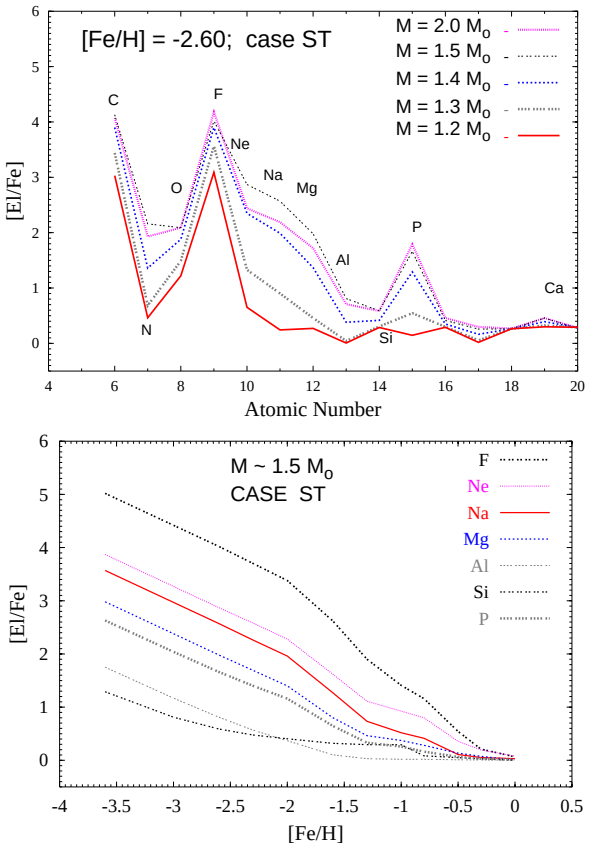

Figure 15. *Top panel:* theoretical predictions of light elements for different initial masses, [Fe/H] = −2.6 and a ST case. *Bottom panel:* theoretical predictions of the light elements in the region between Ne up to Si as a function of metallicity, for an AGB model of $M = 1.5\ M_{\odot}$ and ST case.

(and Mg) are indicator of the mass of the AGB companion which polluted the observed CEMP-s stars (Bisterzo et al. 2006b; Paper II).

We also remind that Na can be produced in IMS models by hot bottom burning (Sugimoto 1971; Iben 1973; Karakas & Lattanzio 2003; Ventura & D'Antona 2005), which is not included in our models.

Fig. 15, top panel, shows a huge amount of fluorine produced in AGB stars via the chain ^{18}O(p, α)^{15}N(α, γ)^{19}F, where protons are produced via ^{14}N(n, p)^{14}C, neutrons via ^{13}C(α, n)^{16}O reaction and ^{18}O via the chain ^{14}N(α, γ)^{18}F(β^+)^{18}O (Lugaro et al. 2004, 2008; Abia et al. 2009). With the addition of proton captures in the network, the prediction of [F/Fe] increased by about 2 dex. We estimate a further increase by about 0.3 dex due to the primary ^{13}C from H shell (Cristallo et al. 2009a). Further discussions and improvement about fluorine, accounting for recent experimental measurements of reaction rates involved (La Cognata et al. 2010), will be given in a forthcoming paper.

6 CONCLUSIONS

We presented theoretical results of updated AGB stellar nucleosynthesis models in a mass range $1.3 \leqslant M/M_{\odot} \lesssim 3.0$ and metallicities $-3.6 \leqslant$ [Fe/H] $\leqslant -1$. We analysed the behaviour of the three *s*-process peaks and their ratios [hs/ls] and [Pb/hs] as the initial AGB mass and the ^{13}C-pocket change. Then, we presented in detail the abundance composition in the envelope of all the elements, from carbon to bismuth.

We find a high [C/Fe] already after the first TDU episode of models at low metallicities, due to the increase with the decrease in metallicity of the primary ^{12}C and to an efficient TDU. We discuss the deep impact of ^{22}Ne as neutron seed and neutron poison by decreasing the metallicity. This primary ^{22}Ne increases with the initial mass and as a consequence Na (and Mg) are strongly produced by decreasing the metallicity. This makes of Na and Mg good indicators for the initial mass of the AGB star.

The three *s*-peaks are strongly dependent on the choice of the ^{13}C-pocket as well as the initial mass and the metallicity. [ls/Fe], [hs/Fe] and [Pb/Fe] do not have a linear behaviour with decreasing metallicity, and, depending on the ^{13}C-pocket efficiency, they can cover a large range of values. Especially [Pb/Fe], largely produced by decreasing the metallicity, can reach 4.5 dex. By increasing the AGB mass and then the temperature at the bottom of the thermal pulse, [ls/Fe] receives an increasing contribution by the ^{22}Ne(α, n)^{25}Mg reaction. Two intrinsic *s*-process indexes, [hs/ls] and [Pb/hs], are needed in order to characterise the *s* distribution, independent on the dilution of the AGB material onto the companion and on the TDU efficiency. The [hs/ls] ratio may give a constraint on the initial mass, and it can be an indicator of the *s*-process efficiency as well, while [Pb/hs] gives information about the efficiency of the ^{13}C-pocket only.

As well as ls, hs, and Pb, we predict two peaks at Sn and Hf – W, which receive a significant contribution from the *s*-process. Also bismuth is synthesised in these objects via neutron capture on ^{208}Pb. We remark the importance of Nb measurement in CEMP-s stars, because an extrinsic AGB has [Zr/Fe] = [Nb/Fe] (e.g. CS 29497-030 by Ivans et al. 2005, see Paper II). We refer to Paper II for a comparison between our AGB models and spectroscopic observations in CEMP-*s* stars.

This study together with Paper II are part of a series of works, planned to provide a complete picture of the *s*-process nucleosynthesis in AGB stars. We are planning to extend the analysis from CEMP-*s* stars up to solar metallicities. We will compare AGB predictions presented here with spectroscopic observations of *s*-enhanced disk stars of different spectral classification (e.g CH and Barium binary stars, intrinsic post-AGBs, extrinsic or intrinsic MS, S, C stars; for previous analysis see Busso et al. 1995, 2001 and Abia et al. 2001). As last analysis, we will present update Galactic chemical evolution results, with AGB yields of different masses and metallicities. From the whole spectrum of these studies, we aim at better understanding the AGB nucleosynthesis.

ACKNOWLEDGMENTS

We thank Dr. Maria Lugaro for helpful comments and discussions which have helped improving the clarity and focus of this paper, and, in particular, which motivated us to im-

prove the network by introducing protons. This work was supported by the Italian MIUR-PRIN 2006 Project 'Late Phases of Stellar Evolution: Nucleosynthesis in Supernovae, AGB Stars, Planetary Nebulae'.

REFERENCES

Abia, C., Busso, M., Gallino, R., Domínguez, I., Straniero, O., Isern, J. 2001, ApJ, 559, 1117
Abia, C. et al. 2002, Apj, 579, 817
Abia, C., Recio-Blanco, A., de Laverny, P., Cristallo, S., Domínguez, I., Straniero, O. 2009, ApJ, 694, 971
Alpizar-Vicente, A. M. et al. 2008, Phys. Rev. C, 77, 5806
Anders, E., & Grevesse, N. 1989, GCA, 53, 197
Andrievsky, S. M., Spite, M., Korotin, S. A., Spite, F., François, P., Bonifacio, P., Cayrel, R., Hill, V. 2009, A&A, 494, 1083
Angulo, C. et al. 1999, Nucl. Phys. A, 656, 3
Aoki, W., Bisterzo, S., Gallino, R., Beers, T. C., Norris, J. E., Ryan, S. G., Tsangarides, S. 2006, ApJ, 650, 127
Arlandini, C., Käppeler, F., Wisshak, K., Gallino, R., Lugaro, M., Busso, M., Straniero, O. 1999, ApJ, 525, 886
Bao, Z. Y., Beer, H., Käppeler F., Voss, F., Wisshak, K. 2000, Atomic Data & Nuclear Data Tables, 76, 70
Beers, T. C., Preston, G. W., & Shectman, S. A. 1992, AJ, 103, 1987
Beers, T. C., & Christlieb, N. 2005, ARA&A, 43, 531
Beers, T. C., Sivarani, T., Marsteller, B., Lee, Y., Rossi, S., Plez, B. 2007, AJ, 133, 1193
Bergemann, M., & Gehren, T. 2008, A&A, 492, 823
Bisterzo, S., Käppeler F., Gallino, R., Heil, M., Domingo-Pardo, C. 2006a, Nuclei in the Cosmos - IX, Proceedings of Science (PoS), 77
Bisterzo, S., Gallino, R., Straniero, O., Aoki, W., Ryan, S., Beers, T. C. 2006b, AIP Conference Proceedings, 847, 368
Bisterzo, S., Käppeler F., Gallino, R., Heil, M., Domingo-Pardo, C., Vockenhuber, C., Wallner, A. 2007, International Conference on Nuclear Data for Science and Technology, DOI: 10.1051/ndata:07488
Bisterzo, S., & Gallino, R. 2008, AIP Conference Proceedings, 1001, 131
Bisterzo, S., Gallino, R., Straniero, O., Ivans, I. I., Preston, G. W., Aoki, W. 2008, AIP Conference Proceedings, 990, 330
Bisterzo, S., Gallino, R., Straniero, O., Aoki, W. 2009, PASA, 26, 314
Bloecker, T. 1995, A&A, 297, 727
Boothroyd, A. I., & Sackmann, I.-J. 1988, ApJ, 328, 653
Brown, J. A., Smith, V. V., Lambert, D. L., Dutchover, E. Jr., Hinkle, K. H., Johnson, H. R. 1990, AJ, 99, 1930
Burbidge, E. M., Burbidge, G. R., Fowler, W. A., Hoyle, F. 1957, Rev. Mod. Phys., 29, 547
Busso, M., Lambert, D. L., Beglio, L., Gallino, R., Raiteri, C. M., Smith, V. V. 1995, ApJ, 446, 775
Busso, M., Gallino, R., & Wasserburg, G. J. 1999, ARA&A, 37, 239
Busso, M., Gallino, R., Lambert, D. L., Travaglio, C., Smith, V.V. 2001, ApJ, 557, 802
Campbell, S. W., & Lattanzio, J. C. 2008, A&A, 490, 769
Cayrel, R. et al. 2004, A&A, 416, 1117
Charbonnel, C. & Zahn, J.,-P. 2007, A&A, 467, 15
Chieffi, A., & Straniero, O. 1989, ApJs, 71, 47
Christlieb, N. 2003, Rev. Mod. Astron., 16, 191
Clayton, D. D. 1961, Ann. Phys., 12, 331
Clayton, D. D. 1968, "Principles of Stellar Evolution and Nucleosynthesis", ed. New York: McGraw-Hill
Clayton, D. D. 1988, MNRAS, 234, 1
Cristallo, S., Straniero, O., Gallino, R., Piersanti, L., Domínguez, I., Lederer, M. T. 2009a, ApJ, 696, 797
Cristallo, S., Piersanti, L., Straniero, O., Gallino, R., Domínguez, I., Käppeler, F. 2009b, PASA, 26, 139
Denissenkov, P. A., & Tout, C. A. 2003, MNRAS, 340, 722
Denissenkov, P. A., & Pinsonneault, M. 2008, ApJ, 679, 1541
Denissenkov, P. A., Pinsonneault, M. & MacGregor, K. B. 2009, ApJ, 696, 1823
Delaude, D., Gallino, R., Cristallo, S., Straniero, O., Husti, L., Ryan, S. 2004, Mem. Soc. Astronom. It., 74, 706
Domingo-Pardo, C. et al. 2006, Phys. Rev. C, 74, 5802
Domingo-Pardo, C. et al. 2007a, Phys. Rev. C, 75, 5806
Domingo-Pardo, C. et al. 2007b, Phys. Rev. C, 76, 5805
Domínguez, I., Chieffi, A., Limongi, M., Straniero, O. 1999, ApJ, 524, 226
Eggleton, P. P., Dearborn, D. S. P., & Lattanzio, J. C. 2006, Science, 314, 1580
François, P., Matteucci, F., Cayrel, R., Spite, M., Spite, F., Chiappini, C. 2004, A&A, 421, 613
Fujimoto, M. Y., Ikeda, Y., & Iben, I. Jr., 2000, ApJ, 529, 25
Gallino, R., Arlandini, C., Busso, M., Lugaro, M., Travaglio, C., Straniero, O., Chieffi, A., Limongi, M. 1998, ApJ, 497, 388
Gallino, R., Wasserburg, G. J., Busso, M., Straniero, O. 1995, IAUS, 228, 461
Gallino, R., Bisterzo, S., Husti, L., Käppeler, F., Cristallo, S., Straniero, O. 2006, Nuclei in the Cosmos - IX, Proceedings of Science (PoS), 100
Goriely, S., & Mowlavi, N. 2000, A&A, 362, 599
Goriely, S., & Siess, L. 2004, A&A, 421, 25
Hale, S. E., Champagne, A. E., Iliadis, C., Hansper, V. Y.,; Powell, D. C., Blackmon, J. C. 2002, Phys. Rev. C, 65, 015801
Heil, M., Winckler, N., Dababneh, S. Käppeler, F., Wisshak, K., Bisterzo, S., Gallino, R., Davis, A. M., Rauscher, T. 2008, ApJ, 673, 434
Helfer, H. L., Wallerstein, G., & Greenstein, J.L. 1959, ApJ, 129, 700
Herwig, F., Blöcker, T., Schönberner, D., El Eid, M. 1997, A&A, 324, L81
Herwig, F. 2000, A&A, 360, 952
Herwig, F. 2004, ApJs, 155, 651
Hollowell, D., Iben, I. Jr., Fujimoto, M. Y. 1990, ApJ, 351, 245
Husti, L., Gallino, R., Bisterzo, S., Cristallo, S., Straniero, O. 2007, Mem. Soc. Astronom. It., 78, 523
Husti, L., & Gallino, R. 2008, AIP Conference Proceedings, 1001, 139
Iben, I. Jr. 1973, ApJ, 185, 209
Iben, I. Jr., & Renzini, A. 1983, ARA&A, 21, 271
Ivans, I. I., Sneden, C., Gallino, R., Cowan, J. J., Preston, G. W. 2005, ApJ, 627, 145
Iwamoto, N., Kajino, T., Mathews, G. J., Fujimoto, M. Y., Aoki, W. 2004, ApJ, 602, 377

Käppeler, F., Beer, H., Wisshak, K., Clayton, D. D., Macklin, R. L., Ward, R. A. 1982, ApJ, 257, 821
Käppeler, F., Wiescher, M., Giesen, U., Goerres, J., Baraffe, I., El Eid, M., Raiteri, C. M., Busso, M., Gallino, R., Limongi, M., Chieffi, A. 1994, ApJ, 437, 396
Karakas, A., & Lattanzio, J. 2003, PASA, 20, 279
Karakas, A., & Lattanzio, J. 2007, PASA, 24, 103
Koehler, P. E. & O'brien, H. A. 1989, Phys. Rev. C, 39, 1655
La Cognata, M. et al. 2010, ApJ, 708, 796
Langer, N., Heger, A. Wellstein, S., Herwig, F. 1999, A&A, 346, L37
Lattanzio, J., Frost, C., Cannon, R., Wood, P. 1996, Mem. Soc. Astronom. It., 67, 729
Lau, H. H. B., Stancliffe, R. J., & Tout, C. A. 2009, MNRAS, 396, 1046
Lee Y. S. et al. 2008a, AJ, 136, 2022
Lee Y. S. et al. 2008b, AJ, 136, 2050
Lodders, K. 2003, ApJ, 591, 1220
Lugaro, M. et al. 2004, ApJ, 615, 934
Lugaro, M. et al. 2008, A&A, 484, 27
Mashonkina, L. 2008, A&A, 478, 529
Merrill, S. P. W. 1952, ApJ, 116, 21
Mosconi, M. et al. 2008, JPhG, 35, 4015
Mowlavi, N. 1999, A&A, 350, 73
Reimers, D. 1977, A&A, 61, 217
Roederer, I. U. et al. 2008, ApJ, 679, 1549
Short, C. I., & Hauschildt, P. H. 2006, ApJ, 641, 494
Schwarzschild, M., & Härm, R. 1965, ApJ, 142, 855
Schwarzschild, M., & Härm, R. 1967, ApJ, 150, 961
Serminato, A., Gallino, R., Travaglio, C., Bisterzo, S., Straniero, O. 2009, PASA, 26, 153
Smith, V. V., & Lambert, D. L. 1988, ApJ, 333, 219
Smith, V. V., & Lambert, D. L. 1990, ApJ, 72, 387
Sneden, C., Cowan, J. J., & Gallino, R. 2008, ARA&A, 46, 241
Stancliffe, R. J., & Jeffery, C. S. 2007, MNRAS, 375, 1280
Stancliffe, R. J. & Glebbeek, E. 2008, MNRAS, 389, 1828
Straniero, O., Gallino, R., Busso, M., Chieffi, A., Raiteri, C. M., Limongi, M., Salaris, M. 1995, ApJ, 440, 85
Straniero, O., Chieffi, A., Limongi, M., Busso, M., Gallino, R., Arlandini, C. 1997, ApJ, 478, 332
Straniero, O., Limongi, M., Chieffi, A., Domínguez, I., Busso, M., Gallino, R. 2000, Mem. Soc. Astronom. It., 71, 719
Straniero, O., Domínguez, I., Cristallo, S., Gallino, R. 2003, PASA, 20, 389
Straniero, O., Gallino, R, & Cristallo, S. 2006, Nucl. Phys. A, 777, 311
Sugimoto, D. 1971, Progress of Theoretical Physics, 45, 761
Tagliente, G. et al. 2008a, Phys. Rev. C, 77, 035802
Tagliente, G. et al. 2008b, Phys. Rev. C, 78, 045804
Travaglio, C., Gallino, R., Busso, M., Gratton, R. 2001, ApJ, 549, 346
Travaglio, C., Gallino, R., Arnone, E., Cowan, J., Jordan, F., Sneden, C. 2004, ApJ, 601, 684
Thompson, I. B. et al. 2008, ApJ, 667, 556
Van Loon, J. Th. 2006, Cosmology ASP Conference Series, 353, 211
Vassiliadis, E., & Wood, P. R. 1993, ApJ, 413, 641
Vauclair, S. 2004, ApJ, 605, 874
Ventura, P., & DAntona, F. 2005, A&A, 431, 279
Wallerstein, G., & Dominy, J. F. 1988, ApJ, 330, 937
York, D. G. et al. 2000, AJ, 120, 1579
Van Eck, S., Goriely, S., Jorissen, A., Plez, B. 2003, A&A, 404, 29

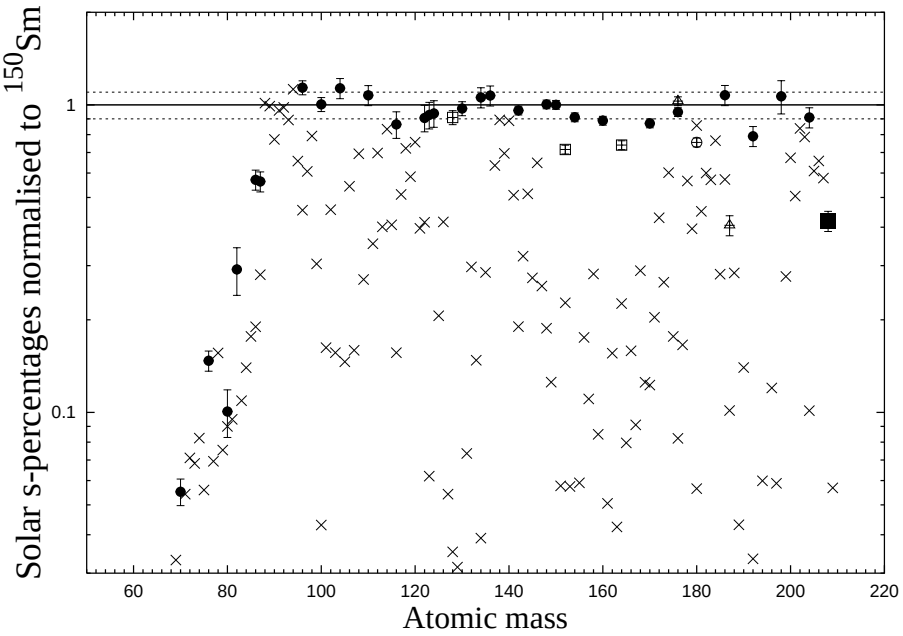

Figure A1. Solar s% normalized to ^{150}Sm versus atomic mass for the solar main component as in Arlandini et al. (1999), updated to 2009.

APPENDIX A: SOLAR *S*-PROCESS CONTRIBUTION

In Table A1, we show the best representation of the solar main component with theoretical predictions in percentage for elements from Sr to Bi for an average between $M = 1.5$ and 3 $M_{\odot}$ at half solar metallicity and a case ST. Here, the main-*s* percentages presented by Arlandini et al. (1999), stellar model (reported as comparison in Col. 3), are updated with new solar abundances and a network upgraded to 2009 (Col. 4). The results by Bisterzo et al. (2006a) have been further updated with the recent cross sections measurement of ^{62}Ni (Alpizar-Vicente et al. 2008), ^{90,91}Zr (Tagliente et al. 2008a,b), ^{186,187,188}Os isotopes (Mosconi et al. 2008), ^{204,206,207}Pb (Domingo-Pardo et al. 2006, 2007a,b), ^{209}Bi(n, γ)^{210}Bi^{g} (Bisterzo et al. 2007) (see also KADoNiS, Karlsruhe Astrophysical Database of Nucleosynthesis in Stars, web address http://nuclear-astrophysics.fzk.de/kadonis/.). The case ST at [Fe/H] = -0.3 gives a [hs/ls] = -0.25 (Col. 4, and Fig. 11, middle panel). In Col. 5 we report the normalization of the main-*s* percentages to europium in logarithmic scale, [El/Eu]. As shown in Col. 4, only $\sim 6\%$ of solar europium is produced by the *s*-process, and it is considered a typical *r*-process element. The normalization to europium highlights the amount of a pure *s*-process contribution to each element [El/Eu]$_{\rm s}$. This [El/Eu] ratio is useful to compare our theoretical predictions with spectroscopic observations, especially in CEMP-*s* (and CEMP-*s*+*r*) stars, to understand if there is competition between *r*- and *s*-process (see Table 1 and Paper II). A pure *s*-process contribution predicts [La/Eu]$_{\rm s}$ = 1.08 at [Fe/H] = -0.3, and $0.8 \leqslant$ [La/Eu]$_{\rm s}$ $\leqslant 1.1$ at [Fe/H] = -2.6 (see Table 1, Cols. 7 to 10). If lower [La/Eu]$_{\rm s}$ values are observed, this indicate stars that experienced an important *r*-process contribution in addition to the *s*-process enhancements.

The same model presented in Table A1, is shown in Fig. A1 for isotopes from Sr to Bi normalised to the *s*-only nucleus ^{150}Sm. The full circles are the *s*-only nuclei. We adopted different symbols for ^{128}Xe, ^{152}Gd, and ^{164}Er, which have a not negligible p contribution (10% for Xe), for ^{176}Lu, a long-lived isotope (3.8×10^{10} y) which decays into ^{176}Hf, for ^{187}Os, which is affected by the long-lived decay of ^{187}Re (5×10^{10} y), and for ^{180}Ta, which receives also contributions from the *p*-process and from ν-interactions in massive stars. The black full square corresponds to ^{208}Pb, which receives a contribution of about 50% by the strong-*s* component (Travaglio et al. 2001, 2004; Serminato et al. 2009).

Table A1. Theoretical predictions in percentage for elements from Sr to Bi, (the label 'El' stands for a generic elements) adopted to reproduce the main component obtained by an average of $M = 1.5$ and 3.0 $M_{\odot}$ models ($M_{\rm aver}$) at [Fe/H] = −0.3 (case ST as in Arlandini et al. 1999, stellar model, Col. 3), improved with cross section measurements and solar abundances upgraded to 2009 (Col. 4; see text of this Appendix). In Col. 5 we report the normalization of the updated main-*s* percentages to europium in logarithmic scale, [El/Eu].

		Arlandini ($M_{\rm aver}$) [Fe/H] = −0.3	Updated [Fe/H] = −0.3	Updated
El	Z	% ST	% ST	[El/Eu] ST
(1)	(2)	(3)	(4)	(5)
Sr	38	85.0	93.1	1.21
Y	39	92.0	99.0	1.23
Zr	40	83.0	88.1	1.18
Nb	41	85.0	89.3	1.19
Mo	42	50.0	54.8	0.98
Ru	44	32.0	34.1	0.77
Rh	45	14.0	15.6	0.43
Pd	46	46.0	49.4	0.93
Ag	47	20.0	21.3	0.56
Cd	48	52.0	64.0	1.04
In	49	35.0	39.0	0.83
Sn	50	65.0	65.6	1.05
Sb	51	25.0	25.3	0.64
Te	52	17.0	18.2	0.50
I	53	5.3	5.4	-0.03
Xe	54	17.0	17.0	0.47
Cs	55	15.0	14.8	0.41
Ba	56	81.0	84.1	1.16
La	57	62.0	69.5	1.08
Ce	58	77.0	80.7	1.14
Pr	59	49.0	50.8	0.94
Nd	60	56.0	56.7	0.99
Sm	62	29.0	30.9	0.73
Eu	63	5.8	5.8	0.00
Gd	64	15.0	11.0	0.28
Tb	65	7.2	8.5	0.17
Dy	66	15.0	14.4	0.39
Ho	67	7.8	8.0	0.14
Er	68	17.0	18.2	0.50
Tm	69	13.0	12.5	0.33
Yb	70	33.0	39.4	0.83
Lu	71	20.0	19.9	0.54
Hf	72	56.0	58.9	1.01
Ta	73	41.0	45.0	0.89
W	74	56.0	63.8	1.04
Re	75	8.9	16.9	0.46
Os	76	9.4	11.9	0.31
Ir	77	1.4	1.5	-0.59
Pt	78	5.1	6.4	0.04
Au	79	5.8	5.9	0.01
Hg	80	61.0	63.2	1.04
Tl	81	76.0	66.1	1.06
Pb	82	46.0	49.9	0.93
Bi	83	4.9	5.7	-0.01
[hs/ls]		-0.27	-0.25	

APPENDIX B: DATA TABLES

B1 [El/Fe] predictions as the ^{13}C-pocket changes

In the following Tables we list the theoretical surface predictions [El/Fe] for four initial AGB masses at [Fe/H] = −2.6, for elements from helium to bismuth: $M^{\rm AGB}_{\rm ini} = 1.3\ M_{\odot}$ (n5) (Table B1), $M^{\rm AGB}_{\rm ini} = 1.4\ M_{\odot}$ (n10) (Table B2), $M^{\rm AGB}_{\rm ini} = 1.5\ M_{\odot}$ (n20) (Tables B3), $M^{\rm AGB}_{\rm ini} = 2.0\ M_{\odot}$ (n26) (Tables B4), where '*ni*' is the number of TPs with TDU. Columns correspond to the different results obtained using a wide range of ^{13}C-pockets (ST×2 down to ST/150). The case ST/150 mainly shows the ^{22}Ne(α, n)^{25}Mg neutron source contribution.

Table B1. Theoretical [El/Fe] predictions from He to Bi for $M_{\rm ini}^{\rm AGB} = 1.3\ M_{\odot}$ (which undergoes 5 TPs with TDU, n5) and [Fe/H] = −2.6 models, as the ^{13}C-pocket changes (ST×2 down to ST/150).

El	Z	ST*2	ST*1.3	ST	ST/1.5	ST/2	ST/3	ST/4.5	ST/6	ST/9	ST/12	ST/18	ST/24	ST/30	ST/45	ST/75	ST/150
He	4	0.06	0.06	0.06	0.06	0.06	0.06	0.06	0.05	0.06	0.06	0.06	0.06	0.06	0.06	0.06	0.05
C	6	3.44	3.44	3.44	3.44	3.43	3.43	3.43	3.43	3.43	3.43	3.43	3.43	3.43	3.43	3.43	3.43
N	7	0.68	0.68	0.68	0.68	0.68	0.68	0.68	0.68	0.68	0.68	0.68	0.68	0.68	0.68	0.68	0.68
O	8	1.54	1.51	1.49	1.46	1.44	1.42	1.40	1.38	1.37	1.36	1.35	1.34	1.33	1.33	1.32	1.32
F	9	3.63	3.60	3.57	3.52	3.49	3.43	3.38	3.33	3.25	3.19	3.10	3.03	2.97	2.87	2.72	2.45
Ne	10	1.38	1.35	1.33	1.31	1.30	1.29	1.28	1.28	1.27	1.27	1.26	1.26	1.26	1.26	1.26	1.25
Na	11	0.98	0.94	0.90	0.86	0.84	0.80	0.77	0.75	0.73	0.71	0.69	0.68	0.67	0.65	0.64	0.61
Mg	12	0.50	0.48	0.46	0.44	0.42	0.40	0.39	0.38	0.36	0.35	0.35	0.34	0.34	0.33	0.33	0.33
Al	13	0.06	0.05	0.04	0.03	0.03	0.02	0.02	0.02	0.01	0.01	0.01	0.01	0.01	0.01	0.01	0.01
Si	14	0.32	0.31	0.31	0.30	0.30	0.29	0.29	0.29	0.29	0.29	0.29	0.29	0.29	0.29	0.29	0.29
P	15	0.81	0.65	0.55	0.42	0.36	0.29	0.24	0.22	0.19	0.18	0.16	0.14	0.13	0.11	0.08	0.04
S	16	0.31	0.30	0.30	0.30	0.30	0.29	0.29	0.29	0.29	0.29	0.29	0.29	0.29	0.29	0.29	0.29
Cl	17	0.07	0.06	0.06	0.05	0.05	0.05	0.04	0.04	0.04	0.04	0.04	0.05	0.05	0.05	0.06	0.05
Ar	18	0.27	0.26	0.26	0.26	0.26	0.26	0.26	0.26	0.26	0.26	0.26	0.26	0.26	0.26	0.26	0.26
K	19	0.33	0.33	0.32	0.32	0.32	0.32	0.31	0.31	0.31	0.31	0.31	0.31	0.31	0.31	0.31	0.31
Ca	20	0.29	0.29	0.29	0.29	0.29	0.29	0.29	0.29	0.29	0.29	0.29	0.29	0.29	0.29	0.29	0.29
Sc	21	0.39	0.36	0.34	0.31	0.29	0.26	0.24	0.23	0.22	0.22	0.23	0.24	0.24	0.24	0.22	0.16
Ti	22	0.28	0.27	0.27	0.26	0.26	0.26	0.26	0.26	0.26	0.27	0.27	0.27	0.27	0.27	0.26	0.25
V	23	0.02	0.01	0.01	0.01	0.00	0.00	0.00	0.00	0.01	0.01	0.01	0.01	0.01	0.00	0.00	0.00
Cr	24	-0.20	-0.20	-0.20	-0.20	-0.20	-0.20	-0.20	-0.20	-0.20	-0.20	-0.20	-0.20	-0.20	-0.20	-0.20	-0.20
Mn	25	-0.40	-0.40	-0.40	-0.40	-0.40	-0.40	-0.40	-0.40	-0.40	-0.40	-0.40	-0.40	-0.40	-0.40	-0.40	-0.40
Fe	26	0.00	0.00	0.00	0.00	0.00	0.00	0.00	0.00	0.00	0.00	0.00	0.00	0.00	0.00	0.00	0.00
Co	27	0.43	0.43	0.43	0.42	0.42	0.41	0.39	0.38	0.36	0.35	0.33	0.31	0.30	0.28	0.27	0.25
Ni	28	0.10	0.09	0.08	0.08	0.07	0.06	0.05	0.04	0.04	0.03	0.03	0.02	0.02	0.02	0.02	0.01
Cu	29	0.86	0.83	0.80	0.76	0.73	0.67	0.61	0.56	0.50	0.45	0.39	0.36	0.34	0.32	0.33	0.31
Zn	30	0.38	0.34	0.31	0.26	0.23	0.18	0.14	0.12	0.09	0.07	0.06	0.05	0.06	0.08	0.12	0.11
Ga	31	0.83	0.76	0.70	0.60	0.54	0.43	0.34	0.29	0.22	0.19	0.16	0.17	0.20	0.32	0.41	0.38
Ge	32	0.81	0.72	0.65	0.54	0.47	0.36	0.28	0.23	0.18	0.16	0.15	0.18	0.24	0.41	0.49	0.43
As	33	0.64	0.55	0.48	0.37	0.31	0.22	0.16	0.13	0.10	0.09	0.10	0.14	0.21	0.37	0.43	0.35
Se	34	0.72	0.61	0.52	0.40	0.32	0.23	0.17	0.15	0.13	0.13	0.15	0.24	0.35	0.55	0.60	0.45
Br	35	0.62	0.51	0.43	0.32	0.25	0.17	0.13	0.11	0.10	0.10	0.13	0.21	0.31	0.50	0.54	0.38
Kr	36	0.70	0.56	0.46	0.33	0.27	0.22	0.21	0.22	0.24	0.26	0.36	0.50	0.63	0.79	0.79	0.47
Rb	37	0.83	0.67	0.55	0.41	0.35	0.31	0.32	0.34	0.37	0.41	0.54	0.71	0.85	1.01	0.99	0.57
Sr	38	0.63	0.49	0.40	0.31	0.29	0.32	0.39	0.45	0.55	0.69	1.00	1.20	1.32	1.42	1.38	0.63
Y	39	0.63	0.49	0.41	0.34	0.33	0.39	0.49	0.56	0.68	0.84	1.17	1.37	1.47	1.55	1.48	0.57
Zr	40	0.63	0.49	0.41	0.35	0.35	0.42	0.52	0.59	0.74	0.94	1.27	1.43	1.51	1.55	1.43	0.41
Nb	41	0.66	0.51	0.43	0.37	0.37	0.44	0.55	0.62	0.78	0.98	1.32	1.48	1.55	1.59	1.46	0.39
Mo	42	0.55	0.42	0.34	0.29	0.29	0.36	0.46	0.52	0.68	0.89	1.21	1.35	1.41	1.42	1.26	0.23
Ru	44	0.40	0.29	0.23	0.18	0.18	0.22	0.29	0.34	0.46	0.65	0.94	1.07	1.13	1.15	1.00	0.12
Rh	45	0.21	0.14	0.10	0.08	0.07	0.10	0.13	0.16	0.25	0.39	0.63	0.75	0.82	0.83	0.70	0.05
Pd	46	0.43	0.31	0.24	0.19	0.19	0.24	0.32	0.39	0.54	0.75	1.08	1.22	1.29	1.31	1.15	0.17
Ag	47	0.22	0.14	0.11	0.08	0.08	0.11	0.16	0.20	0.32	0.49	0.77	0.90	0.96	0.98	0.83	0.07
Cd	48	0.44	0.33	0.27	0.24	0.25	0.33	0.44	0.52	0.72	0.96	1.28	1.41	1.47	1.48	1.29	0.22
In	49	0.31	0.22	0.19	0.17	0.18	0.24	0.33	0.40	0.57	0.80	1.10	1.22	1.28	1.28	1.09	0.14
Sn	50	0.60	0.47	0.40	0.35	0.37	0.46	0.57	0.66	0.89	1.15	1.45	1.56	1.61	1.60	1.35	0.24
Sb	51	0.39	0.28	0.23	0.19	0.20	0.27	0.35	0.42	0.62	0.86	1.13	1.23	1.27	1.25	0.98	0.10
Te	52	0.32	0.23	0.18	0.15	0.16	0.21	0.29	0.35	0.53	0.76	1.02	1.12	1.16	1.13	0.86	0.07
I	53	0.12	0.08	0.05	0.04	0.05	0.07	0.10	0.13	0.23	0.38	0.59	0.67	0.70	0.68	0.45	0.01
Xe	54	0.38	0.27	0.22	0.19	0.19	0.25	0.34	0.40	0.61	0.86	1.11	1.20	1.24	1.20	0.89	0.08
Cs	55	0.28	0.20	0.16	0.13	0.14	0.19	0.26	0.33	0.52	0.76	1.01	1.10	1.13	1.10	0.78	0.06
Ba	56	1.09	0.92	0.82	0.76	0.80	0.93	1.09	1.26	1.63	1.87	2.05	2.10	2.11	2.00	1.42	0.27
La	57	1.09	0.92	0.82	0.77	0.80	0.95	1.11	1.29	1.68	1.90	2.06	2.11	2.10	1.97	1.29	0.21
Ce	58	1.21	1.03	0.93	0.88	0.93	1.08	1.25	1.48	1.88	2.06	2.20	2.23	2.21	2.02	1.24	0.18
Pr	59	1.00	0.83	0.74	0.70	0.74	0.89	1.06	1.29	1.68	1.87	2.01	2.03	2.02	1.83	1.05	0.11
Nd	60	1.09	0.91	0.82	0.77	0.82	0.97	1.15	1.38	1.77	1.96	2.08	2.10	2.09	1.87	1.05	0.11
Sm	62	0.94	0.76	0.67	0.63	0.67	0.81	0.98	1.21	1.59	1.77	1.88	1.90	1.88	1.64	0.82	0.06
Eu	63	0.38	0.28	0.22	0.20	0.22	0.30	0.41	0.58	0.92	1.07	1.18	1.20	1.18	0.95	0.30	0.00
Gd	64	0.69	0.54	0.46	0.43	0.46	0.58	0.73	0.95	1.32	1.49	1.60	1.61	1.59	1.35	0.57	0.02
Tb	65	0.50	0.37	0.31	0.28	0.31	0.41	0.54	0.74	1.09	1.25	1.36	1.37	1.34	1.11	0.39	0.00
Dy	66	0.68	0.53	0.45	0.42	0.45	0.57	0.72	0.94	1.31	1.47	1.57	1.58	1.56	1.31	0.53	0.02
Ho	67	0.48	0.36	0.30	0.27	0.30	0.40	0.52	0.72	1.07	1.22	1.32	1.33	1.31	1.06	0.36	0.00
Er	68	0.77	0.62	0.54	0.50	0.54	0.67	0.82	1.05	1.42	1.58	1.68	1.69	1.66	1.41	0.61	0.03
Tm	69	0.67	0.52	0.45	0.41	0.45	0.56	0.71	0.93	1.29	1.44	1.54	1.54	1.51	1.26	0.49	0.01
Yb	70	1.08	0.90	0.80	0.76	0.80	0.94	1.11	1.35	1.73	1.88	1.98	1.99	1.97	1.71	0.85	0.08
Lu	71	0.83	0.66	0.58	0.53	0.57	0.69	0.84	1.07	1.43	1.59	1.69	1.70	1.68	1.42	0.60	0.03
Hf	72	1.27	1.08	0.97	0.92	0.95	1.10	1.27	1.52	1.91	2.07	2.18	2.18	2.16	1.89	1.00	0.12
Ta	73	1.15	0.96	0.86	0.80	0.84	0.98	1.16	1.41	1.79	1.95	2.06	2.07	2.04	1.76	0.89	0.08
W	74	1.27	1.08	0.97	0.91	0.95	1.10	1.29	1.55	1.94	2.10	2.20	2.21	2.18	1.89	1.00	0.11
Re	75	0.78	0.61	0.52	0.48	0.52	0.64	0.87	1.13	1.43	1.56	1.64	1.62	1.58	1.29	0.51	0.01
Os	76	0.64	0.49	0.41	0.38	0.42	0.53	0.70	0.93	1.29	1.43	1.53	1.53	1.50	1.21	0.44	0.01
Ir	77	0.16	0.10	0.07	0.07	0.07	0.11	0.17	0.29	0.53	0.64	0.73	0.73	0.70	0.47	0.07	0.00
Pt	78	0.46	0.34	0.28	0.26	0.28	0.38	0.51	0.72	1.06	1.20	1.29	1.29	1.26	0.97	0.28	0.00
Au	79	0.44	0.32	0.27	0.25	0.27	0.36	0.49	0.70	1.04	1.17	1.26	1.26	1.23	0.93	0.26	0.00
Hg	80	1.31	1.12	1.03	0.98	1.03	1.19	1.39	1.66	2.04	2.18	2.27	2.27	2.24	1.90	1.00	0.14
Tl	81	1.35	1.16	1.06	1.04	1.10	1.26	1.57	1.86	2.11	2.23	2.29	2.25	2.19	1.81	0.95	0.10
Pb	82	3.27	3.24	3.22	3.21	3.20	3.18	3.16	3.13	3.07	2.99	2.81	2.62	2.40	1.77	0.89	0.03
Bi	83	3.17	3.12	3.09	3.05	3.02	2.98	2.93	2.88	2.77	2.64	2.39	2.11	1.76	1.06	0.28	0.00

Table B2. The same as Table B1, but for $M^{\rm AGB}_{\rm ini} = 1.4\ M_{\odot}$ (n10).

El	Z	ST*2	ST*1.3	ST	ST/1.5	ST/2	ST/3	ST/4.5	ST/6	ST/9	ST/12	ST/18	ST/24	ST/30	ST/45	ST/75	ST/150
He	4	0.16	0.16	0.16	0.16	0.16	0.16	0.16	0.15	0.16	0.16	0.16	0.16	0.16	0.16	0.16	0.15
C	6	3.90	3.90	3.90	3.90	3.90	3.90	3.90	3.90	3.89	3.89	3.89	3.89	3.89	3.89	3.89	3.89
N	7	1.36	1.36	1.36	1.36	1.36	1.35	1.35	1.35	1.35	1.35	1.35	1.35	1.35	1.35	1.35	1.35
O	8	1.95	1.91	1.88	1.84	1.81	1.78	1.75	1.74	1.72	1.71	1.70	1.69	1.68	1.68	1.67	1.66
F	9	4.00	3.94	3.90	3.83	3.79	3.71	3.64	3.59	3.52	3.46	3.39	3.33	3.29	3.21	3.12	2.99
Ne	10	2.36	2.35	2.35	2.34	2.34	2.34	2.33	2.33	2.33	2.33	2.33	2.33	2.33	2.33	2.33	2.32
Na	11	2.03	2.01	1.99	1.98	1.98	1.97	1.96	1.96	1.96	1.95	1.95	1.94	1.94	1.93	1.92	1.91
Mg	12	1.45	1.41	1.37	1.32	1.29	1.24	1.20	1.17	1.14	1.12	1.11	1.10	1.09	1.08	1.07	1.07
Al	13	0.51	0.44	0.38	0.31	0.27	0.22	0.18	0.17	0.15	0.14	0.13	0.13	0.13	0.12	0.12	0.12
Si	14	0.51	0.45	0.42	0.38	0.36	0.34	0.33	0.32	0.32	0.32	0.31	0.31	0.31	0.31	0.31	0.31
P	15	1.70	1.47	1.29	1.05	0.90	0.72	0.60	0.55	0.50	0.47	0.43	0.41	0.39	0.35	0.31	0.26
S	16	0.43	0.38	0.35	0.32	0.32	0.31	0.30	0.30	0.30	0.30	0.30	0.30	0.30	0.30	0.30	0.30
Cl	17	0.25	0.19	0.16	0.14	0.14	0.13	0.13	0.13	0.14	0.14	0.15	0.16	0.16	0.16	0.16	0.14
Ar	18	0.27	0.27	0.26	0.26	0.26	0.26	0.26	0.26	0.26	0.26	0.26	0.26	0.26	0.26	0.26	0.26
K	19	0.41	0.40	0.39	0.39	0.38	0.38	0.38	0.38	0.38	0.38	0.38	0.38	0.38	0.38	0.38	0.37
Ca	20	0.29	0.28	0.28	0.28	0.28	0.28	0.28	0.28	0.28	0.28	0.28	0.28	0.28	0.28	0.28	0.28
Sc	21	0.81	0.73	0.69	0.65	0.63	0.62	0.62	0.62	0.63	0.64	0.65	0.65	0.65	0.64	0.61	0.56
Ti	22	0.42	0.36	0.33	0.32	0.32	0.32	0.33	0.34	0.34	0.34	0.34	0.34	0.33	0.32	0.30	0.28
V	23	0.12	0.06	0.04	0.03	0.03	0.03	0.04	0.05	0.05	0.05	0.04	0.03	0.03	0.01	0.00	0.00
Cr	24	-0.20	-0.20	-0.20	-0.20	-0.20	-0.20	-0.20	-0.20	-0.20	-0.20	-0.20	-0.20	-0.20	-0.20	-0.20	-0.20
Mn	25	-0.40	-0.40	-0.40	-0.40	-0.40	-0.40	-0.40	-0.40	-0.40	-0.40	-0.40	-0.40	-0.40	-0.40	-0.40	-0.40
Fe	26	0.00	0.00	0.00	0.00	0.00	0.00	0.00	0.00	0.00	0.00	0.00	0.00	0.00	0.00	0.00	0.00
Co	27	0.79	0.79	0.78	0.78	0.77	0.77	0.76	0.76	0.75	0.75	0.74	0.74	0.73	0.73	0.73	0.73
Ni	28	0.23	0.21	0.21	0.19	0.19	0.18	0.17	0.16	0.16	0.15	0.15	0.15	0.15	0.15	0.15	0.15
Cu	29	1.24	1.22	1.20	1.17	1.16	1.13	1.10	1.08	1.06	1.05	1.04	1.03	1.04	1.05	1.06	1.06
Zn	30	0.68	0.65	0.62	0.58	0.56	0.52	0.48	0.46	0.44	0.44	0.45	0.47	0.49	0.52	0.54	0.50
Ga	31	1.25	1.19	1.15	1.09	1.05	0.99	0.94	0.91	0.89	0.89	0.93	0.98	1.01	1.07	1.08	0.99
Ge	32	1.26	1.19	1.14	1.07	1.03	0.96	0.91	0.88	0.87	0.89	0.96	1.02	1.07	1.13	1.12	0.98
As	33	1.10	1.03	0.97	0.90	0.85	0.78	0.73	0.70	0.70	0.74	0.84	0.91	0.96	1.02	0.99	0.82
Se	34	1.24	1.15	1.09	1.01	0.95	0.88	0.82	0.80	0.83	0.90	1.04	1.12	1.17	1.22	1.16	0.93
Br	35	1.14	1.05	0.99	0.90	0.85	0.77	0.72	0.70	0.74	0.83	0.96	1.05	1.10	1.14	1.08	0.83
Kr	36	1.39	1.26	1.18	1.07	1.01	0.94	0.91	0.94	1.07	1.20	1.35	1.43	1.47	1.47	1.34	0.96
Rb	37	1.64	1.51	1.41	1.29	1.23	1.16	1.14	1.18	1.35	1.50	1.65	1.73	1.77	1.75	1.60	1.15
Sr	38	1.41	1.25	1.15	1.06	1.02	1.04	1.20	1.39	1.63	1.75	1.87	1.91	1.91	1.84	1.65	0.98
Y	39	1.44	1.25	1.14	1.06	1.05	1.13	1.36	1.58	1.83	1.95	2.05	2.07	2.05	1.96	1.73	0.91
Zr	40	1.40	1.18	1.07	1.02	1.04	1.18	1.49	1.71	1.93	2.03	2.11	2.10	2.06	1.93	1.67	0.73
Nb	41	1.42	1.20	1.09	1.04	1.06	1.21	1.52	1.75	1.97	2.07	2.15	2.14	2.10	1.97	1.70	0.73
Mo	42	1.26	1.03	0.93	0.89	0.93	1.11	1.44	1.66	1.85	1.95	2.01	1.98	1.93	1.78	1.50	0.50
Ru	44	1.01	0.79	0.69	0.66	0.69	0.86	1.18	1.39	1.58	1.68	1.72	1.69	1.64	1.49	1.22	0.29
Rh	45	0.67	0.48	0.40	0.37	0.39	0.54	0.83	1.02	1.20	1.29	1.34	1.31	1.27	1.13	0.88	0.12
Pd	46	1.03	0.80	0.70	0.67	0.70	0.88	1.21	1.42	1.60	1.71	1.77	1.75	1.71	1.58	1.32	0.33
Ag	47	0.68	0.48	0.40	0.38	0.41	0.56	0.85	1.04	1.23	1.33	1.39	1.38	1.35	1.23	0.98	0.14
Cd	48	1.08	0.87	0.78	0.76	0.81	1.01	1.35	1.56	1.75	1.85	1.91	1.90	1.87	1.74	1.46	0.40
In	49	0.89	0.69	0.62	0.61	0.66	0.85	1.18	1.38	1.57	1.67	1.73	1.71	1.68	1.54	1.25	0.27
Sn	50	1.30	1.07	0.98	0.98	1.03	1.28	1.64	1.83	1.99	2.08	2.10	2.06	2.01	1.85	1.52	0.42
Sb	51	1.00	0.79	0.70	0.70	0.75	1.00	1.35	1.53	1.68	1.76	1.76	1.71	1.66	1.49	1.15	0.19
Te	52	0.88	0.67	0.59	0.59	0.64	0.88	1.24	1.40	1.55	1.63	1.63	1.58	1.52	1.36	1.02	0.14
I	53	0.47	0.31	0.26	0.26	0.29	0.48	0.78	0.93	1.07	1.14	1.13	1.09	1.03	0.87	0.57	0.00
Xe	54	0.97	0.76	0.68	0.68	0.73	1.00	1.35	1.51	1.66	1.73	1.71	1.66	1.60	1.42	1.06	0.15
Cs	55	0.80	0.60	0.53	0.53	0.58	0.83	1.18	1.33	1.49	1.56	1.55	1.51	1.45	1.29	0.93	0.09
Ba	56	1.82	1.59	1.51	1.54	1.66	2.04	2.32	2.44	2.57	2.59	2.54	2.47	2.39	2.18	1.63	0.44
La	57	1.83	1.60	1.52	1.55	1.69	2.09	2.34	2.45	2.58	2.58	2.52	2.44	2.36	2.14	1.52	0.34
Ce	58	1.95	1.73	1.65	1.70	1.88	2.28	2.49	2.60	2.70	2.68	2.61	2.52	2.43	2.18	1.48	0.30
Pr	59	1.72	1.51	1.44	1.49	1.66	2.06	2.27	2.38	2.48	2.47	2.40	2.31	2.23	1.98	1.28	0.19
Nd	60	1.81	1.59	1.52	1.58	1.76	2.16	2.36	2.47	2.56	2.54	2.46	2.37	2.29	2.03	1.29	0.19
Sm	62	1.66	1.44	1.37	1.42	1.61	2.01	2.20	2.30	2.38	2.36	2.28	2.17	2.09	1.81	1.07	0.10
Eu	63	0.98	0.78	0.71	0.76	0.93	1.30	1.49	1.59	1.67	1.65	1.56	1.46	1.38	1.11	0.46	0.00
Gd	64	1.38	1.17	1.10	1.16	1.34	1.73	1.92	2.03	2.10	2.08	1.99	1.89	1.80	1.52	0.80	0.03
Tb	65	1.15	0.94	0.87	0.93	1.10	1.49	1.67	1.78	1.86	1.83	1.74	1.64	1.55	1.27	0.59	0.00
Dy	66	1.37	1.16	1.09	1.15	1.33	1.72	1.91	2.01	2.09	2.06	1.97	1.86	1.77	1.48	0.77	0.02
Ho	67	1.13	0.93	0.86	0.92	1.10	1.48	1.66	1.77	1.84	1.81	1.72	1.61	1.52	1.24	0.56	0.00
Er	68	1.50	1.28	1.21	1.27	1.46	1.86	2.04	2.14	2.21	2.18	2.09	1.98	1.88	1.59	0.86	0.05
Tm	69	1.36	1.15	1.08	1.14	1.32	1.72	1.89	2.00	2.07	2.04	1.94	1.83	1.73	1.44	0.73	0.02
Yb	70	1.83	1.61	1.54	1.60	1.79	2.19	2.37	2.47	2.54	2.50	2.40	2.29	2.19	1.90	1.13	0.14
Lu	71	1.55	1.33	1.26	1.32	1.51	1.90	2.08	2.18	2.24	2.20	2.10	1.99	1.90	1.60	0.86	0.05
Hf	72	2.02	1.79	1.71	1.77	1.97	2.37	2.54	2.65	2.71	2.67	2.57	2.46	2.37	2.07	1.28	0.21
Ta	73	1.89	1.67	1.59	1.65	1.85	2.24	2.41	2.52	2.58	2.54	2.44	2.34	2.25	1.94	1.16	0.16
W	74	2.01	1.79	1.71	1.77	1.97	2.37	2.54	2.65	2.70	2.67	2.58	2.47	2.38	2.07	1.28	0.22
Re	75	1.44	1.22	1.15	1.25	1.48	1.83	1.98	2.08	2.11	2.06	1.96	1.84	1.75	1.44	0.71	0.02
Os	76	1.32	1.10	1.03	1.10	1.31	1.68	1.85	1.96	2.01	1.98	1.88	1.77	1.69	1.38	0.64	0.01
Ir	77	0.55	0.39	0.35	0.39	0.54	0.86	1.00	1.11	1.16	1.13	1.04	0.94	0.86	0.59	0.12	0.00
Pt	78	1.08	0.88	0.82	0.88	1.08	1.45	1.61	1.72	1.77	1.74	1.64	1.54	1.45	1.13	0.44	0.00
Au	79	1.05	0.85	0.79	0.86	1.05	1.42	1.58	1.69	1.74	1.70	1.61	1.50	1.41	1.09	0.41	0.00
Hg	80	2.04	1.83	1.76	1.83	2.05	2.44	2.59	2.71	2.75	2.71	2.62	2.51	2.42	2.07	1.26	0.25
Tl	81	2.05	1.84	1.79	1.94	2.20	2.51	2.64	2.74	2.72	2.67	2.55	2.43	2.34	1.96	1.17	0.23
Pb	82	3.86	3.80	3.78	3.75	3.74	3.69	3.62	3.54	3.40	3.26	3.02	2.81	2.58	2.01	1.12	0.12
Bi	83	3.75	3.69	3.65	3.61	3.58	3.51	3.41	3.31	3.13	2.96	2.67	2.39	2.09	1.45	0.56	0.03

Table B3. The same as Table B1, but for $M_{\rm ini}^{\rm AGB} = 1.5\ M_{\odot}$ (n20).

El	Z	ST*2	ST*1.3	ST	ST/1.5	ST/2	ST/3	ST/4.5	ST/6	ST/9	ST/12	ST/18	ST/24	ST/30	ST/45	ST/75	ST/150
He	4	0.26	0.26	0.26	0.26	0.26	0.26	0.26	0.26	0.26	0.26	0.26	0.26	0.26	0.26	0.26	0.26
C	6	4.13	4.13	4.13	4.13	4.13	4.13	4.13	4.13	4.13	4.13	4.13	4.13	4.13	4.13	4.13	4.12
N	7	2.17	2.16	2.16	2.16	2.16	2.16	2.16	2.16	2.16	2.16	2.16	2.16	2.16	2.15	2.15	2.15
O	8	2.18	2.12	2.09	2.04	2.02	1.98	1.96	1.94	1.93	1.92	1.90	1.90	1.89	1.89	1.88	1.88
F	9	4.15	4.07	4.02	3.94	3.89	3.82	3.75	3.71	3.64	3.60	3.54	3.51	3.48	3.43	3.38	3.31
Ne	10	2.88	2.88	2.87	2.87	2.87	2.87	2.87	2.87	2.87	2.87	2.87	2.87	2.87	2.86	2.86	2.86
Na	11	2.57	2.57	2.57	2.57	2.57	2.58	2.58	2.58	2.58	2.58	2.58	2.57	2.57	2.56	2.56	2.55
Mg	12	2.07	2.02	1.98	1.93	1.90	1.85	1.81	1.79	1.77	1.76	1.74	1.74	1.73	1.73	1.72	1.72
Al	13	0.98	0.88	0.81	0.72	0.67	0.62	0.58	0.56	0.54	0.53	0.51	0.51	0.50	0.49	0.48	0.48
Si	14	0.77	0.66	0.59	0.50	0.46	0.42	0.39	0.38	0.37	0.36	0.36	0.36	0.35	0.35	0.35	0.35
P	15	2.12	1.87	1.66	1.39	1.22	1.00	0.86	0.79	0.73	0.69	0.65	0.63	0.61	0.58	0.54	0.50
S	16	0.59	0.47	0.41	0.36	0.34	0.32	0.32	0.32	0.31	0.31	0.31	0.31	0.31	0.31	0.31	0.31
Cl	17	0.40	0.30	0.26	0.23	0.22	0.22	0.23	0.24	0.25	0.26	0.26	0.27	0.27	0.27	0.26	0.23
Ar	18	0.27	0.26	0.26	0.26	0.26	0.26	0.26	0.26	0.26	0.26	0.26	0.26	0.26	0.26	0.26	0.26
K	19	0.49	0.47	0.46	0.45	0.45	0.45	0.45	0.46	0.46	0.46	0.46	0.46	0.46	0.46	0.46	0.46
Ca	20	0.28	0.28	0.28	0.27	0.27	0.27	0.28	0.28	0.28	0.28	0.28	0.28	0.28	0.28	0.27	0.27
Sc	21	1.04	0.94	0.89	0.88	0.88	0.89	0.91	0.92	0.93	0.93	0.93	0.93	0.92	0.91	0.88	0.85
Ti	22	0.54	0.44	0.41	0.41	0.41	0.43	0.43	0.43	0.43	0.42	0.41	0.40	0.38	0.37	0.35	0.33
V	23	0.21	0.12	0.09	0.09	0.09	0.10	0.10	0.10	0.09	0.08	0.06	0.05	0.04	0.02	0.01	0.00
Cr	24	-0.20	-0.20	-0.20	-0.20	-0.20	-0.20	-0.20	-0.20	-0.20	-0.20	-0.20	-0.20	-0.20	-0.20	-0.20	-0.20
Mn	25	-0.40	-0.40	-0.40	-0.40	-0.40	-0.40	-0.40	-0.40	-0.40	-0.40	-0.40	-0.40	-0.40	-0.40	-0.40	-0.40
Fe	26	0.00	0.00	0.00	0.00	0.00	0.00	0.00	0.00	0.00	0.00	0.00	0.00	0.00	0.00	0.00	0.00
Co	27	1.01	1.01	1.01	1.01	1.01	1.00	1.00	1.00	1.00	1.00	1.00	1.00	1.00	1.00	1.00	1.00
Ni	28	0.33	0.31	0.31	0.30	0.30	0.30	0.29	0.29	0.29	0.29	0.29	0.30	0.30	0.30	0.31	0.31
Cu	29	1.44	1.42	1.41	1.40	1.39	1.38	1.38	1.37	1.37	1.38	1.39	1.39	1.40	1.42	1.43	1.43
Zn	30	0.82	0.80	0.78	0.76	0.74	0.73	0.72	0.73	0.75	0.77	0.81	0.83	0.85	0.86	0.86	0.82
Ga	31	1.40	1.36	1.33	1.30	1.28	1.27	1.26	1.28	1.32	1.36	1.42	1.46	1.47	1.48	1.46	1.40
Ge	32	1.41	1.35	1.32	1.29	1.27	1.25	1.25	1.28	1.36	1.41	1.48	1.52	1.53	1.53	1.49	1.40
As	33	1.24	1.18	1.14	1.10	1.08	1.06	1.08	1.13	1.22	1.29	1.36	1.40	1.41	1.40	1.34	1.23
Se	34	1.38	1.31	1.27	1.22	1.20	1.18	1.23	1.30	1.43	1.50	1.58	1.61	1.61	1.58	1.50	1.36
Br	35	1.28	1.21	1.16	1.11	1.09	1.08	1.13	1.21	1.35	1.43	1.51	1.53	1.53	1.49	1.41	1.26
Kr	36	1.53	1.43	1.37	1.33	1.32	1.36	1.49	1.62	1.76	1.84	1.90	1.89	1.86	1.79	1.66	1.45
Rb	37	1.80	1.69	1.63	1.58	1.57	1.62	1.79	1.93	2.08	2.16	2.21	2.19	2.16	2.07	1.92	1.69
Sr	38	1.62	1.48	1.42	1.41	1.48	1.74	1.99	2.11	2.22	2.25	2.21	2.16	2.11	2.00	1.81	1.40
Y	39	1.69	1.52	1.46	1.49	1.61	1.93	2.19	2.30	2.40	2.41	2.35	2.28	2.21	2.08	1.85	1.32
Zr	40	1.69	1.50	1.45	1.53	1.70	2.07	2.30	2.40	2.47	2.45	2.35	2.27	2.19	2.02	1.76	1.11
Nb	41	1.71	1.53	1.47	1.55	1.73	2.11	2.34	2.43	2.51	2.49	2.39	2.30	2.22	2.05	1.78	1.10
Mo	42	1.57	1.38	1.33	1.44	1.64	2.02	2.22	2.31	2.37	2.33	2.21	2.12	2.04	1.85	1.55	0.81
Ru	44	1.30	1.11	1.07	1.18	1.39	1.77	1.96	2.06	2.11	2.06	1.93	1.83	1.75	1.56	1.27	0.55
Rh	45	0.93	0.75	0.71	0.82	1.02	1.39	1.58	1.67	1.72	1.67	1.54	1.45	1.37	1.19	0.92	0.27
Pd	46	1.31	1.12	1.08	1.20	1.42	1.79	1.98	2.07	2.12	2.07	1.96	1.87	1.80	1.63	1.35	0.56
Ag	47	0.94	0.76	0.72	0.83	1.04	1.40	1.59	1.68	1.73	1.68	1.57	1.49	1.42	1.26	1.00	0.28
Cd	48	1.41	1.22	1.18	1.31	1.53	1.90	2.07	2.16	2.20	2.16	2.06	1.99	1.93	1.76	1.47	0.59
In	49	1.22	1.04	1.01	1.14	1.35	1.71	1.88	1.97	2.01	1.96	1.87	1.79	1.73	1.56	1.27	0.42
Sn	50	1.63	1.45	1.42	1.58	1.83	2.18	2.33	2.42	2.43	2.36	2.24	2.14	2.06	1.87	1.54	0.62
Sb	51	1.32	1.14	1.11	1.29	1.54	1.89	2.02	2.11	2.10	2.02	1.89	1.79	1.71	1.51	1.17	0.32
Te	52	1.19	1.01	0.99	1.17	1.42	1.76	1.89	1.97	1.96	1.88	1.75	1.65	1.57	1.37	1.03	0.22
I	53	0.73	0.57	0.55	0.71	0.95	1.27	1.39	1.47	1.45	1.37	1.24	1.15	1.07	0.88	0.57	0.01
Xe	54	1.29	1.11	1.09	1.29	1.56	1.87	2.00	2.08	2.04	1.95	1.82	1.72	1.63	1.43	1.06	0.23
Cs	55	1.10	0.93	0.91	1.11	1.37	1.69	1.81	1.89	1.85	1.77	1.65	1.56	1.48	1.29	0.92	0.14
Ba	56	2.17	2.00	2.03	2.37	2.59	2.78	2.90	2.92	2.82	2.73	2.60	2.49	2.39	2.17	1.63	0.56
La	57	2.17	2.01	2.06	2.42	2.63	2.79	2.90	2.90	2.79	2.69	2.56	2.45	2.35	2.12	1.52	0.43
Ce	58	2.30	2.15	2.23	2.62	2.80	2.92	3.03	2.99	2.86	2.77	2.64	2.52	2.42	2.16	1.47	0.37
Pr	59	2.08	1.92	2.01	2.40	2.57	2.70	2.80	2.77	2.64	2.55	2.42	2.31	2.21	1.96	1.27	0.23
Nd	60	2.16	2.01	2.11	2.50	2.67	2.78	2.88	2.84	2.71	2.62	2.49	2.37	2.27	2.00	1.28	0.23
Sm	62	2.01	1.86	1.96	2.35	2.51	2.63	2.72	2.67	2.54	2.44	2.30	2.17	2.07	1.79	1.06	0.13
Eu	63	1.30	1.16	1.26	1.64	1.80	1.91	2.01	1.95	1.82	1.72	1.58	1.46	1.36	1.08	0.45	0.00
Gd	64	1.73	1.58	1.68	2.07	2.23	2.35	2.44	2.39	2.25	2.16	2.01	1.89	1.78	1.49	0.79	0.03
Tb	65	1.49	1.34	1.44	1.83	1.98	2.10	2.19	2.14	2.00	1.91	1.76	1.64	1.53	1.25	0.57	0.00
Dy	66	1.72	1.57	1.68	2.07	2.22	2.34	2.43	2.37	2.23	2.14	1.99	1.86	1.76	1.46	0.76	0.02
Ho	67	1.48	1.33	1.44	1.82	1.98	2.09	2.18	2.12	1.98	1.89	1.74	1.61	1.51	1.21	0.55	0.00
Er	68	1.85	1.70	1.81	2.20	2.35	2.46	2.56	2.49	2.36	2.26	2.11	1.97	1.87	1.57	0.85	0.05
Tm	69	1.71	1.56	1.67	2.06	2.21	2.32	2.41	2.35	2.21	2.11	1.96	1.83	1.72	1.42	0.72	0.01
Yb	70	2.18	2.04	2.15	2.54	2.69	2.80	2.89	2.82	2.68	2.58	2.42	2.28	2.18	1.87	1.13	0.18
Lu	71	1.90	1.75	1.87	2.26	2.41	2.52	2.60	2.53	2.39	2.28	2.12	1.99	1.88	1.58	0.85	0.06
Hf	72	2.36	2.22	2.33	2.73	2.87	2.99	3.07	3.00	2.85	2.75	2.59	2.46	2.36	2.05	1.28	0.27
Ta	73	2.24	2.09	2.21	2.60	2.75	2.86	2.94	2.87	2.72	2.62	2.46	2.33	2.23	1.92	1.16	0.20
W	74	2.36	2.21	2.33	2.73	2.87	2.98	3.06	2.99	2.84	2.75	2.60	2.47	2.36	2.05	1.27	0.28
Re	75	1.77	1.63	1.77	2.17	2.29	2.40	2.47	2.39	2.24	2.13	1.97	1.84	1.73	1.41	0.70	0.03
Os	76	1.66	1.52	1.64	2.04	2.17	2.28	2.35	2.28	2.14	2.04	1.90	1.77	1.67	1.35	0.63	0.00
Ir	77	0.83	0.71	0.82	1.18	1.30	1.41	1.49	1.41	1.28	1.19	1.05	0.93	0.84	0.56	0.09	0.00
Pt	78	1.42	1.28	1.41	1.80	1.93	2.04	2.11	2.03	1.89	1.80	1.65	1.53	1.43	1.11	0.43	0.00
Au	79	1.39	1.25	1.38	1.77	1.89	2.00	2.07	1.99	1.86	1.76	1.62	1.49	1.39	1.07	0.40	0.00
Hg	80	2.39	2.26	2.40	2.80	2.91	3.02	3.09	3.00	2.87	2.77	2.63	2.50	2.40	2.05	1.26	0.32
Tl	81	2.40	2.28	2.46	2.85	2.93	3.04	3.07	2.97	2.82	2.72	2.55	2.41	2.31	1.93	1.16	0.32
Pb	82	4.16	4.10	4.07	4.02	3.98	3.88	3.72	3.60	3.41	3.26	3.00	2.78	2.56	1.98	1.12	0.21
Bi	83	4.03	3.97	3.93	3.86	3.80	3.67	3.49	3.35	3.14	2.96	2.65	2.37	2.08	1.45	0.58	0.08

Table B4. The same as Table B1, but for $M^{\rm AGB}_{\rm ini} = 2.0\ M_{\odot}$ (n26).

El	Z	ST*2	ST*1.3	ST	ST/1.5	ST/2	ST/3	ST/4.5	ST/6	ST/9	ST/12	ST/18	ST/24	ST/30	ST/45	ST/75	ST/150
He	4	0.25	0.25	0.24	0.24	0.24	0.24	0.24	0.24	0.25	0.25	0.24	0.24	0.24	0.24	0.24	0.24
C	6	4.07	4.07	4.07	4.06	4.06	4.06	4.06	4.06	4.06	4.06	4.06	4.06	4.06	4.06	4.05	4.05
N	7	1.93	1.93	1.93	1.92	1.92	1.92	1.92	1.92	1.92	1.92	1.91	1.91	1.91	1.91	1.91	1.91
O	8	2.18	2.13	2.09	2.04	2.01	1.96	1.93	1.91	1.88	1.87	1.85	1.85	1.84	1.83	1.82	1.81
F	9	4.27	4.22	4.18	4.11	4.07	4.01	3.94	3.89	3.82	3.76	3.68	3.62	3.58	3.49	3.38	3.17
Ne	10	2.46	2.45	2.44	2.43	2.42	2.42	2.41	2.41	2.41	2.41	2.41	2.41	2.40	2.40	2.40	2.40
Na	11	2.22	2.20	2.19	2.19	2.18	2.18	2.18	2.18	2.18	2.18	2.18	2.17	2.17	2.16	2.15	2.14
Mg	12	1.80	1.75	1.72	1.67	1.64	1.59	1.55	1.52	1.49	1.47	1.45	1.44	1.43	1.42	1.41	1.41
Al	13	0.85	0.77	0.71	0.62	0.57	0.51	0.46	0.44	0.41	0.40	0.38	0.38	0.37	0.36	0.35	0.34
Si	14	0.74	0.65	0.59	0.51	0.47	0.42	0.39	0.38	0.36	0.35	0.35	0.35	0.34	0.34	0.34	0.34
P	15	2.17	1.96	1.79	1.54	1.38	1.15	0.97	0.87	0.78	0.74	0.68	0.65	0.63	0.58	0.53	0.47
S	16	0.63	0.52	0.46	0.39	0.36	0.34	0.32	0.32	0.31	0.31	0.31	0.31	0.31	0.31	0.31	0.31
Cl	17	0.49	0.37	0.30	0.24	0.21	0.20	0.19	0.19	0.20	0.21	0.22	0.23	0.24	0.25	0.25	0.22
Ar	18	0.28	0.27	0.27	0.26	0.26	0.26	0.26	0.26	0.26	0.26	0.26	0.26	0.26	0.26	0.26	0.26
K	19	0.50	0.47	0.46	0.44	0.44	0.43	0.43	0.43	0.43	0.43	0.44	0.44	0.44	0.44	0.44	0.43
Ca	20	0.29	0.28	0.28	0.28	0.28	0.28	0.28	0.28	0.28	0.28	0.28	0.28	0.28	0.28	0.28	0.28
Sc	21	1.19	1.04	0.96	0.89	0.86	0.85	0.85	0.86	0.88	0.89	0.91	0.91	0.91	0.90	0.87	0.82
Ti	22	0.66	0.52	0.45	0.39	0.38	0.39	0.40	0.41	0.43	0.43	0.43	0.42	0.41	0.38	0.35	0.32
V	23	0.34	0.20	0.13	0.08	0.07	0.08	0.09	0.10	0.11	0.11	0.10	0.09	0.07	0.04	0.02	0.00
Cr	24	-0.20	-0.20	-0.20	-0.20	-0.20	-0.20	-0.20	-0.20	-0.20	-0.20	-0.20	-0.20	-0.20	-0.20	-0.20	-0.20
Mn	25	-0.40	-0.40	-0.40	-0.40	-0.40	-0.40	-0.40	-0.40	-0.40	-0.40	-0.40	-0.40	-0.40	-0.40	-0.40	-0.40
Fe	26	0.00	0.00	0.00	0.00	0.00	0.00	0.00	0.00	0.00	0.00	0.00	0.00	0.00	0.00	0.00	0.00
Co	27	0.99	0.99	0.98	0.98	0.97	0.96	0.95	0.95	0.94	0.93	0.92	0.92	0.92	0.91	0.91	0.92
Ni	28	0.34	0.32	0.31	0.30	0.29	0.28	0.27	0.26	0.26	0.25	0.25	0.25	0.25	0.26	0.26	0.27
Cu	29	1.44	1.41	1.39	1.37	1.35	1.33	1.30	1.29	1.27	1.26	1.26	1.26	1.27	1.29	1.32	1.33
Zn	30	0.84	0.80	0.77	0.73	0.71	0.68	0.65	0.64	0.63	0.63	0.65	0.68	0.71	0.77	0.80	0.77
Ga	31	1.43	1.37	1.33	1.28	1.25	1.21	1.17	1.16	1.15	1.17	1.22	1.27	1.32	1.40	1.42	1.36
Ge	32	1.46	1.39	1.34	1.28	1.25	1.20	1.17	1.16	1.17	1.20	1.28	1.35	1.41	1.49	1.50	1.39
As	33	1.30	1.22	1.17	1.10	1.07	1.02	0.99	0.99	1.01	1.06	1.16	1.25	1.31	1.39	1.38	1.24
Se	34	1.45	1.36	1.30	1.22	1.18	1.14	1.11	1.11	1.16	1.24	1.38	1.47	1.54	1.61	1.57	1.37
Br	35	1.35	1.26	1.19	1.12	1.08	1.03	1.01	1.01	1.07	1.15	1.30	1.40	1.46	1.53	1.48	1.27
Kr	36	1.66	1.52	1.43	1.34	1.30	1.26	1.27	1.32	1.48	1.61	1.77	1.86	1.90	1.90	1.80	1.50
Rb	37	1.96	1.80	1.70	1.60	1.56	1.53	1.55	1.62	1.81	1.95	2.11	2.20	2.23	2.21	2.08	1.77
Sr	38	1.79	1.59	1.46	1.35	1.33	1.36	1.52	1.70	1.94	2.07	2.21	2.27	2.28	2.21	2.06	1.47
Y	39	1.89	1.66	1.51	1.40	1.38	1.46	1.69	1.90	2.14	2.27	2.40	2.43	2.42	2.32	2.11	1.43
Zr	40	1.96	1.69	1.53	1.41	1.41	1.56	1.87	2.09	2.30	2.41	2.50	2.49	2.45	2.31	2.01	1.27
Nb	41	1.96	1.69	1.53	1.41	1.41	1.56	1.87	2.09	2.32	2.43	2.52	2.51	2.47	2.33	2.02	1.25
Mo	42	1.84	1.56	1.39	1.28	1.28	1.47	1.81	2.02	2.22	2.32	2.39	2.36	2.30	2.15	1.77	0.96
Ru	44	1.57	1.29	1.12	1.00	1.01	1.20	1.55	1.75	1.94	2.04	2.10	2.06	2.00	1.85	1.48	0.68
Rh	45	1.20	0.93	0.77	0.66	0.67	0.85	1.18	1.38	1.56	1.66	1.72	1.69	1.63	1.49	1.12	0.39
Pd	46	1.61	1.32	1.15	1.03	1.05	1.25	1.60	1.81	1.99	2.10	2.16	2.14	2.08	1.96	1.57	0.72
Ag	47	1.23	0.95	0.79	0.69	0.70	0.89	1.23	1.42	1.61	1.71	1.78	1.76	1.70	1.59	1.20	0.42
Cd	48	1.65	1.37	1.20	1.10	1.12	1.33	1.67	1.87	2.07	2.19	2.26	2.25	2.20	2.09	1.66	0.76
In	49	1.40	1.14	0.98	0.89	0.91	1.10	1.44	1.64	1.84	1.96	2.04	2.03	1.98	1.88	1.44	0.55
Sn	50	1.87	1.59	1.42	1.32	1.34	1.58	1.94	2.12	2.30	2.40	2.45	2.41	2.34	2.20	1.70	0.76
Sb	51	1.59	1.31	1.15	1.05	1.07	1.32	1.69	1.86	2.03	2.12	2.14	2.08	2.01	1.85	1.32	0.46
Te	52	1.45	1.17	1.01	0.91	0.94	1.20	1.56	1.72	1.89	1.98	2.00	1.93	1.86	1.71	1.16	0.34
I	53	0.97	0.71	0.57	0.49	0.52	0.74	1.07	1.23	1.39	1.48	1.49	1.43	1.35	1.20	0.69	0.08
Xe	54	1.57	1.28	1.12	1.02	1.06	1.35	1.71	1.86	2.02	2.09	2.09	2.01	1.94	1.77	1.18	0.34
Cs	55	1.36	1.08	0.92	0.83	0.87	1.14	1.50	1.65	1.81	1.90	1.91	1.85	1.78	1.63	1.03	0.23
Ba	56	2.43	2.14	1.98	1.91	2.01	2.37	2.65	2.77	2.91	2.94	2.88	2.80	2.72	2.45	1.75	0.65
La	57	2.42	2.14	1.98	1.92	2.03	2.41	2.66	2.77	2.91	2.93	2.85	2.77	2.69	2.37	1.65	0.48
Ce	58	2.55	2.27	2.11	2.07	2.22	2.60	2.81	2.92	3.04	3.04	2.94	2.85	2.77	2.37	1.65	0.40
Pr	59	2.31	2.04	1.88	1.84	1.99	2.37	2.58	2.69	2.81	2.82	2.73	2.65	2.57	2.17	1.45	0.26
Nd	60	2.40	2.12	1.97	1.93	2.08	2.46	2.66	2.78	2.89	2.89	2.79	2.71	2.62	2.19	1.48	0.26
Sm	62	2.28	1.99	1.84	1.80	1.96	2.35	2.54	2.65	2.75	2.73	2.61	2.52	2.42	1.96	1.26	0.15
Eu	63	1.57	1.29	1.14	1.11	1.27	1.64	1.83	1.94	2.03	2.01	1.89	1.80	1.70	1.25	0.61	0.00
Gd	64	2.01	1.73	1.57	1.54	1.71	2.09	2.27	2.38	2.47	2.45	2.33	2.23	2.13	1.66	0.98	0.05
Tb	65	1.76	1.48	1.33	1.30	1.46	1.84	2.03	2.13	2.23	2.20	2.08	1.98	1.87	1.41	0.75	0.00
Dy	66	2.00	1.72	1.56	1.53	1.70	2.08	2.26	2.37	2.46	2.43	2.30	2.21	2.10	1.62	0.94	0.04
Ho	67	1.75	1.47	1.32	1.29	1.46	1.83	2.02	2.12	2.21	2.18	2.05	1.96	1.84	1.37	0.72	0.00
Er	68	2.12	1.84	1.68	1.65	1.82	2.20	2.38	2.49	2.58	2.55	2.42	2.32	2.20	1.73	1.04	0.07
Tm	69	1.96	1.68	1.52	1.49	1.66	2.04	2.22	2.33	2.42	2.39	2.26	2.16	2.04	1.57	0.89	0.03
Yb	70	2.45	2.17	2.01	1.98	2.15	2.54	2.71	2.82	2.90	2.87	2.73	2.63	2.52	2.03	1.33	0.20
Lu	71	2.15	1.87	1.72	1.69	1.86	2.24	2.42	2.52	2.60	2.57	2.43	2.33	2.22	1.73	1.05	0.08
Hf	72	2.64	2.35	2.19	2.17	2.34	2.72	2.90	3.00	3.08	3.04	2.90	2.81	2.70	2.19	1.49	0.29
Ta	73	2.52	2.23	2.07	2.05	2.23	2.61	2.78	2.88	2.96	2.92	2.78	2.69	2.57	2.07	1.37	0.22
W	74	2.66	2.37	2.21	2.19	2.38	2.76	2.92	3.02	3.10	3.06	2.92	2.83	2.71	2.20	1.50	0.28
Re	75	2.08	1.79	1.63	1.63	1.83	2.19	2.34	2.45	2.51	2.46	2.31	2.22	2.10	1.59	0.93	0.04
Os	76	1.95	1.66	1.50	1.49	1.68	2.05	2.21	2.32	2.39	2.35	2.21	2.13	2.01	1.49	0.83	0.01
Ir	77	1.08	0.82	0.69	0.67	0.84	1.18	1.33	1.44	1.51	1.48	1.34	1.27	1.15	0.67	0.20	0.00
Pt	78	1.67	1.39	1.24	1.23	1.42	1.78	1.94	2.05	2.13	2.09	1.96	1.88	1.75	1.23	0.60	0.00
Au	79	1.63	1.35	1.21	1.19	1.38	1.74	1.90	2.01	2.08	2.05	1.92	1.84	1.71	1.18	0.57	0.00
Hg	80	2.64	2.36	2.21	2.20	2.39	2.75	2.91	3.03	3.10	3.07	2.93	2.86	2.73	2.17	1.48	0.33
Tl	81	2.66	2.38	2.23	2.25	2.47	2.81	2.95	3.06	3.10	3.05	2.91	2.82	2.67	2.10	1.42	0.29
Pb	82	4.29	4.18	4.14	4.10	4.07	4.03	3.96	3.88	3.73	3.58	3.32	3.06	2.79	2.20	1.29	0.18
Bi	83	4.20	4.09	4.03	3.98	3.94	3.87	3.76	3.65	3.43	3.24	2.90	2.55	2.24	1.63	0.63	0.07

B2 [El/Fe] predictions as the metallicity changes

In Tables B5 and B6 we list the theoretical surface predictions [El/Fe] for $M_{\rm ini}^{\rm AGB} = 1.3$ and 1.5 $M_{\odot}$ models for two ^{13}C-pockets (ST and ST/12), by changing the metallicity.

Table B5. Theoretical [El/Fe] predictions from He to Bi for $M^{\rm AGB}_{\rm ini} = 1.3\ M_{\odot}$ and two ^{13}C-pockets (ST and ST/12), as the metallicity changes.

		Case ST [Fe/H]								case ST/12 [Fe/H]							
El	Z	-3.6	-3.0	-2.6	-2.3	-2.0	-1.6	-1.3	-1.0	-3.6	-3.0	-2.6	-2.3	-2.0	-1.6	-1.3	-1.0
He	4	0.06	0.06	0.06	0.06	0.06	0.03	0.01	0.01	0.06	0.05	0.05	0.05	0.05	0.03	0.01	0.01
C	6	4.44	3.83	3.44	3.13	2.83	2.13	1.54	1.24	4.44	3.83	3.43	3.13	2.83	2.13	1.54	1.24
N	7	1.41	0.92	0.68	0.56	0.48	0.42	0.40	0.40	1.41	0.92	0.68	0.56	0.48	0.41	0.40	0.40
O	8	2.37	1.82	1.49	1.25	1.03	0.70	0.53	0.40	2.21	1.68	1.36	1.14	0.94	0.67	0.52	0.40
F	9	4.57	3.97	3.57	3.25	2.92	2.10	1.31	0.74	4.23	3.63	3.19	2.79	2.30	1.34	0.64	0.35
Ne	10	2.28	1.69	1.33	1.09	0.88	0.53	0.39	0.37	2.20	1.62	1.27	1.03	0.84	0.52	0.39	0.37
Na	11	1.85	1.26	0.90	0.66	0.46	0.15	0.05	0.04	1.65	1.06	0.71	0.48	0.31	0.10	0.04	0.03
Mg	12	1.06	0.63	0.46	0.38	0.33	0.28	0.26	0.26	0.79	0.47	0.35	0.31	0.28	0.26	0.25	0.25
Al	13	0.25	0.09	0.04	0.03	0.02	0.01	0.00	0.00	0.04	0.02	0.01	0.01	0.01	0.01	0.00	0.00
Si	14	0.38	0.32	0.31	0.30	0.29	0.29	0.28	0.28	0.29	0.29	0.29	0.29	0.29	0.28	0.28	0.28
P	15	1.21	0.76	0.55	0.43	0.34	0.14	0.05	0.04	0.25	0.20	0.18	0.15	0.12	0.04	0.01	0.01
S	16	0.34	0.31	0.30	0.30	0.29	0.29	0.29	0.29	0.29	0.29	0.29	0.29	0.29	0.29	0.29	0.29
Cl	17	0.08	0.06	0.06	0.05	0.05	0.02	0.01	0.01	0.05	0.04	0.04	0.04	0.04	0.03	0.01	0.01
Ar	18	0.27	0.26	0.26	0.26	0.26	0.26	0.26	0.26	0.26	0.26	0.26	0.26	0.26	0.26	0.26	0.26
K	19	0.33	0.33	0.32	0.32	0.31	0.30	0.29	0.29	0.32	0.31	0.31	0.31	0.30	0.29	0.29	0.29
Ca	20	0.29	0.29	0.29	0.29	0.29	0.29	0.29	0.29	0.29	0.29	0.29	0.29	0.29	0.29	0.29	0.29
Sc	21	0.41	0.36	0.34	0.30	0.26	0.09	0.04	0.04	0.28	0.25	0.22	0.21	0.21	0.11	0.04	0.03
Ti	22	0.29	0.27	0.27	0.26	0.26	0.25	0.24	0.25	0.27	0.27	0.27	0.27	0.28	0.25	0.24	0.24
V	23	0.03	0.01	0.01	0.01	0.00	0.00	0.00	0.00	0.01	0.01	0.01	0.01	0.01	0.00	0.00	0.00
Cr	24	-0.20	-0.20	-0.20	-0.20	-0.20	-0.20	-0.20	-0.20	-0.20	-0.20	-0.20	-0.20	-0.20	-0.20	-0.20	-0.20
Mn	25	-0.40	-0.40	-0.40	-0.40	-0.40	-0.40	-0.40	-0.40	-0.40	-0.40	-0.40	-0.40	-0.40	-0.40	-0.40	-0.40
Fe	26	0.00	0.00	0.00	0.00	0.00	0.00	0.00	0.00	0.00	0.00	0.00	0.00	0.00	0.00	0.00	0.00
Co	27	0.42	0.43	0.43	0.42	0.40	0.19	0.06	0.03	0.41	0.38	0.35	0.30	0.22	0.07	0.03	0.03
Ni	28	0.10	0.09	0.08	0.07	0.05	0.01	0.00	0.00	0.07	0.05	0.03	0.02	0.01	0.00	0.00	0.00
Cu	29	0.87	0.85	0.80	0.74	0.63	0.22	0.04	0.02	0.71	0.57	0.45	0.32	0.18	0.07	0.05	0.07
Zn	30	0.40	0.36	0.31	0.24	0.16	0.02	0.00	0.00	0.23	0.13	0.07	0.04	0.02	0.04	0.04	0.04
Ga	31	0.87	0.80	0.70	0.57	0.38	0.06	0.02	0.02	0.50	0.31	0.19	0.12	0.11	0.19	0.18	0.18
Ge	32	0.85	0.77	0.65	0.50	0.31	0.05	0.02	0.02	0.44	0.25	0.16	0.12	0.15	0.29	0.25	0.22
As	33	0.68	0.59	0.48	0.34	0.18	0.02	0.01	0.01	0.28	0.15	0.09	0.08	0.12	0.26	0.21	0.16
Se	34	0.76	0.66	0.52	0.36	0.19	0.03	0.02	0.03	0.30	0.17	0.13	0.12	0.23	0.40	0.31	0.22
Br	35	0.66	0.56	0.43	0.28	0.14	0.02	0.01	0.02	0.23	0.13	0.10	0.10	0.20	0.36	0.27	0.18
Kr	36	0.74	0.61	0.46	0.31	0.18	0.07	0.05	0.12	0.31	0.26	0.26	0.32	0.49	0.56	0.38	0.22
Rb	37	0.88	0.72	0.55	0.39	0.26	0.11	0.07	0.16	0.44	0.40	0.41	0.47	0.66	0.63	0.38	0.18
Sr	38	0.67	0.51	0.40	0.32	0.26	0.18	0.15	0.48	0.53	0.57	0.69	0.92	1.29	1.26	0.89	0.42
Y	39	0.66	0.49	0.41	0.36	0.31	0.23	0.18	0.56	0.65	0.71	0.84	1.09	1.44	1.31	0.84	0.31
Zr	40	0.65	0.48	0.41	0.37	0.33	0.24	0.20	0.66	0.72	0.79	0.94	1.20	1.50	1.31	0.70	0.20
Nb	41	0.68	0.50	0.43	0.39	0.35	0.26	0.21	0.68	0.76	0.83	0.98	1.25	1.54	1.32	0.67	0.18
Mo	42	0.56	0.40	0.34	0.31	0.27	0.20	0.16	0.61	0.67	0.74	0.89	1.15	1.41	1.17	0.47	0.10
Ru	44	0.40	0.27	0.23	0.19	0.16	0.11	0.10	0.50	0.47	0.52	0.65	0.90	1.18	0.99	0.34	0.07
Rh	45	0.21	0.13	0.10	0.08	0.06	0.05	0.05	0.31	0.25	0.28	0.39	0.61	0.88	0.71	0.19	0.03
Pd	46	0.42	0.29	0.24	0.21	0.18	0.15	0.16	0.64	0.52	0.58	0.75	1.06	1.37	1.16	0.43	0.09
Ag	47	0.21	0.13	0.11	0.09	0.07	0.07	0.07	0.40	0.29	0.34	0.49	0.76	1.03	0.83	0.23	0.04
Cd	48	0.44	0.31	0.27	0.25	0.25	0.23	0.22	0.78	0.66	0.76	0.96	1.26	1.53	1.29	0.48	0.11
In	49	0.31	0.21	0.19	0.18	0.18	0.15	0.15	0.62	0.53	0.61	0.80	1.08	1.34	1.10	0.34	0.06
Sn	50	0.61	0.45	0.40	0.37	0.35	0.30	0.27	0.88	0.84	0.95	1.15	1.43	1.65	1.35	0.44	0.09
Sb	51	0.40	0.27	0.23	0.21	0.19	0.15	0.14	0.59	0.58	0.68	0.86	1.11	1.29	0.98	0.21	0.03
Te	52	0.33	0.22	0.18	0.16	0.15	0.12	0.11	0.53	0.50	0.59	0.76	1.01	1.18	0.88	0.16	0.02
I	53	0.12	0.07	0.05	0.05	0.04	0.03	0.03	0.25	0.21	0.27	0.38	0.58	0.73	0.48	0.05	0.00
Xe	54	0.38	0.26	0.22	0.20	0.18	0.15	0.14	0.62	0.58	0.67	0.86	1.11	1.27	0.93	0.17	0.02
Cs	55	0.29	0.19	0.16	0.14	0.13	0.12	0.12	0.56	0.48	0.57	0.76	1.01	1.17	0.84	0.13	0.02
Ba	56	1.09	0.89	0.82	0.78	0.76	0.69	0.83	1.46	1.57	1.68	1.87	2.05	2.15	1.50	0.46	0.06
La	57	1.09	0.89	0.82	0.79	0.76	0.70	0.88	1.46	1.61	1.72	1.90	2.07	2.15	1.38	0.40	0.03
Ce	58	1.20	1.00	0.93	0.89	0.88	0.83	1.11	1.58	1.80	1.90	2.06	2.19	2.29	1.35	0.40	0.02
Pr	59	1.00	0.80	0.74	0.71	0.70	0.68	0.95	1.38	1.60	1.70	1.87	2.00	2.10	1.15	0.28	0.01
Nd	60	1.08	0.88	0.82	0.79	0.77	0.74	1.05	1.46	1.69	1.79	1.96	2.08	2.18	1.16	0.29	0.01
Sm	62	0.93	0.74	0.67	0.64	0.62	0.58	0.86	1.21	1.51	1.61	1.77	1.87	1.95	0.89	0.17	0.00
Eu	63	0.38	0.26	0.22	0.21	0.20	0.18	0.34	0.58	0.85	0.93	1.07	1.17	1.24	0.34	0.03	0.00
Gd	64	0.68	0.51	0.46	0.43	0.42	0.39	0.63	0.93	1.25	1.33	1.49	1.58	1.66	0.62	0.09	0.00
Tb	65	0.49	0.35	0.31	0.29	0.28	0.26	0.45	0.71	1.01	1.10	1.25	1.34	1.41	0.44	0.05	0.00
Dy	66	0.67	0.50	0.45	0.43	0.41	0.38	0.60	0.90	1.23	1.32	1.47	1.55	1.62	0.59	0.08	0.00
Ho	67	0.47	0.34	0.30	0.28	0.27	0.24	0.43	0.70	1.00	1.08	1.22	1.30	1.38	0.41	0.05	0.00
Er	68	0.77	0.59	0.54	0.51	0.50	0.44	0.70	1.01	1.35	1.44	1.58	1.66	1.73	0.67	0.10	0.00
Tm	69	0.66	0.50	0.45	0.42	0.41	0.35	0.57	0.87	1.22	1.30	1.44	1.50	1.58	0.55	0.07	0.00
Yb	70	1.07	0.87	0.80	0.77	0.74	0.67	0.99	1.32	1.66	1.74	1.88	1.96	2.06	0.94	0.20	0.01
Lu	71	0.82	0.63	0.58	0.54	0.51	0.45	0.75	1.05	1.37	1.45	1.59	1.67	1.77	0.69	0.11	0.00
Hf	72	1.25	1.05	0.97	0.92	0.89	0.84	1.19	1.50	1.83	1.92	2.07	2.16	2.26	1.09	0.26	0.01
Ta	73	1.13	0.93	0.86	0.81	0.78	0.74	1.09	1.39	1.71	1.80	1.95	2.04	2.14	0.97	0.20	0.01
W	74	1.25	1.04	0.97	0.92	0.90	0.86	1.23	1.53	1.86	1.94	2.10	2.18	2.28	1.10	0.26	0.01
Re	75	0.79	0.59	0.52	0.48	0.47	0.44	0.76	1.01	1.36	1.43	1.56	1.63	1.71	0.62	0.09	0.00
Os	76	0.63	0.47	0.41	0.39	0.38	0.36	0.65	0.86	1.20	1.28	1.43	1.50	1.60	0.50	0.06	0.00
Ir	77	0.15	0.09	0.07	0.07	0.06	0.06	0.16	0.25	0.48	0.53	0.64	0.70	0.78	0.10	0.00	0.00
Pt	78	0.45	0.32	0.28	0.26	0.26	0.24	0.47	0.64	0.98	1.06	1.20	1.27	1.36	0.32	0.03	0.00
Au	79	0.43	0.30	0.27	0.25	0.24	0.22	0.44	0.62	0.96	1.03	1.17	1.23	1.32	0.30	0.03	0.00
Hg	80	1.29	1.09	1.03	0.99	0.98	0.94	1.35	1.55	1.95	2.03	2.18	2.24	2.35	1.07	0.24	0.03
Tl	81	1.39	1.14	1.06	1.03	1.04	0.99	1.47	1.62	2.05	2.11	2.23	2.29	2.35	1.12	0.24	0.01
Pb	82	3.24	3.23	3.22	3.22	3.21	2.89	2.53	2.26	3.08	3.06	2.99	2.85	2.43	1.06	0.10	0.00
Bi	83	3.14	3.11	3.09	3.06	3.01	2.58	2.06	1.65	2.86	2.78	2.64	2.41	1.66	0.34	0.01	0.00

Table B6. The same as Table B5, but for $M_{\rm ini}^{\rm AGB} = 1.5\ M_{\odot}$.

		Case ST [Fe/H]								case ST/12 [Fe/H]							
El	Z	-3.6	-3.0	-2.6	-2.3	-2.0	-1.6	-1.3	-1.0	-3.6	-3.0	-2.6	-2.3	-2.0	-1.6	-1.3	-1.0
He	4	0.26	0.26	0.26	0.26	0.25	0.14	0.07	0.07	0.26	0.26	0.26	0.25	0.25	0.14	0.07	0.07
C	6	5.14	4.53	4.13	3.83	3.52	2.83	2.24	1.94	5.13	4.53	4.13	3.83	3.52	2.83	2.24	1.94
N	7	3.15	2.55	2.16	1.86	1.57	0.98	0.64	0.53	3.15	2.55	2.15	1.86	1.56	0.98	0.63	0.52
O	8	3.07	2.48	2.09	1.79	1.50	0.95	0.63	0.46	2.89	2.30	1.92	1.63	1.35	0.86	0.59	0.43
F	9	5.02	4.42	4.02	3.70	3.38	2.62	1.90	1.41	4.63	4.02	3.60	3.25	2.88	2.10	1.44	1.10
Ne	10	3.87	3.27	2.87	2.58	2.28	1.62	1.11	0.93	3.87	3.26	2.87	2.57	2.28	1.62	1.11	0.93
Na	11	3.57	2.97	2.57	2.26	1.96	1.27	0.73	0.52	3.59	2.98	2.58	2.27	1.96	1.25	0.71	0.49
Mg	12	2.98	2.38	1.98	1.69	1.40	0.80	0.46	0.37	2.75	2.15	1.76	1.47	1.19	0.67	0.41	0.35
Al	13	1.75	1.17	0.81	0.57	0.37	0.10	0.03	0.02	1.39	0.84	0.53	0.35	0.21	0.06	0.02	0.02
Si	14	1.29	0.81	0.59	0.48	0.41	0.32	0.29	0.29	0.52	0.40	0.36	0.35	0.34	0.31	0.29	0.29
P	15	2.63	2.04	1.66	1.40	1.16	0.65	0.33	0.26	0.88	0.74	0.69	0.66	0.61	0.34	0.16	0.11
S	16	0.87	0.53	0.41	0.37	0.34	0.30	0.29	0.29	0.32	0.31	0.31	0.31	0.31	0.30	0.29	0.29
Cl	17	0.53	0.32	0.26	0.23	0.22	0.11	0.06	0.06	0.26	0.26	0.26	0.26	0.26	0.16	0.09	0.09
Ar	18	0.28	0.27	0.26	0.26	0.26	0.26	0.26	0.26	0.26	0.26	0.26	0.26	0.26	0.26	0.26	0.26
K	19	0.50	0.47	0.46	0.45	0.44	0.36	0.32	0.31	0.47	0.47	0.46	0.46	0.45	0.37	0.33	0.32
Ca	20	0.28	0.28	0.28	0.27	0.27	0.28	0.29	0.29	0.28	0.28	0.28	0.28	0.28	0.28	0.29	0.29
Sc	21	1.11	0.95	0.89	0.86	0.83	0.54	0.33	0.34	0.95	0.94	0.93	0.92	0.90	0.62	0.37	0.31
Ti	22	0.61	0.46	0.41	0.40	0.38	0.32	0.29	0.30	0.42	0.42	0.42	0.42	0.41	0.31	0.27	0.26
V	23	0.28	0.13	0.09	0.07	0.06	0.03	0.02	0.03	0.09	0.08	0.08	0.08	0.06	0.01	0.00	0.00
Cr	24	-0.20	-0.20	-0.20	-0.20	-0.20	-0.20	-0.20	-0.20	-0.20	-0.20	-0.20	-0.20	-0.20	-0.20	-0.20	-0.20
Mn	25	-0.40	-0.40	-0.40	-0.40	-0.40	-0.40	-0.40	-0.40	-0.40	-0.40	-0.40	-0.40	-0.40	-0.40	-0.40	-0.40
Fe	26	0.00	0.00	0.00	0.00	0.00	0.00	0.00	0.00	0.00	0.00	0.00	0.00	0.00	0.00	0.00	0.00
Co	27	1.01	1.01	1.01	1.00	0.99	0.70	0.43	0.36	1.01	1.01	1.00	0.98	0.95	0.66	0.41	0.37
Ni	28	0.32	0.32	0.31	0.30	0.27	0.12	0.05	0.03	0.32	0.31	0.29	0.27	0.25	0.12	0.05	0.04
Cu	29	1.44	1.43	1.41	1.39	1.34	0.95	0.57	0.43	1.43	1.40	1.38	1.34	1.29	0.94	0.64	0.58
Zn	30	0.83	0.81	0.78	0.74	0.68	0.35	0.14	0.08	0.83	0.80	0.77	0.74	0.71	0.49	0.32	0.31
Ga	31	1.41	1.37	1.33	1.28	1.19	0.74	0.36	0.24	1.42	1.39	1.36	1.34	1.31	1.04	0.80	0.75
Ge	32	1.41	1.37	1.32	1.26	1.16	0.70	0.33	0.24	1.46	1.43	1.41	1.39	1.38	1.15	0.90	0.82
As	33	1.24	1.19	1.14	1.08	0.97	0.53	0.22	0.17	1.33	1.30	1.29	1.28	1.28	1.06	0.82	0.71
Se	34	1.38	1.33	1.27	1.19	1.07	0.60	0.28	0.26	1.53	1.52	1.50	1.50	1.52	1.30	1.02	0.85
Br	35	1.28	1.22	1.16	1.09	0.97	0.51	0.22	0.22	1.45	1.44	1.43	1.43	1.44	1.22	0.94	0.76
Kr	36	1.55	1.45	1.37	1.28	1.16	0.72	0.48	0.65	1.86	1.84	1.84	1.84	1.85	1.57	1.19	0.90
Rb	37	1.82	1.71	1.63	1.53	1.40	0.95	0.69	0.88	2.17	2.16	2.16	2.16	2.17	1.87	1.45	1.09
Sr	38	1.68	1.51	1.42	1.34	1.27	0.97	0.90	1.34	2.24	2.24	2.25	2.26	2.29	2.00	1.53	1.09
Y	39	1.76	1.55	1.46	1.40	1.35	1.11	1.07	1.53	2.40	2.40	2.41	2.42	2.44	2.10	1.55	1.06
Zr	40	1.78	1.54	1.45	1.41	1.38	1.19	1.18	1.64	2.45	2.45	2.45	2.46	2.45	2.05	1.41	0.88
Nb	41	1.80	1.56	1.47	1.43	1.41	1.22	1.22	1.69	2.49	2.49	2.49	2.49	2.49	2.07	1.41	0.87
Mo	42	1.67	1.42	1.33	1.29	1.29	1.12	1.14	1.59	2.33	2.33	2.33	2.33	2.31	1.87	1.16	0.62
Ru	44	1.40	1.15	1.07	1.03	1.01	0.85	0.87	1.30	2.07	2.06	2.06	2.05	2.02	1.57	0.86	0.38
Rh	45	1.03	0.79	0.71	0.68	0.66	0.53	0.55	0.98	1.68	1.67	1.67	1.66	1.64	1.21	0.55	0.19
Pd	46	1.42	1.16	1.08	1.04	1.04	0.90	0.96	1.48	2.08	2.08	2.07	2.07	2.07	1.66	0.94	0.46
Ag	47	1.04	0.80	0.72	0.69	0.69	0.58	0.66	1.15	1.68	1.68	1.68	1.69	1.69	1.30	0.63	0.25
Cd	48	1.51	1.26	1.18	1.16	1.18	1.08	1.18	1.68	2.14	2.15	2.16	2.18	2.21	1.81	1.07	0.55
In	49	1.32	1.08	1.01	0.99	1.01	0.92	1.00	1.48	1.94	1.95	1.96	1.99	2.01	1.60	0.87	0.39
Sn	50	1.74	1.49	1.42	1.40	1.41	1.30	1.39	1.84	2.35	2.35	2.36	2.37	2.36	1.88	1.09	0.54
Sb	51	1.43	1.18	1.11	1.09	1.11	1.01	1.10	1.52	2.02	2.02	2.02	2.02	2.00	1.51	0.74	0.28
Te	52	1.30	1.05	0.99	0.97	0.99	0.90	0.99	1.40	1.87	1.87	1.88	1.88	1.86	1.36	0.62	0.20
I	53	0.82	0.61	0.55	0.54	0.55	0.49	0.56	0.92	1.37	1.37	1.37	1.37	1.35	0.88	0.27	0.05
Xe	54	1.40	1.16	1.09	1.07	1.09	1.01	1.10	1.50	1.95	1.95	1.95	1.96	1.93	1.40	0.64	0.20
Cs	55	1.21	0.98	0.91	0.90	0.92	0.86	0.96	1.38	1.77	1.77	1.77	1.78	1.77	1.26	0.52	0.14
Ba	56	2.30	2.08	2.03	2.04	2.11	2.09	2.15	2.40	2.72	2.72	2.73	2.73	2.69	2.02	1.15	0.44
La	57	2.31	2.10	2.06	2.07	2.15	2.14	2.20	2.40	2.68	2.69	2.69	2.70	2.64	1.92	1.05	0.32
Ce	58	2.45	2.26	2.23	2.26	2.35	2.35	2.37	2.52	2.76	2.76	2.77	2.77	2.71	1.91	1.01	0.26
Pr	59	2.23	2.04	2.01	2.04	2.13	2.14	2.17	2.33	2.53	2.54	2.55	2.56	2.50	1.70	0.82	0.17
Nd	60	2.32	2.14	2.11	2.13	2.23	2.23	2.24	2.39	2.60	2.61	2.62	2.62	2.56	1.72	0.83	0.16
Sm	62	2.17	1.99	1.96	1.99	2.08	2.08	2.07	2.19	2.43	2.43	2.44	2.43	2.35	1.50	0.63	0.09
Eu	63	1.46	1.28	1.26	1.28	1.37	1.37	1.37	1.48	1.72	1.72	1.72	1.71	1.64	0.82	0.19	0.00
Gd	64	1.89	1.71	1.68	1.71	1.81	1.81	1.80	1.91	2.15	2.15	2.16	2.14	2.07	1.21	0.41	0.03
Tb	65	1.65	1.47	1.44	1.47	1.57	1.57	1.56	1.66	1.90	1.90	1.91	1.89	1.81	0.97	0.26	0.01
Dy	66	1.88	1.70	1.68	1.71	1.80	1.81	1.79	1.89	2.13	2.13	2.14	2.12	2.04	1.18	0.39	0.03
Ho	67	1.64	1.46	1.44	1.47	1.56	1.57	1.55	1.64	1.88	1.88	1.89	1.87	1.79	0.94	0.25	0.00
Er	68	2.01	1.83	1.81	1.84	1.94	1.94	1.91	1.99	2.25	2.25	2.26	2.24	2.15	1.28	0.45	0.04
Tm	69	1.87	1.69	1.67	1.70	1.79	1.79	1.75	1.83	2.11	2.11	2.11	2.09	2.00	1.13	0.35	0.02
Yb	70	2.35	2.17	2.15	2.18	2.28	2.26	2.21	2.30	2.58	2.58	2.58	2.55	2.46	1.57	0.67	0.11
Lu	71	2.07	1.89	1.87	1.89	1.99	1.97	1.91	2.00	2.29	2.29	2.28	2.26	2.17	1.28	0.44	0.04
Hf	72	2.53	2.36	2.33	2.36	2.45	2.43	2.38	2.48	2.75	2.75	2.75	2.72	2.64	1.73	0.79	0.16
Ta	73	2.41	2.23	2.21	2.23	2.33	2.31	2.26	2.37	2.62	2.62	2.62	2.59	2.51	1.60	0.68	0.12
W	74	2.53	2.36	2.33	2.36	2.46	2.45	2.41	2.52	2.74	2.74	2.75	2.72	2.64	1.73	0.79	0.16
Re	75	1.95	1.79	1.77	1.80	1.90	1.89	1.84	1.95	2.13	2.13	2.13	2.11	2.02	1.14	0.35	0.03
Os	76	1.83	1.66	1.64	1.68	1.78	1.77	1.73	1.83	2.03	2.04	2.04	2.02	1.94	1.05	0.28	0.01
Ir	77	0.99	0.83	0.82	0.85	0.94	0.94	0.90	0.98	1.18	1.18	1.19	1.17	1.09	0.34	0.03	0.00
Pt	78	1.59	1.43	1.41	1.45	1.55	1.54	1.49	1.58	1.79	1.79	1.80	1.78	1.69	0.81	0.16	0.00
Au	79	1.56	1.40	1.38	1.42	1.52	1.51	1.45	1.54	1.76	1.76	1.76	1.74	1.65	0.77	0.15	0.00
Hg	80	2.58	2.42	2.40	2.44	2.54	2.53	2.47	2.57	2.76	2.76	2.77	2.75	2.67	1.71	0.74	0.19
Tl	81	2.61	2.47	2.46	2.51	2.62	2.59	2.49	2.61	2.71	2.71	2.72	2.69	2.60	1.66	0.68	0.14
Pb	82	4.12	4.08	4.07	4.06	4.05	3.72	3.33	3.07	3.37	3.33	3.26	3.11	2.75	1.65	0.50	0.06
Bi	83	3.98	3.94	3.93	3.91	3.87	3.48	3.00	2.56	3.15	3.08	2.96	2.74	2.21	1.00	0.11	0.01

APPENDIX C: ONLINE-ONLY MATERIAL

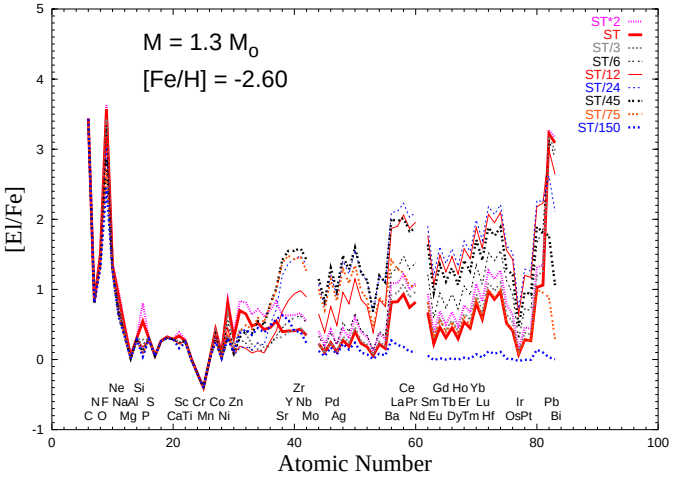

Figure C1. Elemental composition in the envelope at the last TDU, for AGB models of initial mass $M = 1.3\ M_{\odot}$, initial metallicity [Fe/H] $= -2.6$, and different choices of ^{13}C-pocket efficiency.

This paper has been typeset from a TEX/ LATEX file prepared by the author.

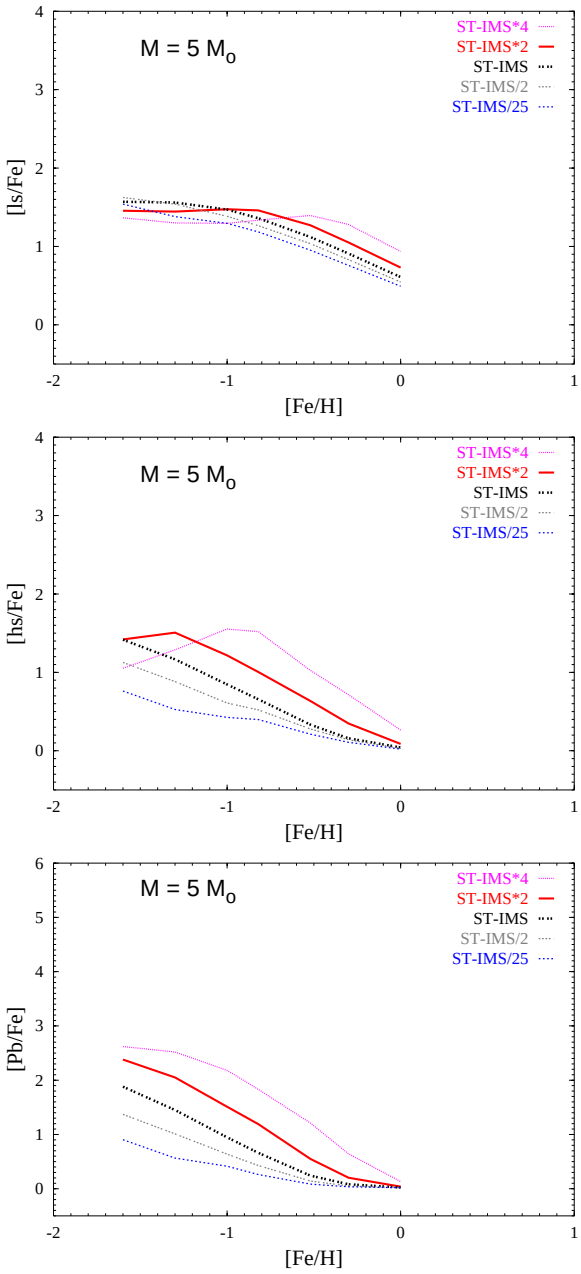

Figure C2. Theoretical results of [ls/Fe], [hs/Fe], and [Pb/Fe] (*top*, *middle* and *bottom panels*, respectively) for AGB models of initial mass $M = 5\ M_{\odot}$ and a range of ^{13}C-pocket efficiencies (ST-IMS×4 down to ST-IMS/25) in the metallicity range $-1.6 \leqslant$ [Fe/H] $\leqslant 0$.

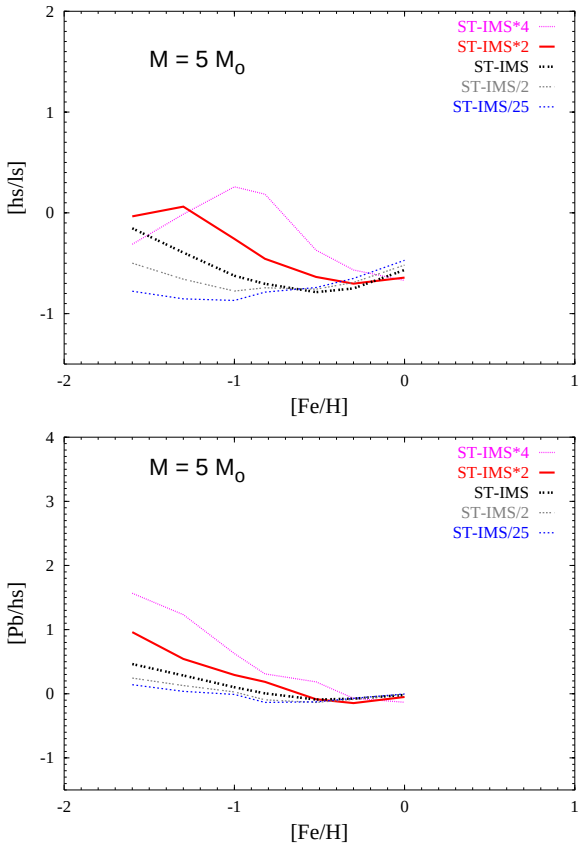

Figure C3. The same as Fig. C2, but for the two *s*-process indicators [hs/ls] (*top panel*) and [Pb/hs] (*bottom panel*).

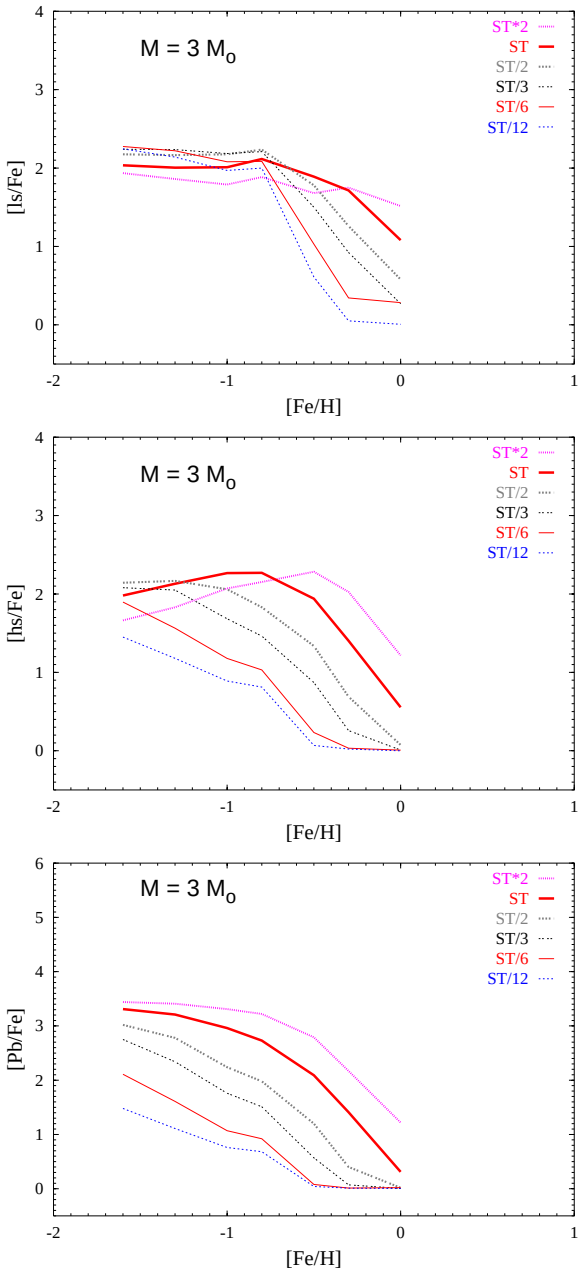

Figure C4. Theoretical results of [ls/Fe], [hs/Fe], and [Pb/Fe] (*top*, *middle* and *bottom panels*, respectively) for AGB models of initial mass $M = 3\ M_{\odot}$ and a range of ^{13}C-pocket efficiencies (ST×2 down to ST/12) in the metallicity range $-1.6 \leqslant$ [Fe/H] $\leqslant 0$.

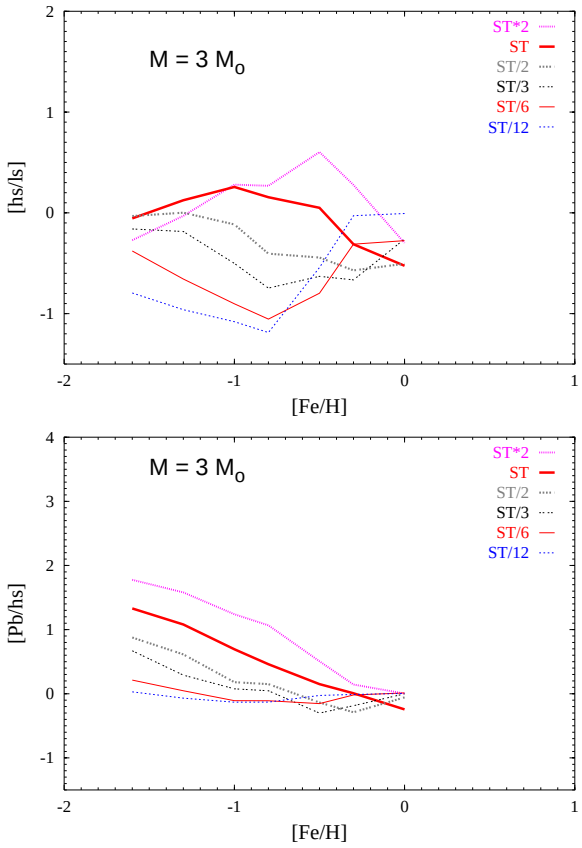

Figure C5. The same as Fig. C4, but for the two *s*-process indicators [hs/ls] (*top panel*) and [Pb/hs] (*bottom panel*).

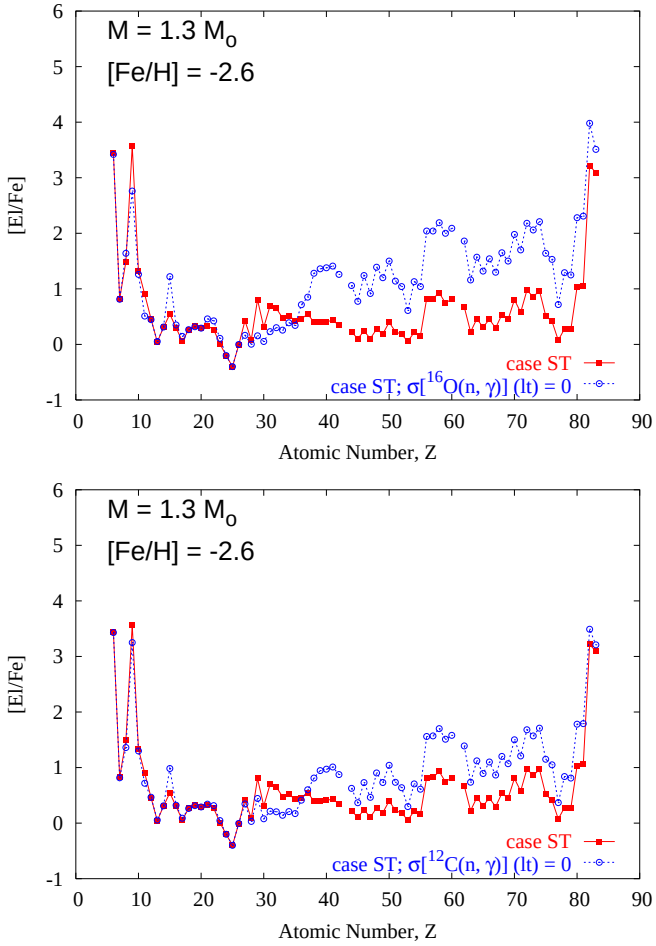

Figure C6. *Top panel:* theoretical predictions for AGB models of $M = 1.3\ M_{\odot}$, a case ST and [Fe/H] $= -2.6$. The line with full squares stands for the ordinary case, while the line with empty circles corresponds to a case with the cross section of ^{16}O(n, γ) put to zero. *Bottom panel:* the same as top panel, but the line with empty circles corresponds to a case with the cross section of ^{12}C(n, γ) put to zero.